

TOOLS AND APPLICATIONS FOR IMAGING-BASED
CARDIOVASCULAR MECHANICS

by

Arnold David Gomez

A dissertation submitted to the faculty of
The University of Utah
in partial fulfillment of the requirements for the degree of

Doctor of Philosophy

Department of Bioengineering

The University of Utah

August 2015

Copyright © Arnold David Gomez 2015

All Rights Reserved

The University of Utah Graduate School

STATEMENT OF DISSERTATION APPROVAL

The dissertation of Arnold David Gomez
has been approved by the following supervisory committee members:

Edward W. Hsu, Chair 04-20-2015
Date Approved

David A. Bull, Member 04-30-2015
Date Approved

Daniel Kim, Member 04-22-2015
Date Approved

Frank Sachse, Member 04-22-2015
Date Approved

Jeffrey A. Weiss, Member 04-23-2015
Date Approved

and by Patrick A. Tresco, Chair/Dean of

the Department/College/School of Bioengineering

and by David B. Kieda, Dean of The Graduate School.

ABSTRACT

Image-based biomechanics, particularly numerical modeling using subject-specific data obtained via imaging, has proven useful for elucidating several biomechanical processes, such as prediction of deformation due to external loads, applicable to both normal function and pathophysiology of various organs. As the field evolves towards applications that stretch the limits of imaging hardware and acquisition time, the information traditionally expected as input for numerical routines often becomes incomplete or ambiguous, and requires specific acquisition and processing strategies to ensure physical accuracy and compatibility with predictive mathematical modeling. These strategies, often derivatives or specializations of traditional mechanics, effectively extend the nominal capability of medical imaging hardware providing subject-specific information coupled with the option of using the results for predictive numerical simulations. This research deals with the development of tools for extracting mechanical measurements from a finite set of imaging data and finite element analysis in the context of constructing structural atlases of the heart, understanding the biomechanics of the venous vasculature, and right ventricular failure. The tools include: (1) application of Hyperelastic Warping image registration to displacement-encoded MRI for reconstructing absolute displacement fields, (2) combination of imaging and a material parameter identification approach to measure morphology, deformation, and mechanical properties of vascular tissue, and (3) extrapolation of

diffusion tensor MRI acquired at a single time point for the prediction the structural changes across the cardiac cycle with mechanical simulations. Selected tools were then applied to evaluate structural changes in a reversible animal model for right ventricular failure due to pressure overload.

To all the bricks in the Ivory Tower

In loving memory of Owen Stedham

TABLE OF CONTENTS

ABSTRACT.....	iii
LIST OF TABLES.....	ix
LIST OF FIGURES.....	x
LIST OF SYMBOLS.....	xii
LIST OF ABBREVIATIONS.....	xviii
ACKNOWLEDGEMENTS.....	xx
Chapter	
1. INTRODUCTION.....	1
2. BACKGROUND.....	5
2.1 Significance of Imaging-Based Cardiovascular Biomechanics.....	5
2.2 Noninvasive Imaging of Soft Tissue in Small Animals.....	7
2.3 Applied Computational Mechanics.....	13
2.4 Special Considerations for Vein Biomechanics.....	18
2.5 Special Considerations for Cardiac Biomechanics.....	21
2.6 References.....	29
3. CHARACTERIZATION OF REGIONAL DEFORMATION AND MATERIAL PROPERTIES OF THE INTACT EXPLANTED VEIN BY MICROCT AND COMPUTATIONAL ANALYSIS.....	37
3.1 Abstract.....	37
3.2 Introduction.....	38
3.3 Methods.....	42
3.4 Results.....	54
3.5 Discussion.....	63
3.6 Acknowledgements.....	66
3.7 Funding Sources.....	67
3.8 Conflicts of Interest	67

3.9 Statement of Human Studies.....	67
3.10 Statement of Animal Studies.....	67
3.11 References.....	68
4. ACCURATE HIGH-RESOLUTION MEASUREMENTS OF 3D TISSUE DYNAMICS WITH REGISTRATION-ENHANCED DISPLACEMENT ENCODED MRI.....	73
4.1 Abstract.....	73
4.2 Introduction.....	74
4.3 Theoretical Background	77
4.4 Methods.....	85
4.5 Results.....	95
4.6 Discussion.....	109
4.7 Conclusion.....	115
4.8 Acknowledgements.....	115
4.9 References.....	116
5. PREDICTION OF MYOCARDIAL STRUCTURAL ALTERATION ACROSS THE CARDIAC CYCLE USING COMPUTATIONAL MECHANICS.....	122
5.1 Abstract.....	122
5.2 Introduction.....	123
5.3 Methods.....	129
5.4 Results.....	144
5.5 Discussion.....	155
5.6 Conflicts of Interest.....	159
5.7 Acknowledgements	159
5.8 References.....	160
6. DT-MRI OBSERVATIONS OF FIBER STRUCTURE ALTERATIONS AS A COMPENSATORY MECHANISM FOR VENTRICULAR PRESSURE OVERLOAD: PRELIMINARY RESULTS.....	167
6.1 Abstract.....	167
6.2 Introduction.....	168
6.3 Methods.....	169
6.4 Results.....	174
6.5 Discussion.....	178
6.6 Acknowledgements.....	182
6.7 References.....	183
7. CONCLUDING REMARKS.....	186
7.1 Summary.....	186
7.2 Future Directions.....	188

7.3 Final Thoughts.....	191
7.4 References.....	193

LIST OF TABLES

3.1: Material coefficients sets.....	50
4.1: Mean error in displacement estimations under different deformation conditions.....	97
4.2: Performance of the proposed displacement measurement approach as a function of image SNR.....	100
4.3: Mean error with respect to true displacement field for all deformations with registration parameter variations.....	102
5.1: Material coefficient sets for passive myocardium.....	139
5.2: Fiber and sheet distribution coefficients.....	143
5.3: Mean simulated kinematic parameters.....	148
5.4: Mean transmural helix angle slope.....	150
6.1: Mean helical angle slopes and specimen wall thickness.....	176
6.2: DT-MRI parameters.....	179

LIST OF FIGURES

2.1: Motion-induced changes in the net MRI phase of a given voxel.....	12
2.2: Computational modeling of a Vein.....	19
2.3: Computational modeling of the Ventricles	22
2.4: Left-ventricular coordinate system.....	26
3.1: MicroCT-compatible pressurization apparatus.....	44
3.2: Stress-strain responses of the material models used in all computational analyses.....	51
3.3: Dependence of CT contrast on soaking time and solution concentration.....	55
3.4: MicroCT images of a vein sample under load.....	56
3.5: Computational model geometry.....	58
3.6: Hyperelastic Warping strain measurement.....	59
3.7: Forward FE simulations of the pressurized vein.....	61
4.1: Effect of phase wrapping in displacement profiles.....	79
4.2: Schematic illustration of the proposed registration-enhanced DENSE reconstruction.....	83
4.3: Numerical phantom and images used for verification.....	86
4.4: Schematic and MR images of the controlled motion apparatus.....	91
4.5: Displacement vector fields obtained by the different schemes for deformation scenario (c)	96
4.6: Strain maps obtained by the different schemes for deformation scenario (c)	99

4.7: Experimental validation measurements on the rotating phantom.....	104
4.8: Tissue Displacements by tagging and registration-enhanced DENSE.....	106
4.9: Direct comparison of displacements obtained by the proposed technique and tagging.....	107
4.10: Multislice Reconstruction of 3D Left-Ventricular Motion.....	108
4.11: Circumferential strain maps in the rat LV myocardium.....	110
5.1: Angular quantification of fiber and sheet structures.....	125
5.2: Spatial distribution of LV helix angle along the radial direction.....	126
5.3: Mesh convergence via maximum shear strain.....	136
5.4: Representative finite-element model of the LV wall.....	137
5.5: Material symmetry assumptions.....	140
5.6: Isolated heart during arrest and contracture.....	145
5.7: Histogram representation of structural angles populations at ED and ES.....	147
5.8: Histograms of structural angles populations using the “rotation-only” approach to transform DTI data from an initial time point to ED and ES.....	151
5.9: Histograms of structural angle populations using the “full deformation” approach to transform DTI data from an initial time point to ED and ES.....	153
5.10: Warping DTI data across the cardiac cycle.....	154
5.11: Deformed tracts of a collection of fibers in a longitudinal isocline along the radial direction.....	156
6.1: Computational mesh of biventricular mechanics.....	173
6.2: Wall thickness difference between failure specimens.....	175
6.3: Representative transmural helical angle distributions of controls RVR, and RVF subgroups.....	177
6.4: Biventricular simulation of pressure overload.....	180

LIST OF SYMBOLS

(in order of appearance)

CHAPTER 2

g_i	i-th X-ray projection
l	Rotated Cartesian coordinate
m	Rotated Cartesian coordinate (orthogonal to l)
θ	Projection angle
μ	Linear attenuation coefficient
s	Projection path
\bar{E}	X-ray effective energy
\vec{r}	Position, Cartesian coordinate in laboratory frame
B	Magnetic field
t	Time
γ	Gyromagnetic ratio (proportionality constant between frequency and magnetic field strength)
ω	Lamor frequency (angular speed of precession)
B_0	Main magnetic field in a MRI system
\vec{G}	Imaging gradient
T	Time interval (typically)

ϕ	MRI phase
\vec{v}	Velocity
W	Strain energy function
c	Strain energy scaling coefficient (material parameter)
Q	Exponential term in a Fung-type strain energy function
\underline{E}	Green-Lagrange strain tensor
μ_a	Frame invariant material coefficient
λ_{ab}	Frame invariant material coefficient (cross terms)
\underline{A}	Material directionality (texture) tensor
\vec{a}	Material directionality (texture) vector
c_i	i-th material coefficient
E_{ij}	Components of the Green-Lagrange strain tensor
$\hat{\theta}$	Unit vector in the circumferential direction
$\hat{\ell}$	Unit vector in the longitudinal direction
\hat{r}	Unit vector in the radial direction

CHAPTER 3

H_t	Local Hounsfield intensity
$\underline{\hat{C}}$	Right Cauchy strain tensor
\vec{x}	Current coordinates
\vec{X}	Reference coordinates
\underline{E}	Green-Lagrange strain tensor
\underline{P}	Second Piola-Kirchoff stress tensor

W	Strain energy function
U	Image-based energy (similarity metric)
T	Target image
S	Template image
Ψ	Total system energy
λ	Scaling coefficient weighting image-based energy (drives registration)
c_1	i -th material coefficient
\bar{I}_1	First invariant of deviatoric Right Cauchy strain tensor
\bar{I}_2	Second invariant of deviatoric Right Cauchy strain tensor
J	Determinant of deformation gradient $J = \det \left(\frac{d\vec{x}}{d\vec{x}} \right)$ (measure of volumetric deformation)
K	Bulk modulus
$\xi^{(i)}$	Exponential fiber stiffness coefficient
$\alpha^{(i)}$	Exponential fiber stiffness coefficient
\bar{I}_n	Projection of the Right Cauchy strain tensor along the fiber direction
ε_m	Residual strain error-
N	Number of elements in the analysis region

CHAPTER 4

\vec{u}	Displacement vector
\vec{r}	Spatial coordinate in the laboratory frame
\vec{k}_e	Displacement encoding gradient
N	Number of phase images

ϕ_i	i-th phase image
\underline{K}	Displacement reconstruction matrix
\vec{u}_d	Phase-based displacement
\vec{u}_{ref}	Reference displacement vector
T	Target image
S	Template image
$\hat{\phi}$	Deformation map
\vec{U}_w	Image-based displacement (in reference coordinates)
\vec{x}	Current coordinates
\vec{X}	Reference coordinates
\vec{b}	Registration force
$\vec{\eta}$	General linearization direction
∇S	Target image gradient
\vec{u}_w	Image-based displacement (in current coordinates)
E	Image intensity energy
λ	Scaling coefficient weighting image-based energy (drives registration)
\underline{Q}	Rotation matrix
\underline{I}	Identity tensor C_1
C_1	Material coefficient on Neo-Hookean solid
κ	Bulk modulus

CHAPTER 5

$\hat{\theta}$	Unit vector in the circumferential direction
$\hat{\rho}$	Unit vector in the longitudinal direction
\hat{r}	Unit vector in the radial direction
α	Helix angle
α'	Transverse angle
β	Sheet angle
β'	Sheet elevation angle
\hat{f}	Unit vector in the local fiber direction
\hat{s}	Unit vector in the local sheet direction
$\vec{\varphi}$	Deformation map
\vec{X}	Reference coordinates
\vec{x}	Current coordinates
\vec{e}_R	General vector in current coordinates (rotated only)
\vec{E}	General vector in reference coordinates
\underline{R}	Rotation matrix
\underline{F}	Deformation gradient
\vec{e}_F	General vector in current coordinates (full transformation)
W	Strain energy function
c	Strain energy scaling coefficient (material parameter)
Q	Exponential term in a Fung-type strain energy function
J	Determinant of deformation gradient $J = \det\left(\frac{d\vec{x}}{d\vec{X}}\right)$ (measure of

	volumetric deformation)
c_i	i-th material coefficient
E_{ij}	Components of the Green-Lagrange strain tensor
\underline{T}	Total Cauchy stress
T_{max}	Maximum sarcomere tension
Ca_0	Peak calcium concentration
ECa_{50}	Calcium sensitivity
C_{lc}	Tension development loading curve
t	Time
B	Sarcomere length difference weight
l	Current sarcomere length
l_0	Zero-tension sarcomere length
k_i^α	Coefficients for fiber angle distribution polynomials
k_i^β	Coefficients for sheet angle distribution polynomials

LIST OF ABBREVIATIONS

(in alphabetical order)

ADP	Adenosine diphosphate
ATP	Adenosine triphosphate
CT	Computed tomography
DENSE	Displacement encoding with stimulated echoes
DT-MRI	Diffusion tensor magnetic resonance imaging
EAD	Early diastole
ECG	Electrocardiogram
ED	End diastole
ES	End systole
FE	Finite element
FEA	Finite element analysis
FOV	Field of view
LHS	Left hand side
LV	Left ventricle
microCT	High-resolution (micro-resolution) computed tomography
MR	Magnetic resonance
MRI	Magnetic resonance imaging
PBS	Phosphate buffered saline

RHS	Right hand side
RMS	Root mean squared
RV	Right ventricle
SNR	Signal-to-noise ratio
TE	Echo time
TR	Repetition time

ACKNOWLEDGEMENTS

This research could not have been completed without the help from a diverse group of talented and generous individuals to whom I am deeply grateful.

During the last 5 years, my co-advisors, Dr. Edward Hsu and Dr. David Bull, provided me with all the resources, guidance, and independence needed to gain confidence and forge my technical expertise. I would like to thank my supervising committee for their counsel and cumulative efforts, which ultimately advance scientific understanding and many people's careers including my own.

I am very grateful the people at the Small Animal Imaging Core for their assistance with imaging equipment, Dr. Jeffrey Weiss and the Musculoskeletal Research Laboratories, which develops and maintains the finite element analysis software used throughout this research, and to Dr. Stephen McKellar for granting me access to the reversible model of right ventricular failure. I am also indebted to my master's advisor, Dr. Steven Day, for providing me with an initial exposure to bioengineering research and guidance during key moments of my life, and Dr. Don Olsen for introducing me to the University of Utah.

Lastly, I would like to thank my family and friends for their affection, encouragement, and sense of direction in terms of what truly matters.

CHAPTER 1

INTRODUCTION

Fundamental aspects in tissue mechanobiology are often common across multiple clinically relevant and basic research problems, and can be elucidated through a unique combination of medical imaging and computational biomechanics. Through closed-form relationships of quasi-elastic behavior, mechanical simulations allow approximations mechanical stress and other parameters that are difficult or impossible to measure by experimental means particularly *in vivo*. However, computational modeling is susceptible to lack of fidelity. Inclusion of imaging information effectively reduces the solution space of a given problem to the most plausible representations of the physical processes under investigation. One of the most common forms of imaging-based biomechanics consists of using morphological information to customize the geometrical domain of mechanical simulations, but it can be extended to structural and kinematic information as modalities like MRI and ultrasound are sensitive to these features. Synergistic usage of medical imaging, which provides access and fidelity, and computational mechanics, which offers flexibility and predictive power is often referred to with the term “imaging-based computational biomechanics.”

As a field of study, imaging-based computational biomechanics, is not thoroughly defined. In some cases, imaging information can be used as a direct input to

computational models for customization. In other instances, the output of imaging hardware can be used to infer a set of characteristics about a system through analytical assumptions of an underlying phenomenon, which is the basis of exciting new fields like elastography. Mechanical principles can be used to correct degraded data or interpolate incomplete measurements, as is the case on recent investigations involving model-based interpolation and reconstruction strategies. Regardless of the case, the ability to estimate realistic physical behavior through determinate enforcement of conservation principles is a distinct and powerful advantage over other reconstruction or image processing strategies. Although the precise scope of imaging-based computational biomechanics can be ambiguous, the field itself is very likely to expand in the future given the natural tendency towards perceiving physical phenomena at increasingly ambitious scale and detail.

Motivated by an interest in expanding the capabilities of imaging hardware with computational physics, this research focuses on the application of a popular discretization in biomechanical analysis, the finite element method, to address certain limitations of computed tomography and magnetic resonance. Within this essay, this principle is exemplified in terms of the design of methods that enable research on understudied aspects involving the morphology, property coefficients, kinematics and structure of tissue in the cardiovascular system.

Chapter 2 contains a brief background, including some justification for concentrating on the cardiovascular system in terms of our society's needs, as well as preliminary concepts involving imaging soft tissue and the approach to computational mechanics followed through the investigations herein. Some particular consideration is

given to MRI to exemplify its ability to produce both morphological data as well as the structural and kinematic data. The chapter also contains special considerations relevant to the tissues under consideration.

In Chapter 3, the specifics of a method for visualization of morphology and deformation venous tissue using computed tomography are introduced. The investigation explored the application of iodine as a contrast agent with the purpose of evaluating tissue mechanics of veins using with specialized inflation-extension experiments. A mechanics-based image registration, also referred as Hyperelastic Warping, was used to measure deformation, and a series of finite-element simulations were performed in order to find a set of material coefficients descriptive of tissue stiffness.

Chapter 4 describes a method for reconstructing displacement-encoded MRI with the aid of image registration. The basic premise of this investigation is the extraction of high-confidence regions in the displacements fields obtained with image registration by projecting the solution to the intensity gradient. The results can then be used to approximate lost or incomplete information. In the study, the method was used to estimate the bulk motion component, which is lost on the phase unwrapping step of traditional displacement-encoded MRI, but the same idea can be implemented in other applications by specializing an expected error criteria.

The methodology needed for extending the utility of structural data acquired at discrete time points to describe the entire cardiac cycle is presented in Chapter 5. Myocardial deformation estimates obtained with finite element analysis were used to transform fiber and sheet orientation information obtained at early diastole into its

equivalent at end diastole and end systole. At these conformations, the results were experimentally validated against diffusion tensor MRI results obtained on a MRI-compatible isolated heart preparation. The computational models were then used to produce computationally driven, but experimentally confirmed, estimation of structural deformation using *in vivo* measurements of volume and pressure.

Chapter 6 consists of a practical application of selected methods herein to elucidate kinematic and structural changes of the ventricles subject to right-ventricular overload. Because it is based on a reversible animal model, the investigation provides insight on recovery, as well as health and disease.

The concluding chapter of this document, Chapter 7, provides a discussion regarding the advantages and disadvantages of using computational mechanics to complement the output of imaging hardware, and offers some recommendations for improvements on the methods presented herein as well as future areas of investigation.

CHAPTER 2

BACKGROUND

2.1 Significance of Imaging-Based Cardiovascular Biomechanics

For the past 50 years, cardiovascular disease has been regarded as the principal cause of mortality among people in the developed world, and is becoming increasingly prevalent in developing countries [1]–[3]. As a field, imaging-based cardiovascular mechanics has experienced a series of outstanding contributions leading to improving the accuracy and expanding the uses of cardiovascular simulations, as well as incorporation of physical principles into image reconstruction and analysis. Both of these aspects have placed imaging-based cardiovascular biomechanics in a strong position for studying cardiovascular disease progression, aiding design of treatment strategies, and increasing diagnostic capability.

The first aspect, biomechanical simulations, is evolving into a completely new type of experimentation of biological systems based primarily on numerical results. In traditional engineering, testing prototypes *in silico* has resulted in a tremendous increase of financial and human efficiency [4], [5]. The idea stems from the basic premise that the same physical principles that enable a simulation to accurately describe a validation experiment are just as effective in additional circumstances. Computational approaches already have a strong presence in the biomedical arena. Currently, it is possible to gain

predictive insights on the performance of medical devices promising for treatment of congestive heart failure, which affects approximately 6 million people in America alone [6]. Some of these devices include intramyocardial implants, myocardial patches aimed to reduce ventricular volume, and ventricular assist pumps [7]–[9]. This last one includes a large number of examples of computer-aided design and testing [10], [11], but also fitting, and optimization of flow parameters to prevent device failure and simplify manufacturing [10], [12]. Additional investigations have provided insight on wall stress distribution and its role in right ventricular failure, an underestimated ailment often more deadly than isolated left ventricular failure [13], [14], and a secondary effect affecting 9-50% of left ventricular assist device recipients [15], [16]. Numerical strategies have been demonstrated in the study of large arteries, in the context of vascular aneurysm, stent design, and characterization of fluid-solid interaction [17]–[19]. Within the study of venous vasculature, computational fluid mechanics has been employed for identifying wall shear stress ranges likely to result in neointimal hyperplasia [20], which is a major cause of failure in 20-60% of the roughly 50,000 arteriovenous fistulas and 350,000 coronary artery bypass grafts that are performed in the US annually [21], [22]. Similar studies have, in turn been used to improve fistula creation procedures for dialysis and optimization of artificial grafts [23], [24]. Computational models have also been used to gauge the effectiveness of myocardial reconstruction procedures, and the distributions of internal forces ultimately linked to contractility and stress-induced remodeling [9], [25]–[27].

Elastography is perhaps the most visible example of incorporating computational mechanics into image reconstruction [28]–[30]. There are different approaches for

inferring material characteristics with imaging information, and most revolve around detection of tissue response (deformation or deformation rate) to a known load [31], [32]. Preliminary investigations exist for inferring shear moduli of the myocardium by measuring wave propagation, with the goal of differentiating between different types of akinetic tissue [33], [34]. Deformation obtained through tagged MRI has been shown useful for indirect approximation of myocardial stiffness and active stress (which is directly related to tissue contractility) through finite-element based parameter identification [25]. A similar approach for approximating the stiffness of the vein wall with high-resolution speckle-tracking has also been demonstrated in venous tissue in the forearm [35], [36]. Further applications of the field include model-based reconstruction of DT-MRI, whereby exponential signal decay and positive-definitiveness of the diffusion tensor are enforced, which has shown to consistently accelerate scan time 8-fold [37]. Additionally, zero divergence, interslice interpolation of displacement fields has been introduced to increase the accuracy of strain calculation in incompressible tissue, particularly in the heart [38].

2.2 Noninvasive Imaging of Soft Tissue in Small Animals

This research focuses on two modalities of medically imaging specialized for small animals: computed tomography (for the vein) and magnetic resonance (for the heart). In general, the most common modalities of medical imaging can be classified according to the physical processes that enable detection of image information [39], including those dealing with measuring the intensity and speed of ultrasound echoes (echography), gathering of gamma rays emitted by radiomarkers placed within the body (nuclear

medicine), collecting X-rays transmitted through the body (projection radiography, and computed tomography), and detecting electromotive forces induced by magnetic resonance (MRI). Because several branches of preclinical research make use of small animal models, all of these modalities have been adapted into specialized means for noninvasive tissue imaging at the small-animal scale (approximately 10-500 microns resolution over 1-2000 cubic centimeters). Rodents are often preferred because they are mammals with fast life cycles, are relatively simple to maintain, and can be genetically engineered models to develop myocardial conditions such as contractile insufficiency, and cardiomyopathy [40]. Imaging instruments at that scale can also be used to generate high-resolution data of intact human or large animal organs [41]. Some technical concepts preliminaries for the studies herein are reviewed below.

2.2.2 Computed Tomography

In small animal imaging, computer tomography is carried out in high-resolution instruments of resolutions as low as a few microns, and this characteristic surpasses practical MRI and ultrasound, making it an interesting choice for the study of tissue samples with minute features [42]. Computed tomography takes advantage of a set of i X-ray projections, $g_i(l, m, \theta)$, acquired from different coaxial angles, θ , using a rotating emitter-detector set, which are combined to reconstruct a volumetric image using methods such as filtered back projection. (l and m represent a subset, or a rotated plane, of the 3D laboratory coordinates.) Being a projection, any given pixel intensity in $g_i(l, m, \theta)$ is the result of the fundamental interaction between incident X-rays' effective energy, \bar{E} , and the *linear attenuation coefficient* of the material, μ , along the

projection path, s , namely,

$$g_i(l, m, \theta) = \int_0^d \mu(s, \bar{E}) ds. \quad (2.1)$$

Regardless of the method used to reconstruct the volumetric image, projection intensity bound by (2.1) is directly related to voxel intensity. Indeed, by calibrating the instrument against a phantom of known properties, a reasonably accurate reconstruction method will approximate $\mu(\vec{r})$ [39], which is the distribution of attenuation coefficients. Therefore, at a constant ray effective energy, tissue attenuation is the main source of CT contrast. This observation yields a fundamental challenge: Because attenuation coefficients across different types of soft tissue (or isolated tissue and aqueous saline solutions) are virtually identical across practical spectrum of ray energies [43], intensity differences between the tissue and its surroundings are likely to fall in the same quantization level of a discrete digital detector. This consideration is the basis for using contrast agents, such as ionic or nonionic iodine or barium compounds, for detection of soft tissue [44].

2.2.3 Magnetic Resonance Imaging

The local magnetic alignment of spin systems, like hydrogen protons in water molecules within tissue, is affected by external magnetic fields [45]. Given that (from an arbitrary initial state of magnetization) nuclear protons will start to precess into alignment with the external field, they will induce a measurable electromotive force onto a surrounding receiving coil. To provide a desired initial state of alignment inside a magnetic field, electrical current is passed through excitation coils producing modulated

radiofrequency pulses that “flip” spins into a given configuration. The formation of images is granted by spatially dependent variations from the main external field, induced by gradients, which encode the spatial location of voxels by altering their precession frequency. Once the signal phase and magnitude is measured, it can be frequency demodulated and reconstructed with methods specialized to different contrast types. In general, the strength of the signal originating from a given voxel increases with the number of protons present within the region, which can be used to discriminate tissue regions based on their proton density. Additional types of contrast can be achieved in numerous ways including taking advantage of realignment time constants, contrast agents, and phase. This last has the outstanding property of being affected by motion, which is of essential interest within this research because it is the basis for diffusion and displacement imaging [46], [47].

The precession frequency, ω , is directly proportional to a spatially and temporally varying magnetic field $B(\vec{r}, t)$. (\vec{r} symbolizes the spatial coordinates of a given point, and t symbolizes time.) Letting γ serve as proportionality constant, the relationship can be written as:

$$\omega(\vec{r}, t) = \gamma B(\vec{r}, t) = \gamma B_0 + \gamma \Delta B_0 + \gamma \vec{r}(t) \vec{G}(t), \quad (2.2)$$

where B_0 is the main magnetic field, ΔB_0 corresponds to a spatially dependent, but constant field inhomogeneity, and $\vec{G}(t)$ is a phase-sensitizing gradient. The total amount of phase accrued in a given time interval, T (typically the magnetic resonance echo time), corresponds to the time integral of (2.2). The phase *additional* to that induced by the main magnetic field, $\Delta\phi$, corresponds to the temporal derivative of the last two terms on the RHS in (2.2), in other words,

$$\Delta\phi = \int_0^T \omega(\vec{r}, t) dt = \gamma\Delta B_0 T + \gamma \int_0^T \vec{r}(t) \cdot \vec{G}(t) dt. \quad (2.2)$$

The additional phase can be further decomposed into $\Delta\phi = \phi_T - \phi_0$ with a background amount, ϕ_0 , which includes $\gamma\Delta B_0 T$. Thus, the relationship phase and movement (i.e., the phase at acquisition time, ϕ_T , and temporal derivatives of spatial location), can be expressed by expanding $\vec{r}(t)$ (2.2) with a Taylor series about zero, or,

$$\phi_T = \phi_0 + \gamma \sum_{n=0}^{\infty} \frac{1}{n!} \frac{d\vec{r}^n}{dt^n} \cdot \int_0^t \vec{G}(t) t^n dt. \quad (2.2)$$

Evaluating the first few terms shows that, depending on the gradient strength and waveform, phase can be related to position, velocity, (\vec{v} below), acceleration, and other such information. In essence,

$$\phi_T = \phi_0 + \gamma\vec{r} \cdot \int_0^t \vec{G}(t) dt + \gamma\vec{v} \cdot \int_0^t \vec{G}(t) t dt + \dots \quad (2.3)$$

indicates that motion sensitivity is associated to the n th moment of gradient with respect to time, and a background scan to remove ϕ_0 . [45], [48]

In practice, (2.3) is the theoretical origin of velocity-encoded “phase contrast” MRI, certain approaches for measuring displacement, as well as moment nulling (a strategy to remove motion sensitivity to reduce artifacts) [49], [50]. In diffusion weighting, which gives rise to diffusion tensor MRI, random motion of intravoxel water molecules cause *incoherent* phase accrument reducing the net aggregate magnetization of a voxel diminishing its magnitude [46]. The measurement of *coherent*, or bulk, motion-induced changes of phase do not have a direct effect on the signal magnitude. These interactions are exemplified in Figure 2.1, which illustrates changes in the phase distribution across

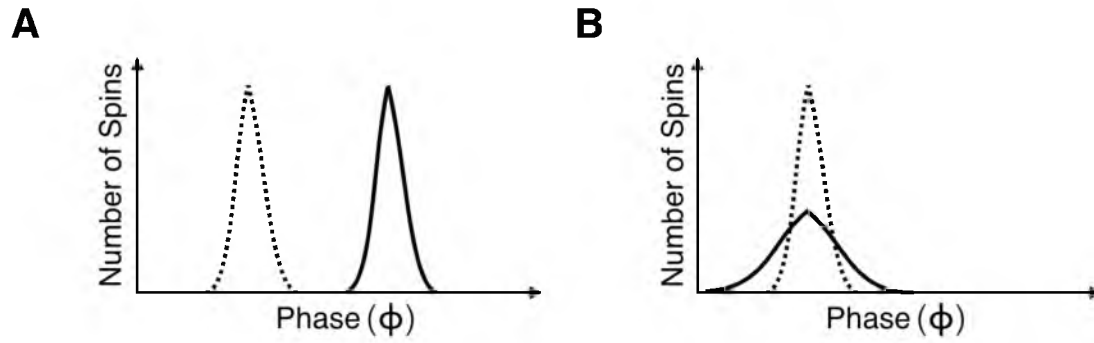


Figure 2.1. Motion-induced changes in the net MRI phase of a given voxel. Coherent motion (A), like bulk tissue motion or flow, results in a horizontal shift corresponding to a change of average phase distribution. Incoherent motion (B), such as that caused by diffusion of water molecules in the tissue, result in a change in the phase-distribution variance.

a population of spins within a given voxel assuming a Gaussian distribution. 3D fields are constructed by prescribing a set of $\vec{G}(t)$ to create images weighted along different directions, which can be later combined into a vector field [51].

2.3 Applied Computational Mechanics

Some authors have described biomechanics as a systematic means for modeling a biological system based on a mathematical description of conservation principles and the system's characteristics [52], [53]. The approach used in this research is modeled after some of these descriptions, and can be summarized in eight steps as follows [53]: (1) Observation and description of the geometry under consideration; (2) Identification of the constitutive characteristics of the materials involved in the process; (3) Derivation of a set of governing equations based on momentum, energy, or mass balance, or other expressions of conservation laws; (4) Application of a descriptive set of initial or boundary conditions based on observation of the system; (5) Generation of a set of state variables by solving the governing equations; (6) Experimentation in a controlled environment to obtain measurements for testing the mathematical model; (7) Comparison of measured and calculated variables, and refinement of modeling strategy; (8) Specialization of the model to predict the outcome of the system under different conditions.

Analysis of most biological systems results in a set of partial differential equations impractical to solve analytically due either, or a combination of, nonlinearity, irregular geometries, inhomogeneous distribution of properties, or with the application of complex initial or boundary conditions. Numerical methods provide a way to

approximate the solution of state variables by defining a discrete computational domain analogous to the problem in question. In the finite element method, variables of interest are defined by a set of local interactions at discrete locations in a subdomain, which can be assembled onto a global system of simultaneous equations where the boundary conditions are applied [54]. A central component of the finite element method, interpolation through element-specific shape functions, enables the application of calculus at element level making the method practical for a relatively wide range of governing equations and applications, including structural (which was used herein for estimation of deformation), and thermal (which was used for the definition of local coordinate systems) [55]. It also provides a way to exchange information between the model's finite-element domain and an image's lattice. Current nonlinear solution schemes, descriptions and implementations of constitutive relations for biological materials, and user interfaces have greatly simplified the application of the finite element method in biological problems. In the context of applied biomechanics, and other engineering disciplines, the general approach for computational modeling contains specialized considerations involving interaction with finite-element packages, namely, preprocessing, solution, and postprocessing [54]. During preprocessing the physical model of the simulation is determined, the geometry is discretized, material characteristics are assigned to the geometry, and boundary conditions are applied. In the solution step the problem is assembled into a system of simultaneous equations, and the control parameters of the solution process are defined. No single set of parameters is guaranteed to converge into a satisfactory set of variables, so different sets may be necessary. The so-called postprocessing involves extracting results from output files,

visualization, unit conversion, and other operations needed to assist interpretation of the solution.

The basic approach to extract and discretize a system's geometry is facilitated by three main processes: Segmentation, mesh generation, and mesh refinement, all of which are active areas of research [56]–[59]. The first process often involves computer-assisted delineation, or labeling, of features of interest. The second deals with the discretization of the domain into elements, which can vary among several formulations depending on the intricacy of the problem. Mesh refinement involves ascertaining the quality of the mesh in terms of fidelity to the features observed in volumetric images, element attributes to add numerical stability (like aspect ratio and volume), and convergence (in a consistency sense) of the solution. In both cases, mesh density is increased, i.e., element size is reduced increasing the total number of elements over a given volume, until features of interest are reflected on the mesh and until a consistent solution for a set of variables is achieved. Meshes composed of on linear hexahedral elements were used throughout this research because, among other reasons, they have been shown to perform well in soft-tissue problems [60], and facilitate pixel-wise mesh generation. However, these elements converge relatively slowly, meaning that final meshes contain thousands of elements.

A set of predefined models of material behavior is often included in a given analysis package providing a range of options, that can be increased by fitting experimental data and by user-defined materials. Most of the time, predefined models are based on experimental material characterization involving postulating one or several constitutive models, and testing their descriptive qualities against experimental data. A single

material can be used to represent different tissues by varying a set of coefficients, which are often available in the literature. In some circumstances, if coefficients are not explicitly defined, but sufficient experimental data (such as biaxial or shear responses) is presented, a set of coefficients can be obtained by fitting. Alternatively, a new constitutive model can be generated with user-defined materials. Although the traditional way to define a new set of constitutive equations for a material is to calculate derivatives of the strain energy function with respect to strain or strain invariants for the definition of stress and elasticity tensors [55], it is also possible to use superimposition of predefined material behavior through “solid mixtures” [61].

Boundary conditions are necessary to produce both, a realistic representation of the system under consideration and a well-posed problem [54], [55]. Biomechanical problems can be constrained in a variety of ways including restricting the motion of the nodes in a surface, and applying nodal forces, which can be prescribed to represent the action of physical loads or restrains. Because boundary conditions directly affect the number of unknowns in the assembled system of equations handled by the solver, they can improve convergence, and simplify the problem if it can be assumed to be symmetric. In many problems, there is a tradeoff between realistic boundary conditions and numerical stability that has to be addressed for analysis and interpretation of results particularly near the boundaries.

Although the preprocessing steps play a large role in being able to successfully obtain a solution for a problem, solver control variables can make a noticeable difference in terms of computational time and convergence. A useful way to improve convergence of nonlinear problems is to increase the number of steps needed to achieve

equilibrium under a relatively large load, known as “load ramping” [55]. Once a solution has been found under a conservative number of steps, the overall efficiency of solution in terms of total solution time can be increased with automatic time step adjustment. Relaxing of convergence tolerances can facilitate convergence at the risk of reducing the accuracy of the solution, but can be used to obtain an initial solution to pinpoint mesh deficiencies (that can be addressed with mesh refinement), or other underlying reasons for lack of convergence.

Postprocessing is highly varied and application-dependent, but, in general, involves extraction of raw data, unit conversion, and other manipulations needed to interpret results or to compare a simulated solution against experimental data. Modern postprocessing software includes a great deal of visualization including 3D exploration, creation of videos to display multiple views of given model, as well as statistical and other analysis tools.

In the context of the presented approach to applied computational mechanics, it is worth noting the roles of some of the software used in this research. Geometry discretization primarily involved Amira (FEI Life Sciences, OR, USA), for image segmentation and initial definition of surfaces, and TrueGrid (XYZ Applications, CA, USA) for mesh generation and refinement. Additional surface manipulations, such as smoothing and rotation, were performed in Meshlab (National Research Council, Italy) and some custom routines noted in each investigation. The FEBio software suite [62] played a central role in terms of preprocessing through Preview (which enables material and boundary conditions assignments, control parameter definition, as well as some mesh manipulation), obtaining solutions with FEBio2 implicit solver, and

postprocessing and visualization with Postview Software. In many ways, MATLAB (Mathworks, MA, USA) acted as the glue holding together different aspects of these investigations including: interaction between different programs with text files (generating mesh generation scripts, FEBio2 input files, and Postview files for visualization of quantities additional to those calculated by the solver), manipulation of data (image reconstruction, embedded calls to FEBio2), and some visualization (sliced images and image vector fields).

2.4 Special Considerations for Vein Biomechanics

One of the most important challenges involving studying the mechanics is the vein's wall thickness (or rather the lack of thereof). From an imaging perspective, venous tissue is difficult to detect because it requires relatively high resolution and has similar contrast to surrounding tissue making *in vivo* data difficult to segment [20], [36]. If images of sufficient quality are available, the procedures described in the previous section may be followed to generate a mesh. If so, it was helpful to mesh different sections of the sample as independent parts, each with their own set of elements, and assemble the parts to form a single entity (Figure 2.2).

From a biomechanical perspective, the vein wall is composed of three layers [63]: The tunica intima is the internal endothelial wall in closest contact to blood and provides virtually no contribution to the biomechanical response of the vein wall. The tunica media is composed by a helical organization of thick collagen fibers mostly oriented in the circumferential direction, parallel smooth muscle cells and longitudinal elastin fibers. Finally, the tunica adventitia, the outer-most layer, contains loose

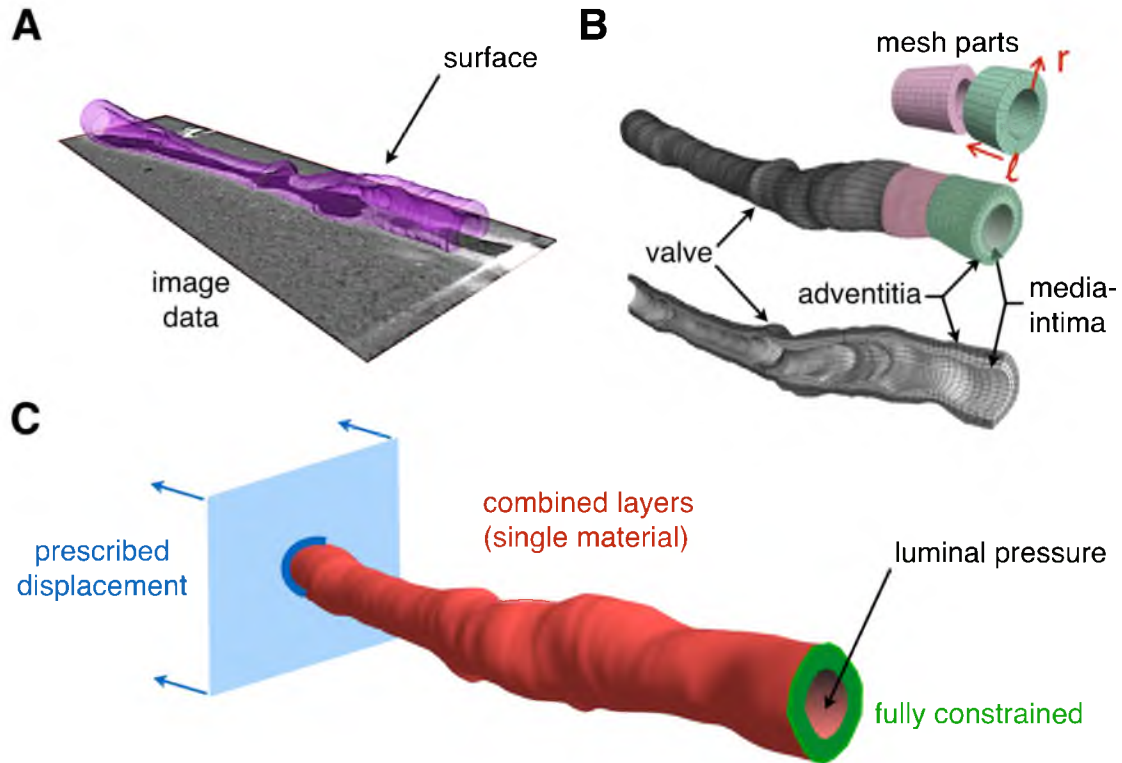


Figure 2.2. Computational modeling of a vein. (A) The vein geometry was extracted from 3D image data by manual segmentation. (B) The computational mesh was constructed by projecting cylindrical parts onto the segmented surface. A cross-sectional cut of computational mesh shows the approximate location of media-intima and adventitia layers. In practice, layers are merged and described by a single material. (C) Boundary conditions akin to an inflation-extension experiment include prescribed displacements and pressure on the internal surface.

collagen fiber bundles aligned mostly in the longitudinal direction but with a small diagonal component, longitudinally aligned elastin fibers, and vascular cells. Additional radial elastin fibers are common to the middle and outer layers, which suggests an organized structure [64]. In arterial tissue, the tunica media provides the largest contribution to the mechanical response to loading [65], [66], but the same observation is yet to be made in the vein due to experimental constraints dealing with thin tissue [63]. Nevertheless, progress has been made in terms of expressing the constitutive properties of vein tissue across different species, types of venous tissue, and some disease states [67], [68]. In terms of constitutive behavior, the most promising models consist of inducing an explicit representation of helical (exponential) collagen fibers embedded in an isotropic matrix representative of surrounding elements, mostly of elastin, following a quadratic or exponential response curve [63]. Compared to arterial tissue, the vein is still relatively understudied particularly with respect to contribution of each of its layers, viscoelastic behavior, and fluid-structure interaction. Lack of experimental data, which is present to some extent in most biological problems, carries with it the consequence that, even if anatomical data are available and a mesh can be constructed, a single material would have to be used to express the cumulative mechanical contributions of each layer. The same assumption would have to be used for some common features in vein anatomy, such as valves, so it is desirable to limit modeling to samples without such features, as was done in Chapter 3 (which also showed the basic definition of the strain energy functions used to describe tissue response, and some considerations in terms of residual strain). A basic set of boundary conditions representative of an inflation-extension experiment consists of fixing the

displacement of nodes on a surface at one end of the vein (depending on the experiment, it may be necessary to allow axial rotation), introducing a prescribed axial displacement on the other end, and defining intraluminal pressure on the inside surface (Figure 2.2).

2.5 Special Considerations for Cardiac Biomechanics

Recent years of research on cardiac imaging have yielded key technical developments making simplifying the acquisition of morphological images of the intact or *in vivo* heart, specially healthy ventricles [69], thus most of the complexity behind construction a mechanical modeling off the heart lays on preprocessing. For the purpose of mesh creation, it is possible to obtain anatomical images of reasonable resolution after a relatively short MRI session, although some care must be applied during acquisition (e.g., by adding a bright or black blood preparation to a pulse sequence) to facilitate segmentation of the myocardium later on [48]. Surfaces can be created either from multislice label sets delineating the endocardium and epicardium, or by a combination of short (perpendicular to the ventricular axis) and long (parallel to the ventricular axis) slices by fitting a surface spline on the label data. There are a few strategies for creating hexahedral meshes of the left ventricle, and in some cases it can also be extended for both ventricles. One strategy, described here for completeness purposes only, essentially consists of building a “plugged cylinder” where a hollow cylinder is used around the myocardium, and the plug corresponds to the inner section of the apex. The cylinder can be meshed using a rectangular topology with two connected ends, and the plug with a compatible butterfly pattern [70]. The strategy used in this research is illustrated in Figure 2.3 and consists of creating a mesh part that

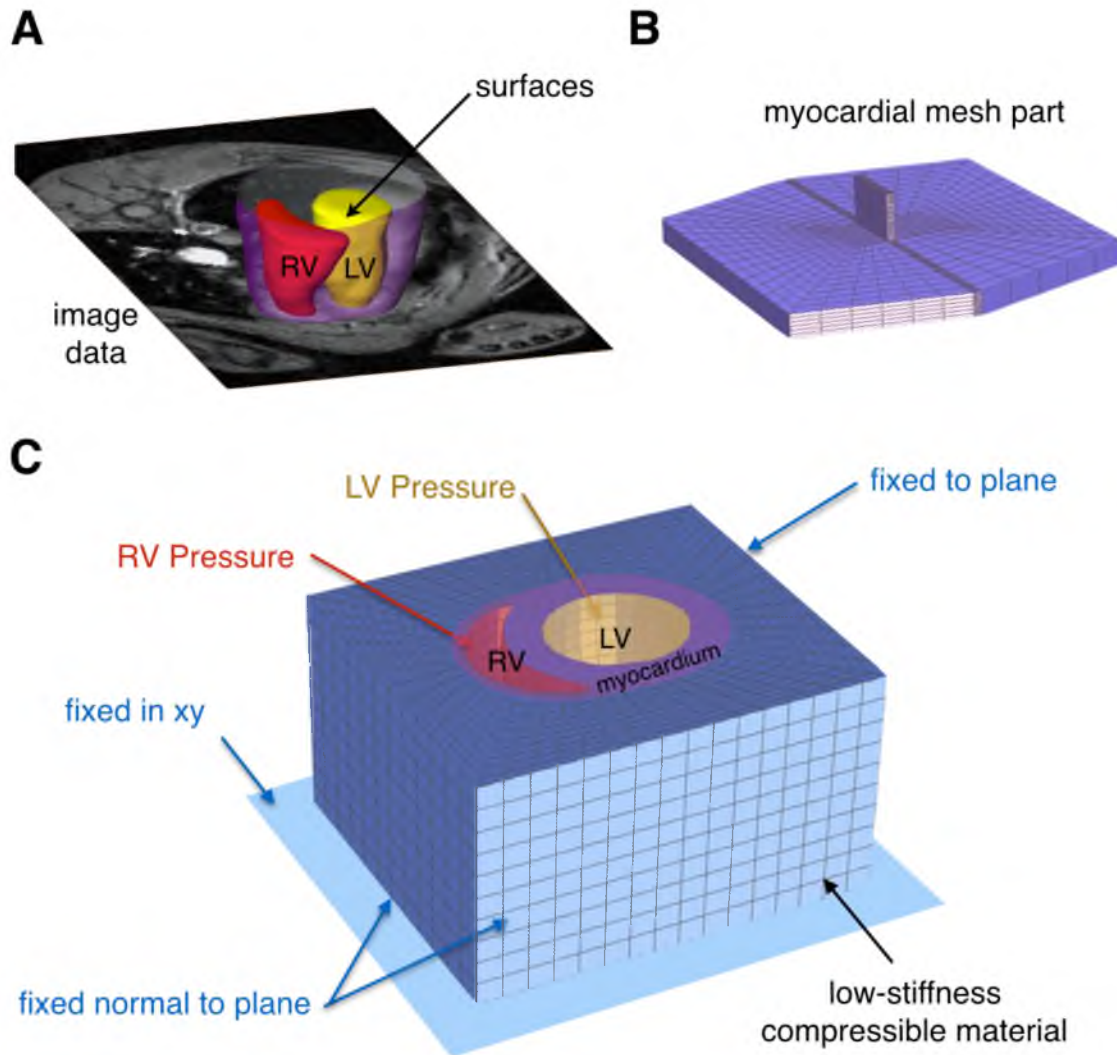


Figure 2.3. Computational Model of the Ventricles. (A) Surfaces corresponding to each cavity and the epicardium were extracted from 3D image data by semi-automatic segmentation. (B) The part used to mesh the myocardium features a butterfly topology. This part is identical for models of the left ventricle alone, except for the central insert, which is used for the septum. (C) The boundary conditions used for the analysis include cavity pressures, fixing the basal cut plane to a plane, and fixing the surrounding material (which has minimum contribution to the deformation of the model) as shown.

“wraps” the epicardium like a blanket [60]. For LV models, this part consists of four rectangular sides around a butterfly part in the center. For biventricular models, two additional sides are introduced and the center is divided into two butterfly meshes and a wall, which gives rise to the septum. The literature shows different sets of boundary conditions including using springs to simulate a fixed base, enforcing contact on a surrounding membrane, having a free epicardial wall and a fully fixed base, and surrounding the ventricles with a support material. The approach used here is a modified version of the latter approach used in previous investigations using a relatively comparable computational environment, where the ventricles are attached to a surrounding material with negligible stiffness forming a block, and the different sides on the block are constrained to planes. Although this approach requires additional steps to recreate the kinematics of the heart (where the apex remains relatively fixed), it allows the base of the heart to radially expand, contract, and rotate. A similar set of boundary conditions can be used in tetrahedral meshes, which can be generated automatically, but conversion to quadratic elements may be necessary to achieve similar results compared to linear hexahedral meshes.

The ventricles as a whole are lined on the outside by the epicardium, which is a thin layer in the order of a tenth of a millimeter composed of irregular connective tissue with a relatively high concentration of collagen and some elastin. This layer is in contact with serous fluid within the pericardial sac. On the inside of the ventricles, the epicardium similar in thickness to the outer layer is composed by collagen, elastin as well as endothelial cells, which are in direct contact with blood. Ventricular myocardial tissue is predominantly (approximately 70% by volume) made up of parallel myocytes

forming nominally branched fibers and layered sheet-like structures that vary in direction depending on their location [71]. Adjacent myocytes are laterally connected by endomysial collagen fibers. At a layer level, sheetlets composed of approximately 3 or 4 myocytes are attached by a collagen-rich perimysium that partly composes cleavage planes [72], [73]. The remaining tissue volume contains vasculature as well as different interstitial components. [52]

As a material, the passive ventricular myocardium has been modeled in several ways with at least two consistent observations across the bulk of the literature: the tissue is not isotropic and it follows a quasi-exponential response [73]–[75]. Some of the ramifications of the first observation were discussed in depth in Chapter 5, but, practically speaking, the construction of a realistic ventricular model must include representation of directional dependency within the strain energy equations as well as the ability to define it on the model. The directional dependency of the material model is expressed within factor Q , the Fung-type hyper elasticity model [74],

$$W = \frac{1}{2}c(e^Q - 1). \quad (2.4)$$

In the model W represents the strain energy of the material, c is a material coefficients with the units of stress, and Q is a function of the components of the Green-Lagrange strain tensor \underline{E} . In a frame-invariant form [76]

$$Q = c^{-1} \sum_{a=1}^3 \left(2\mu_a \underline{A}_a^0 : \underline{E}^2 + \sum_{b=1}^3 \lambda_{ab} (\underline{A}_a^0 : \underline{E})(\underline{A}_b^0 : \underline{E}) \right), \quad (2.5)$$

where

$$\underline{A}_a^0 = \vec{d}_a^0 \otimes \vec{d}_a^0. \quad (2.6)$$

The vectors \vec{d}_a^0 and \vec{d}_b^0 are basis of an orthonormal set that represents the local directionality of the tissue, and μ_a and λ_{ab} are material coefficient sets. Transverse-

isotropic and orthotropic material models arise from aligning \vec{a}_a^0 and \vec{a}_b^0 with the fiber and sheet directions, enabling response to be expressed as a function of local stretches and shears (f for fiber, s for, and n for sheet-normal), or

$$\begin{aligned}
 Q = & c_1 E_{ff}^2 + c_2 E_{ss}^2 + c_3 E_{nn}^2 \\
 & + 2c_4 E_{ff} E_{ss} + 2c_5 E_{ss} E_{nn} + 2c_6 E_{nn} E_{ff} \\
 & + c_7 (E_{fs}^2 + E_{sf}^2) + c_8 (E_{nf}^2 + E_{fn}^2) + c_9 (E_{sn}^2 + E_{ns}^2).
 \end{aligned} \tag{2.7}$$

Neglecting the interaction terms weighted by parameters c_4 , c_5 , and c_6 (i.e., setting these to zero), gives rise to representations used commonly in the literature [73]–[75], including those used in Chapter 5.

Defining the material directions in a computational model is generally achieved by using a local coordinate system [77]. As a first approximation, this process can be simplified by taking advantage of the local orientation of the nodes within a given element. If more sophisticated definitions are desired, a ventricular coordinate system can be obtained by solving differential equations that govern potential distribution in longitudinal (apex to base) and radial (transmural) directions [78]. Then, a set of local coordinate systems can be obtained by calculating the coordinate system's gradients. Finally, the coordinate system can be rotated based on scalar fields that define directional distribution (fiber and sheet structures) across the heart. For example, Figure 2.4 shows the generation of a left-ventricular coordinate system using the finite-element solution for potential distribution obtained with FEBio2 thermal solver. The local coordinate system is equivalent to normalized gradients of the potential, and their cross product. More information about this approach and its extension to biventricular models can be found in previous studies [78].

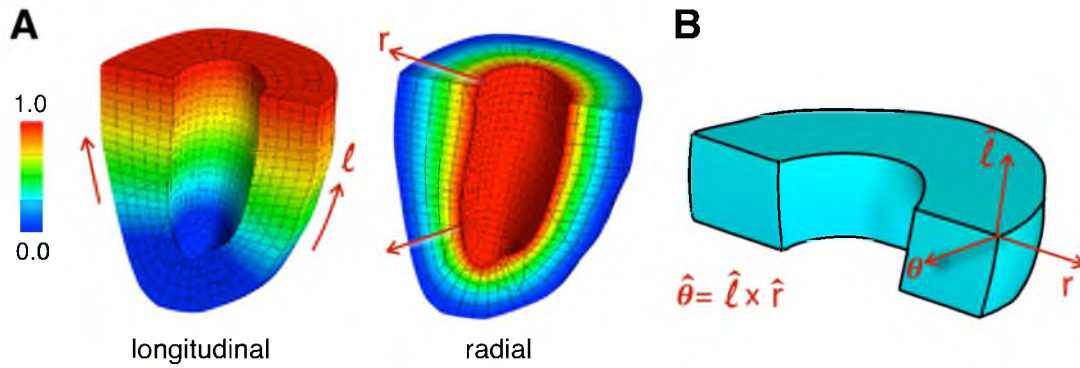


Figure 2.4. Left-ventricular coordinate system. (A) Finite-element solutions of potential distribution based on prescribed temperatures at the apex and base (longitudinal), as well as endo- and epicardium (radial). Normalized gradient vectors can be crossed to define local coordinate systems, like the one illustrated on the epicardial surface. Note that the direction of the system is spatially dependent, and that a set of rotations is needed to align this system in the direction of ventricular fiber and sheet structures.

The most conspicuous aspect of function of the heart is its ability to contract. Basic muscular contraction in the heart is triggered by a specialized process known as cardiac excitation-contraction coupling. It involves signaling pathways (most of them involving calcium ions) that ultimately convert transmembrane voltage variations into changes in force in myocytes. In the heart, electrical signaling from the sinoatrial (and secondarily at atrioventricular) node that eventually causes depolarization of myocytes in atria and ventricles [79]. After depolarization, voltage-gated L-type calcium channels enable extracellular calcium to flow into the cell, where this calcium activates sarcoplasmic ryanodine receptors, which, in turn, allow a flux of calcium stored in the sarcoplasmic reticulum into the cell interior (a process known as calcium-induced calcium release) [80]. Increased intracellular calcium concentration causes calcium to bind to troponin C. This interaction promotes shifting of the troponin-tropomyosin complex as well as changes in the relative arrangement of tropomyosin and actin, which enable interaction between actin and myosin within the sarcomeres. Contraction is produced by relative displacement, or sliding, between actin (thin) and myosin (thick) filament structures. The interaction between actin and myosin, enabled by the presence of sufficient calcium concentration, promotes the ability of myosin ATPase to hydrolyze ATP and convert chemical energy to force generation, or relative motion, via rotation of the myosin cross-bridges or “heads” [81]. The amount of tension applied by sarcomeres is related to the number of number of actin-myosin interactions, and is a function of the level of overlap between thick and thin filaments [82], [83]. The sarcomere length associated with highest overlap produces maximum tension. Contraction or extension beyond the optimal overlap results in a decrease of tension [81], [84]. The roles of calcium and

sarcomere length, briefly described above, constitute two main components of many models of cardiac contraction, which have been previously implemented into FE packages, including FEBio (used for this research). In particular, the “contractility material,” which provides an additive stress component onto the total Cauchy stress was incorporated to the passive myocardial response through a solid mixture [61]. More information can be found in Chapter 5.

2.6 References

- [1] S. L. Murphy, J. Xu, and K. D. Kochanek, “National Vital Statistics Reports Deaths: Final Data for 2010,” National Vital Statistics Reports, vol. 61, no. 4, 2013.
- [2] J. J. V McMurray, S. Adamopoulos, S. D. Anker, et al. “ESC guidelines for the diagnosis and treatment of acute and chronic heart failure 2012: The Task Force for the Diagnosis and Treatment of Acute and Chronic Heart Failure 2012 of the European Society of Cardiology. Developed in collaboration with the Heart,” Eur. Heart J., vol. 33, no. 14, pp. 1787–847, Jul. 2012.
- [3] D. S. Celermajer, C. K. Chow, E. Marijon, N. M. Anstey, and K. S. Woo, “Cardiovascular disease in the developing world: prevalences, patterns, and the potential of early disease detection,” J. Am. Coll. Cardiol., vol. 60, no. 14, pp. 1207–16, Oct. 2012.
- [4] R. L. Bengelink and P. E. Rubbert, “The Impact of CFD on the Airplane Design Process: Today and Tomorrow,” SAE Technical Paper 911989, Sep. 1991.
- [5] D. Peri, M. Rossetti, and E. F. Campana, “Design Optimization of Ship Hulls via CFD Techniques.” J. of Ship Research, vol. 45, no. 2, pp. 140–10, Jun. 2001.
- [6] A. S. Go, D. Mozaffarian, V. L. Roger, E. J. Benjamin, J. D. Berry, et al. “Heart disease and stroke statistics--2014 update: a report from the American Heart Association.” Circulation, vol. 129, no. 3, pp. e28–e292, Jan. 2014.
- [7] J. Wenk, L. Ge, and Z. Zhang, “A coupled biventricular finite element and lumped-parameter circulatory system model of heart failure,” Comput. Methods in Biomechanics and Bioengineering, vol. 16, no. 8, pp. 807–818, 2013.
- [8] D. Tang, C. Yang, T. Geva, G. Gaudette, and P. J. del Nido, “Effect of patch mechanical properties on right ventricle function using MRI-Based two-layer anisotropic models of human right and left ventricles,” Comput. Model. Eng. Sci., vol. 56, no. 2, pp. 113–130, Jan. 2010.
- [9] C. Yang, C. Tang, I. Haber, T. Geva, and P. J. del Nido, “In vivo MRI-based 3D FSI RV/LV models for human right ventricle and patch design for potential computer-aided surgery optimization,” Comput. Struct., vol. 85, no. 11–14, pp. 988–997, 2009.
- [10] X. Song, A. Untaroiu, H. G. Wood, P. E. Allaire, A. L. Throckmorton, S. W. Day, and D. B. Olsen, “Design and transient computational fluid dynamics study of a continuous axial flow ventricular assist device,” ASAIO J., vol. 50, no. 3, pp. 215–24, Jan. .

- [11] T. A. S. Kaufmann, S. D. Gregory, M. R. Büsen, G. D. Tansley, and U. Steinseifer, "Development of a numerical pump testing framework," *Artif. Organs*, vol. 38, no. 9, pp. 783–90, Sep. 2014.
- [12] E. Okamoto, S. Fukuoka, E. Iwazawa, and Y. Mitamura, "Computer assisted design for the implantable left ventricular assist device (LVAD) blood pump using computational fluid dynamics (CFD) and computer-aided design and manufacturing (CAD/CAM)," *J. Artif. Organs*, vol. 4, no. 3, pp. 205–213, Sep. 2001.
- [13] N. F. Voelkel, R. A. Quaife, L. A. Leinwand, R. J. Barst, M. D. McGoon, D. R. Meldrum, J. Dupuis, C. S. Long, L. J. Rubin, F. W. Smart, Y. J. Suzuki, M. Gladwin, E. M. Denholm, and D. B. Gail, "Right ventricular function and failure: report of a National Heart, Lung, and Blood Institute working group on cellular and molecular mechanisms of right heart failure," *Circulation*, vol. 114, no. 17, pp. 1883–91, Oct. 2006.
- [14] L. G. Kevin and M. Barnard, "Right ventricular failure," *Contin. Educ. Anaesthesia, Crit. Care Pain*, vol. 7, no. 3, pp. 89–94, May 2007.
- [15] M. Puhlman, "Continuous-flow left ventricular assist device and the right ventricle," *AACN Adv. Crit. Care*, vol. 23, no. 1, pp. 86–90, 2012.
- [16] M. Meineri, A. E. Van Rensburg, and A. Vegas, "Right ventricular failure after LVAD implantation: prevention and treatment," *Best Pract. Res. Clin. Anaesthesiol.*, vol. 26, no. 2, pp. 217–29, Jun. 2012.
- [17] D. Roy, C. Kauffmann, S. Delorme, S. Lerouge, G. Cloutier, and G. Soulez, "A literature review of the numerical analysis of abdominal aortic aneurysms treated with endovascular stent grafts," *Comput. Math. Methods Med.*, vol. 2012, p. 820389, Jan. 2012.
- [18] C. Martin, W. Sun, and J. Elefteriades, "Patient-specific finite element analysis of ascending aorta aneurysms," *Am. J. Physiol. Heart Circ. Physiol.*, p. ajpheart.00908.2014, Mar. 2015.
- [19] A. A. Owida, H. Do, and Y. S. Morsi, "Numerical analysis of coronary artery bypass grafts: an overview," *Comput. Methods Programs Biomed.*, vol. 108, no. 2, pp. 689–705, Nov. 2012.
- [20] Y. He, C. M. Terry, C. Nguyen, S. A. Berceli, Y. Shiu, and A. K. Cheung, "Serial analysis of lumen geometry and hemodynamics in human arteriovenous fistula for hemodialysis using magnetic resonance imaging and computational fluid dynamics," *J. Biomech.*, vol. 46, no. 1, pp. 165–9, Jan. 2013.
- [21] A. J. Epstein, D. Polsky, L. Yang, and P. W. Groeneveld, "Coronary

- revascularization trends in the United States, 2001-2008,” *JAMA*, vol. 305, no. 17, pp. 2001–2008, 2014.
- [22] A. J. Collins, R. N. Foley, and B. Chavers, “United States Renal data system 2012 annual data report: atlas of chronic kidney disease & end-stage renal disease in the United States,” *Am. J. Kidney Dis.*, vol. 61, no. 1, pp. e1–e480, 2013.
- [23] P. M. McGah, D. F. Leotta, K. W. Beach, and A. Aliseda, “Effects of wall distensibility in hemodynamic simulations of an arteriovenous fistula,” *Biomech. Model. Mechanobiol.*, vol. 13, no. 3, pp. 679–95, Jun. 2014.
- [24] N. Varble, S. Day, D. Phillips, D. Mix, K. Schwarz, K. A. Illig, and A. Chandra, “In vitro hemodynamic model of the arm arteriovenous circulation to study hemodynamics of native arteriovenous fistula and the distal revascularization and interval ligation procedure,” *J. Vasc. Surg.*, vol. 59, no. 5, pp. 1410–7, May 2014.
- [25] J. F. Wenk, K. Sun, Z. Zhang, M. Soleimani, L. Ge, D. Saloner, A. W. Wallace, M. B. Ratcliffe, and J. M. Guccione, “Regional left ventricular myocardial contractility and stress in a finite element model of posterobasal myocardial infarction,” *J Biomech Eng.*, vol. 133, no. 4, pp. 1–14, Apr. 2011.
- [26] K. Sun, N. Stander, C.-S. Jhun, Z. Zhang, T. Suzuki, G.-Y. Wang, S. Maythem, A. W. Wallace, E. E. Tseng, A. J. Baker, D. Saloner, D. R. Einstein, M. B. Ratcliffe, and J. M. Guccione, “A computationally efficient formal optimization of regional myocardial contractility in a sheep with left ventricular aneurysm,” *J. Biomech. Eng.*, vol. 131, no. 11, pp. 1–21, 2009.
- [27] P. Zhang, J. M. Guccione, S. I. Nicholas, J. C. Walker, P. C. Crawford, A. Shamal, G. Acevedo-Bolton, M. A. Guttman, C. Ozturk, E. R. McVeigh, D. A. Saloner, A. W. Wallace, and M. B. Ratcliffe, “Endoventricular patch plasty for dyskinetic anteroapical left ventricular aneurysm increases systolic circumferential shortening in sheep,” *J. Thorac. Cardiovasc. Surg.*, vol. 134, no. 4, pp. 1017–24, Oct. 2007.
- [28] R. Muthupillai and R. L. Ehman, “Magnetic resonance elastography,” *Nat. Med.*, vol. 2, no. 5, pp. 601–3, May 1996.
- [29] Z. Qian, W.-N. Lee, E. E. Konofagou, D. N. Metaxas, and L. Axel, “Ultrasound myocardial elastography and registered 3D tagged MRI: quantitative strain comparison,” *Med. Image Comput. Comput. Assist. Interv.*, vol. 10, no. Pt 1, pp. 800–8, Jan. 2007.
- [30] Y. K. Mariappan, K. J. Glaser, and R. L. Ehman, “Magnetic resonance elastography: a review,” *Clin. Anat.*, vol. 23, no. 5, pp. 497–511, Jul. 2010.
- [31] M. Kauer, V. Vuskovic, J. Dual, G. Szekely, and M. Bajka, “Inverse finite element

- characterization of soft tissues,” *Med. Image Anal.*, vol. 6, no. 3, pp. 275–87, Sep. 2002.
- [32] D. R. Einstein, A. D. Freed, N. Stander, B. Fata, and I. Vesely, “Inverse parameter fitting of biological tissues: a response surface approach,” *Ann. Biomed. Eng.*, vol. 33, no. 12, pp. 1819–30, Dec. 2005.
- [33] T. Elgeti, M. Beling, S. Hirsch, B. Hamm, J. Braun, and I. Sack, “Cardiac MR elastography reveals increased stiffness of the left ventricular endocardium in age and pathology,” in *Proc. Intl. Soc. Mag. Reson. Med.*, 2011, vol. 11, no. 1, p. 1308.
- [34] H. Tzschätzsch, T. Elgeti, S. Hirsch, T. Niendorf, J. Braun, and I. Sack, “Direct elastography of in vivo human heart,” in *Proc. Intl. Soc. Mag. Reson. Med.*, 2011, vol. 45, no. 12, p. 275.
- [35] D. W. Park, G. H. Kruger, J. M. Rubin, J. Hamilton, P. Gottschalk, R. E. Dodde, A. J. Shih, and W. F. Weitzel, “In vivo vascular wall shear rate and circumferential strain of renal disease patients,” *Ultrasound Med. Biol.*, vol. 39, no. 2, pp. 241–52, Feb. 2013.
- [36] W. F. Weitzel, K. Kim, D. W. Park, J. Hamilton, M. O’Donnell, T. J. Cichonski, and J. M. Rubin, “High-resolution ultrasound elasticity imaging to evaluate dialysis fistula stenosis,” *Semin. Dial.*, vol. 22, no. 1, pp. 84–9.
- [37] C. L. Welsh, E. V. R. Dibella, G. Adluru, and E. W. Hsu, “Model-based reconstruction of undersampled diffusion tensor k-space data,” *Magn. Reson. Med.*, Sep. 2012.
- [38] X. Liu, K. Z. Abd-Elmoniem, and J. L. Prince, “Incompressible cardiac motion estimation of the left ventricle using tagged MR images,” *Med. Image Comput. Comput. Assist. Interv.*, vol. 12, no. Pt 2, pp. 331–8, Jan. 2009.
- [39] J. Prince and J. Links, *Medical Imaging Signals and Systems*, 2nd ed. Pearson Higher Education, 2015.
- [40] K. R. Chien, “Cardiac muscle diseases in genetically engineered mice: evolution of molecular physiology,” *Am. J. Physiol.*, vol. 269, no. 3 Pt 2, pp. H755–66, Sep. 1995.
- [41] L. J. Healy, Y. Jiang, and E. W. Hsu, “Quantitative comparison of myocardial fiber structure between mice, rabbit, and sheep using diffusion tensor cardiovascular magnetic resonance,” *J. Cardiovasc. Magn. Reson.*, vol. 13, p. 74, Jan. 2011.
- [42] L. Cunha, I. Horvath, S. Ferreira, J. Lemos, P. Costa, D. Vieira, D. S. Veres, K. Szigeti, T. Summavielle, D. Máthé, and L. F. Metello, “Preclinical imaging: an

- essential ally in modern biosciences,” *Mol. Diagn. Ther.*, vol. 18, no. 2, pp. 153–73, Apr. 2014.
- [43] National Institute of Standards and Technology, “X-Ray mass attenuation coefficients,” *Physical Reference Data*, 2009. [Online]. Available: <http://www.nist.gov/pml/data/index.cfm>.
- [44] L. Martiniova, D. Schimel, E. W. Lai, A. Limpuangthip, R. Kvetnansky, and K. Pacak, “In vivo micro-CT imaging of liver lesions in small animal models,” *Methods*, vol. 50, no. 1, pp. 20–5, Jan. 2010.
- [45] E. M. Haacke, R. W. Brown, M. R. Thompson, and R. Venkatesan, *Magnetic Resonance Imaging: Physical Principles and Sequence Design*. Wiley-Liss; 1st Ed. 1999.
- [46] E. O. Stejskal and J. E. Tanner, “Spin diffusion measurements: spin echoes in the presence of a time-dependent field gradient,” *J. Chem. Phys.*, vol. 42, no. 1, p. 288, Jul. 1965.
- [47] A. H. Aletras, S. Ding, R. S. Balaban, and H. Wen, “DENSE: displacement encoding with stimulated echoes in cardiac functional MRI,” *J. Magn. Reson.*, vol. 137, no. 1, pp. 247–52, Mar. 1999.
- [48] M. A. Bernstein, K. F. King, and X. J. Zhou, *Handbook of MRI Pulse Sequences*. Elsevier Inc., 2004.
- [49] M. O’Donnell, “NMR blood flow imaging using multiecho, phase contrast sequences,” *Med. Phys.*, vol. 12, no. 1, pp. 59–64, Jan. 1985.
- [50] V. M. Runge and M. L. Wood, “Fast imaging and other motion artifact reduction schemes: a pictorial overview,” *Magn. Reson. Imaging*, vol. 6, no. 5, pp. 595–607, Sept. 1988.
- [51] X. Zhong, P. A. Helm, and F. H. Epstein, “Balanced multipoint displacement encoding for DENSE MRI,” *Magn. Reson. Med.*, vol. 61, no. 4, pp. 981–8, Apr. 2009.
- [52] J. D. Humphrey, *Cardiovascular Solid Mechanics*. Springer, 2002.
- [53] Y. C. Fung, *Biomechanics: Mechanical Properties of Living Tissues*, Second Ed. Springer, 1993.
- [54] K. J. Bathe, *Finite Element Procedures*, 2nd Ed. Prentice-Hall, 1996.
- [55] J. Bonet and R. D. Wood, *Nonlinear Continuum Mechanics for Finite Element Analysis*, 1st Ed. Cambridge University Press, 1997.

- [56] P. G. Young, T. B. H. Beresford-West, S. R. L. Coward, B. Notarberardino, B. Walker, and A. Abdul-Aziz, "An efficient approach to converting three-dimensional image data into highly accurate computational models," *Philos. Trans. A. Math. Phys. Eng. Sci.*, vol. 366, no. 1878, pp. 3155–73, Sep. 2008.
- [57] S. D. Daxini and J. M. Prajapati, "A review on recent contribution of meshfree methods to structure and fracture mechanics applications," *ScientificWorldJournal*, vol. 2014, p. 247172, Jan. 2014.
- [58] X. Zhuang, "Challenges and methodologies of fully automatic whole heart segmentation: a review," *J. Healthc. Eng.*, vol. 4, no. 3, pp. 371–408, Jan. 2013.
- [59] F. Vadakkumpadan, H. Arevalo, A. J. Prassl, J. Chen, F. Kickinger, P. Kohl, G. Plank, and N. Trayanova, "Image-based models of cardiac structure in health and disease," *Wiley Interdiscip. Rev. Syst. Biol. Med.*, vol. 2, no. 4, pp. 489–506, Jan. 2012.
- [60] J. M. Guccione, G. Kassab, and M. Ratcliffe, *Computational Cardiovascular Mechanics*, 1st Ed. Springer, 2010.
- [61] S. Maas, D. Rawlings, J. A. Weiss, and G. A. Ateshian, *FEBio: finite elements for biomechanics. Theory Manual*, May, 2014. Salt Lake City, UT, 2014.
- [62] S. A. Maas, B. J. Ellis, G. A. Ateshian, and J. A. Weiss, "FEBio: finite elements for biomechanics," *J. Biomech. Eng.*, vol. 134, no. 1, pp. 011005–1,–10, Jan. 2012.
- [63] D. P. Sokolis, "Experimental investigation and constitutive modeling of the 3D histomechanical properties of vein tissue," *Biomech. Model. Mechanobiol.*, vol. 12, no. 3, pp. 431–51, Jun. 2013.
- [64] J. A. G. Rhodin, "Architecture of the vessel wall," in *Handbook of Physiology*, American Physiology Society by Wiley-Blackwell, 1980.
- [65] A. Pandit, X. Lu, C. Wang, and G. S. Kassab, "Biaxial elastic material properties of porcine coronary media and adventitia," *Am. J. Physiol. Circ. Physiol.*, vol. 288, no. 6, pp. 2581–2587, 2005.
- [66] C. Wang, M. Garcia, and X. Lu, "Three-dimensional mechanical properties of porcine coronary arteries: a validated two-layer model," *Am. J. Physiol. Circ. Physiol.*, vol. 291, no. 3, pp. 1200–1209, 2006.
- [67] E. P. Kritharis, J. D. Kakisis, A. T. Giagini, T. Manos, N. Stergiopoulos, S. Tsangaris, and D. P. Sokolis, "Biomechanical, morphological and zero-stress state characterization of jugular vein remodeling in arteriovenous fistulas for hemodialysis," *Biorheology*, vol. 47, no. 5–6, pp. 297–319, Jan. 2010.
- [68] S. G. Sassani, A. Theofani, S. Tsangaris, and D. P. Sokolis, "Time-course of

venous wall biomechanical adaptation in pressure and flow-overload: assessment by a microstructure-based material model,” *J. Biomech.*, vol. 46, no. 14, pp. 2451–62, Sep. 2013.

- [69] A. Kumar and R. Bagur, “Cardiac magnetic resonance in clinical cardiology,” *World J. Cardiol.*, vol. 7, no. 1, pp. 6–9, Jan. 2015.
- [70] N. S. Phatak, S. A. Maas, A. I. Veress, N. A. Pack, E. V. R. Di Bella, and J. A. Weiss, “Strain measurement in the left ventricle during systole with deformable image registration,” *Med. Image Anal.*, vol. 13, no. 2, pp. 354–61, Apr. 2009.
- [71] D. D. Streeter and W. T. Hanna, “Engineering mechanics for successive states in canine left ventricular myocardium. II. Fiber angle and sarcomere length,” *Circ. Res.*, vol. 33, no. 6, pp. 656–64, Dec. 1973.
- [72] I. J. LeGrice, B. H. Smaill, L. Z. Chai, S. G. Edgar, J. B. Gavin, and P. J. Hunter, “Laminar structure of the heart: ventricular myocyte arrangement and connective tissue architecture in the dog,” *Am. J. Physiol. Circ. Physiol.*, vol. 269, no. 2, pp. H571–H582, 1995.
- [73] G. A. Holzapfel and R. W. Ogden, “Constitutive modelling of passive myocardium: a structurally based framework for material characterization,” *Philos. Trans. A. Math. Phys. Eng. Sci.*, vol. 367, no. 1902, pp. 3445–75, Sep. 2009.
- [74] K. D. Costa, J. W. Holmes, and A. D. McCulloch, “Modelling cardiac mechanical properties in three dimensions,” *Philos. Trans. R. Soc. A Math. Phys. Eng. Sci.*, vol. 359, no. 1783, pp. 1233–1250, Jun. 2001.
- [75] J. M. Guccione, A. D. McCulloch, and L. K. Waldman, “Passive material properties of intact ventricular myocardium determined from a cylindrical model,” *J. Biomech. Eng.*, vol. 113, no. 1, pp. 42–55, Feb. 1991.
- [76] G. A. Ateshian and K. D. Costa, “A frame-invariant formulation of Fung elasticity,” *J. Biomech.*, vol. 42, no. 6, pp. 781–5, Apr. 2009.
- [77] J. H. Omens, D. A. MacKenna, and A. D. McCulloch, “Measurement of strain and analysis of stress in resting rat left ventricular myocardium,” *J. Biomech.*, vol. 26, no. 6, pp. 665–676, Jun. 1993.
- [78] J. D. Bayer, R. C. Blake, G. Plank, and N. A. Trayanova, “A novel rule-based algorithm for assigning myocardial fiber orientation to computational heart models,” *Ann. Biomed. Eng.*, vol. 40, no. 10, pp. 2243–54, Oct. 2012.
- [79] D. Silverthorn, *Human physiology: an integrated approach*, 3rd. ed. Pearson, 2004.

- [80] A. Fabiato and F. Fabiato, "Contractions induced by a calcium-triggered release of calcium from the sarcoplasmic reticulum of single skinned cardiac cells," *J. Physiol.*, vol. 249, no. 3, pp. 469–95, Aug. 1975.
- [81] D. M. Bers, *Excitation-Contraction Coupling and Cardiac Contractile Force*, vol. 237. Dordrecht: Springer Netherlands, 2001.
- [82] D. M. Bers, "Cardiac excitation-contraction coupling," *Nature*, vol. 415, no. 6868, pp. 198–205, Jan. 2002.
- [83] J. M. Guccione and A. D. McCulloch, "Mechanics of active contraction in cardiac muscle: Part I--Constitutive relations for fiber stress that describe deactivation," *J. Biomech. Eng.*, vol. 115, no. 1, pp. 72–81, Feb. 1993.
- [84] J. M. Guccione, L. K. Waldman, and A. D. McCulloch, "Mechanics of active contraction in cardiac muscle: Part II--Cylindrical models of the systolic left ventricle," *J. Biomech. Eng.*, vol. 115, no. 1, pp. 82–90, Feb. 1993.

CHAPTER 3

CHARACTERIZATION OF REGIONAL DEFORMATION AND MATERIAL PROPERTIES OF THE INTACT EXPLANTED VEIN BY MICROCT AND COMPUTATIONAL ANALYSIS¹

3.1 Abstract

Detailed mechanical information of the vein is important to better understand remodeling of the vessel in disease states, but has been difficult to obtain due to its thinness, unique geometry, and limitations of mechanical testing. This study presents a novel method for characterizing deformation of the intact explanted vein under physiological loads and determining its material properties by combining high-resolution imaging and computational analysis. High-resolution CT (microCT) was used to image an iodine-stained, excised porcine internal jugular vein sample under extension to 100% and 120% of *in situ* length, and inflation and 2, 10, 20 mmHg of pressure, inside a microCT-compatible hydrostatic loading chamber. Regional strains were measured with the finite element (FE) image registration method known as Hyperelastic Warping. Material properties were approximated with inverse FE characterization by optimizing stiffness-related coefficients so as to match simulated

¹Reprinted with permission from Springer. Arnold David Gomez, Huashan Zou, Yan-Ting Shiu, and Edward W. Hsu. Characterization of Regional Deformation and Material Properties of the Intact Explanted Vein by MicroCT and Computational Analysis. *Journal of Cardiovascular Engineering and Technology*. DOI 10.1007/s13239-014-0190-x. The final publication is available at springerlink.com.

strains to the experimental measurements. The observed morphology and regional strain of the vein were found to be relatively heterogeneous. The regional variability in the measured strain was primarily driven by geometry. Although iodine treatment may result in tissue stiffening, which requires additional investigation, it is effective in allowing detailed detection of vein geometry. The feasibility and utility of using microCT and computational analysis to characterize mechanical responses and material properties of the vein were demonstrated. The presented method is a promising alternative or addition to mechanical testing for characterizing veins or other similarly delicate vessels in their native anatomical configuration under a wide range of realistic or simulated environmental and loading conditions.

3.2 Introduction

Disorders of the vein, either developed natively (e.g., varicose veins) or after surgery (e.g., arterial vein grafts), are frequently associated with altered mechanical loading conditions on the vessel that result in compromised wall structure, luminal blood flow, or both, with potentially detrimental consequences. [1]–[3] In turn, quantitative characterization for material properties can be helpful for monitoring disease progression. For example, compliance variations indicative of development of neointimal hyperplasia can be localized with wall strain measurements in venous grafts used for arterial bypass surgery [4]. Because vessel wall dilation is a key determinant for the maturation of arteriovenous fistula used for vascular access, stiffness or stiffening of the graft can contribute to maturation failure [3], [5], [6]. The feedback pathways between increased loading and remodeling of the venous wall have been

thought to be responsible for conditions like varicose veins and venous neointimal hyperplasia. [2], [3], [5], [7], [8] Because the vein wall is composed of tissues that exhibit viscoelasticity in their constitutive behavior, a precise knowledge of the relationship between its fluidic or nonfluidic environmental loading and macroscopic morphology is essential to characterize the material properties and responses of the vessel, and help elucidate the mechanisms of the remodeling process. For these reasons, biomechanical characterization of venous tissue has been performed via biaxial testing of small samples as well as inflation and extension of whole vessels [9]–[12], among other means.

Traditionally, material properties of tissues have been obtained primarily through mechanical testing, which has been instrumental in the construction of phenomenological constitutive models of many tissues, including arteries, and to a much lesser extent veins, that are in use today [9], [10], [12]. In a typical mechanical testing experiment, whole-sample deformation and load quantification are embedded in the testing apparatus by means of hardware-based displacement sensors like magnetic or optical encoders [13]. Alternatively, to characterize regional properties, the tissue is outfitted with fiducial markers, whose displacements are then tracked via, for example, photography when the tissue is subject to different loads [14], [15]. Because these examinations can be done in the laboratory where loading and environmental conditions can be precisely controlled, mechanical testing is still considered as the standard technique for detailed characterization of the material properties of many tissues including blood vessels[16]. The main drawbacks of mechanical testing of these types of tissues are its destructive nature, the loss of a blood vessel's native anatomical

configuration, and inherent limitations associated with physical examinations (e.g., number and spatial resolution of the measurements) [13].

Because of their noninvasive or nondestructive nature, imaging-based methods are increasingly used for tissue deformation and material characterization. For example, magnetic resonance imaging (MRI) and ultrasound imaging have been used to track regional tissue deformation based on the inherent tissue contrast via the so-called texture correlation and speckle tracking analyses, respectively [4], [17]. Trackable patterns in the form of grid patterns can also be generated in a process called “tagging” in MRI [18]. Alternatively, regional deformation of tissues is directly measured via motion-sensitive imaging such as phase-contrast velocity and displacement-encoding MRI, and Doppler ultrasonography [19], [20]. Although computed tomography (CT) provides the highly desirable combination of spatial resolution, image quality and acquisition speed, it has been seldom utilized due to its limited soft-tissue contrast. However, in light of recent advances in specimen staining techniques that make otherwise undetectable details of tissues visible [21], [22], CT-based deformation measurements are now conceptually feasible and worth exploring. The 3D feature offered by CT is especially desirable as basis for comprehensive mechanical analysis, since the morphology and, thus, mechanical responses of veins occur in all spatial directions.

Besides image acquisition, an integral part of imaging-based deformation characterization is the underlying computational analysis. Image processing is often used to enhance and isolate features of interest necessary for the identification of tissues and markers as deformation takes place [23], [24]. Further, image registration methods,

utilizing rigid or nonrigid deformation, have been employed to replace visual inspection for automated tissue tracking, which can be obtained with image correlation [17], or similarity measures like mutual information [25] and local contrast [26], [27]. Although each deformation type and registration metric can be advantageous in different specific applications, in general, the accuracy of image registration in capturing the underlying motion increases as more degrees of freedom are allowed in the deformation. To counter numerical instability associated with ill-conditioning due to increasing degrees of freedom, the registration formulation is often regularized with physics-based processes, such as diffusion, fluidic advection, or solid deformation [26]–[28].

The advent of computational image analysis has also made it possible to approximate the constitutive behavior of tissues by means of inverse finite element (FE) approaches, which can provide a way to circumvent the physical limitations of mechanical testing. Whereas traditional forward FE simulations are used to predict tissue deformation according to conservation principles based on given information about load conditions and constitutive behavior, inverse parameter estimation seeks to infer material parameters based on known loads and deformation [29], [30]. Imaging-based inverse material characterization, counter-intuitively, is performed by iterative material property optimization using forward simulations, and has been applied in soft tissues, including the liver [31] and the heart [32]. Provided that images of sufficient resolution and contrast are obtainable for accurate quantification of the local tissue strain [29], and the range of strains resembles biaxial data, i.e., like in extension-inflation vessel analysis, this technique is expected to be uniquely beneficial for material characterization of vein samples, especially in diseased vessels where even

small changes can be significant but difficult to detect via physical examinations.

The overall purpose of the study is to investigate the feasibility of novel means of high-resolution imaging with computational analysis to perform functional and material characterization in thin-walled veins. This includes the development of experimental protocols for using high-resolution CT, or microCT, to capture local microscopic-scale features of vein specimens in 3D under load, and application of computational analysis on images obtained under a controlled-loading scenario to quantify deformation and material properties of the vessel. The experimental considerations include the description of a microCT-compatible experimental setup and tissue contrast enhancement procedures. On the computational side, this study demonstrates the use of image registration for strain measurement in these types of images, and subsequent material characterization via inverse FE analysis. Hyperelastic Warping [28], [33], [34] was selected as the means for image registration because it is integrated with FE analysis, making it particularly convenient for the current study where the material modeling parameters are themselves the subject of investigation.

3.3 Methods

3.3.1 Imaging

3.3.1.1 MicroCT-Compatible Pressurization Apparatus

Based on previous evaluations of large artery mechanics under pressure and other loads [14], [35], [36], a microCT-compatible apparatus was constructed to provide varying physiological pressurization of the vein. The system has small physical size to allow close rotation of the X-ray source required for high-resolution CT acquisition, and

is mostly made out of plastic material to reduce artifacts associated with large attenuation coefficient differences [37]. Figure 3.1 shows a schematic of the entire apparatus designed to accommodate veins of various diameters. The sample was mounted on miniature barb adapters and secured with surgical thread at each end of the phosphate-buffered saline (PBS)-filled test chamber. The adapter was designed to allow extension of the vein sample as well as pressurization, and was fitted with a removable plug for purging air bubbles. Hydrostatic pressurization ranging from 0 to 180 mmHg was achieved via a PBS column, whose level was maintained by the small flow (0.5 ml/min maximum) introduced by a roller pump to compensate for vessel permeability or inadvertent leaks at the tissue-adapter connections.

3.3.1.2 Sample Preparation

Animal protocols were approved by the Institutional Animal Care and Use Committees at the Veterans Affairs Salt Lake City Health Care System and the University of Utah. One external jugular and one subcutaneous abdominal vein samples, each about 30 mm in length, were harvested from 3-month-old female Yorkshire cross domestic pigs (Sigma Livestock, USA) used as control animals at the end-time points of an unrelated study. Due to logistical constraints, the subcutaneous abdominal vein was used immediately after excision, whereas the jugular specimen was frozen (-80 °C) and used within 3 h from thawing before changes in mechanical properties take place [38].

Although the relationship between pretreatment with Lugol's solution and soft tissue contrast has been established in previous microCT visualization of embryonic and

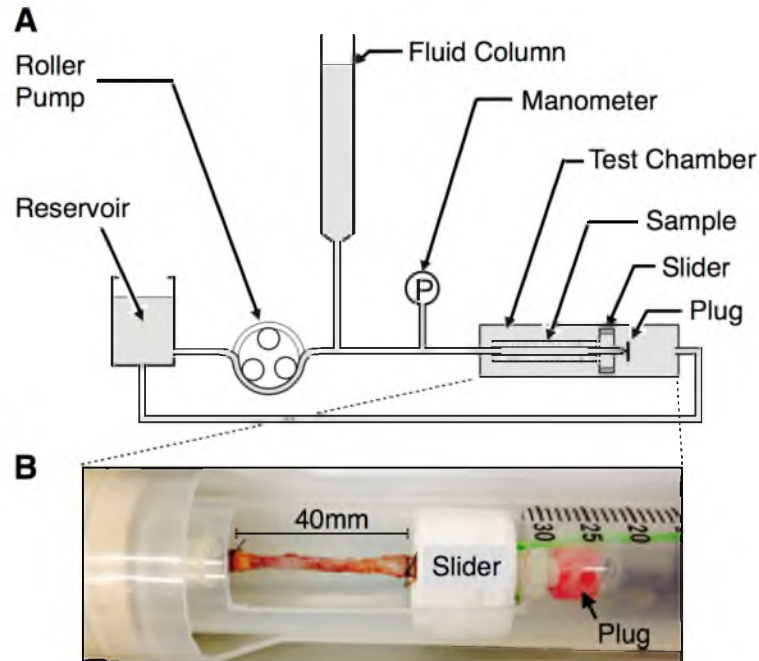


Figure 3.1: MicroCT-compatible pressurization apparatus. The schematic (A) illustrates the overall system designed to allow imaging of the vessel under different loading conditions. The photograph (B) shows the actual study specimen mounted in the test chamber obtained after microCT imaging, with surrounding fluid and chamber cover removed for clarity. Notice the coloration of the specimen due to iodine staining.

cardiovascular tissues [21], [22], the protocol needs to be optimized for vein specimens. To this end, the subcutaneous abdominal vein sample was divided into eleven 3-mm-long sections, and one section was soaked in each 0, 5, 10 or 20% Lugol's solution (cat# 26385-06, Electron Microscopy Sciences, USA) for 1.0, 2.0, or 3.0 h. The starts of the different soaking procedures were timed such that the sections could be imaged together. For the stretching and pressurization experiment, the jugular vein sample was pretreated using the duration and concentration deemed minimally sufficient to produce detectable contrast (5% for 1 h).

3.3.1.3 MicroCT

For the pretreatment optimization experiment, the vein sections were placed inside a PBS-filled 3.0 ml syringe serving as sample holder, and imaged on a Siemens Inveon instrument (Siemens Medical Solutions, PA, USA). 3D images of 23 x 23 x 55 mm field-of-view with 17 μm voxels were acquired using 701 projections with the source operating at 80 kVp and 120 μA , which took 60 min. In postprocessing, the image contrast, for each vein section was quantified by,

$$\text{contrast} = \frac{H_t - H_b}{H_b}, \quad (3.1)$$

where H_t and H_b were the average Hounsfield intensities of the tissue and the background, respectively.

For the pressurization experiment, the pretreated sample was rinsed in PBS, mounted on the pressurization apparatus, and imaged using the same protocol, except with reduced resolution (100 μm) to minimize scan time (18 min) to minimize possible contrast reduction due to diffusion. The jugular vein was first imaged in its unloaded

state, which corresponded to approximately 60% shrinkage from its *in situ* length. The sample was then stretched to its estimated *in situ* length (100%) and imaged at each 2, 10, and 20 mmHg pressurization. Finally, the vein was stretched to 1.2 times its *in situ* length (120%), and imaged at the same pressure levels.

3.3.2 Computational Mechanics

For completeness, some useful theoretical concepts are briefly reviewed. In equations, vectors are identified with arrow accents and tensors with underbars.

3.3.2.1 Theoretical Background

In this study, deformation was quantified by comparing tissue coordinates in a reference (i.e., unloaded) configuration, \vec{X} , with corresponding locations in a current (deformed) configuration, \vec{x} , via the Right Cauchy strain tensor [39],

$$\underline{C} = \left(\frac{d\vec{x}}{d\vec{X}} \right)^T \frac{d\vec{x}}{d\vec{X}}, \quad (3.2)$$

which is used to define constitutive modeling relationships. For visualization, the circumferential component of the Green-Lagrange strain tensor,

$$\underline{E} = \frac{1}{2} [\underline{C} - \underline{1}] \quad (3.3)$$

($\underline{1}$ indicates the identity matrix), was shown in color maps.

In hyperelastic materials, often used to model venous tissue [9], [10], a scalar strain energy function, W , may be used to relate strain to stress, via the second Piola-Kirchhoff stress tensor [39],

$$\underline{P} = 2 \frac{\partial W}{\partial \underline{C}}, \quad (3.4)$$

which allows the formulation of constitutive material models by defining a strain energy function, W , that fits experimentally obtained strain-stress responses, or predictions of deformation of an FE model under idealized loads.

Strain measurement via image registration is commonly achieved by finding the deformation map that minimizes a given measure of similarity between two images [26]–[28]. Assuming intensities represent body points in reference and current configurations, images acquired before and after a deformation can be expressed as scalar fields known as the template, $T(\vec{X})$, and target $S(\vec{x})$, respectively. By comparing local intensity differences, it is possible to construct a scalar similarity measure that approaches zero as one image is deformed into the other. One such metric is the image energy, [26], [28]

$$U(\vec{X}, \vec{x}) = \frac{1}{2} [T(\vec{X}) - S(\vec{x})]^2. \quad (3.5)$$

Compared to other registration strategies using Equation 3.5, Hyperelastic Warping is unique in that the desired deformation field minimizes the image energy, U , along with the material-specific strain energy function, W , by means of the FE method. [28], [33], [34] Thus, given a set of images, geometrical, and constitutive FE modeling, the main criterion for finding \vec{x} (or strain via Equations 3.2-3.4) is the minimization of the net energy Ψ of a system in volume β ,

$$\Psi(\vec{x}) = \lambda \int_{\beta} U(\vec{X}, \vec{x}) dv - \int_{\beta} W(\vec{X}, \vec{x}) dv, \quad (3.6)$$

where λ weights the relative contribution of image information. As formulated, image energy terms effectively provide loading by means of body forces, which are consequently equilibrated by internal stresses associated to deformation. [33], [40]

3.3.2.2 Geometrical and Constitutive Modeling

To construct the FE model required for deformation measurements, the sample's geometry was obtained from images acquired at the unloaded configuration by segmentation (Amira, FEI Visualization, Germany), and rendered in hexahedral-elements (True Grid, XYZ Scientific Applications, USA). To minimize segmentation error resulting in geometrical noise, boundary surfaces were smoothed before rendering (MeshLab, ISTI-CNR, Italy). The model consisted of 9250 elements—37, 125, and 2 along the vessel circumference, length, and wall thickness, respectively. Local mesh refinement was applied to preserve element quality and sample geometry. Mesh density was tested with a maximum-strain convergence analysis by simulating 60-mmHg pressurization at 100% *in situ* length with 3, 6, 9, 15, and 23 thousand-element meshes.

The jugular vein tissue was modeled as anisotropic fiber-reinforced composite based on the microstructural model described in [41] where tissue response was represented by exponential fibers embedded in a nonlinear matrix. For its finite element analysis, the matrix was implemented using the nonlinear description by Veronda and Westmann [42] with the strain energy,

$$W_{matrix} = c_1 \left[e^{c_2(\bar{I}_1 - 3)} - 1 \right] - \frac{c_1 c_2}{2} [\bar{I}_2 - 3] + \frac{K}{2} (\ln J)^2 \quad (3.7)$$

with $J = \det(d\vec{x}/d\vec{X})$, \bar{I}_1 and \bar{I}_2 as first and second invariants of the deviatoric Right Cauchy strain tensor ($\underline{C}_{dev} = J^{2/3} \underline{C}$ from Equation 3.1) [39], and the following material-specific coefficients: c_1 (in kPa) and c_2 (dimensionless). These regulate stiffness, and K (in kPa) as bulk modulus. The four fiber families were implemented as unidirectional exponential reinforcements with strain energy density given by:

$$W_{fibers} = \sum_{m=1}^4 \frac{\xi^{(i)}}{2\alpha^{(i)}} (\exp [\alpha^{(i)}(\bar{I}_n - 1)^2] - 1) \quad (3.8)$$

where $\xi^{(i)}$ and $\alpha^{(i)}$ correspond to material coefficients of the i -th fiber $i \in \{1, 2, 3, 4\}$ and \bar{I}_n is the projection of the Right Cauchy strain tensor along the fiber direction (the square of the fiber stretch). Fiber directionality within the local element coordinates was set by the angular distance, $\varphi^{(i)}$, with $\varphi^{(3)} = 0^\circ$ corresponding to circumferential, $\varphi^{(3)} = 90^\circ$ to longitudinal, and $\varphi^{(1)} = -\varphi^{(2)}$ to oblique fibers, respectively. The cumulative response of the fibers and the matrix was implemented as an uncoupled solid mixture, where the strain energy density of the composite material was $W = W_{matrix} + W_{fibers}$ [43], [44], given the assumption of near-incompressible behavior enforced by a relatively large bulk modulus of 5000 kPa. To evaluate the influence of material assumptions on the strain measurement, three sets of material coefficients were obtained by least-squares fit of anisotropic stress-strain curves (Equations 3.7 and 3.8) to published experimental data from seven jugular vein samples (Figure 3.2, based on [10]): the first set corresponds to fitting the model response to the mean strain-stress relationship and is henceforth referred to as “*baseline*” material. The second and third sets correspond to best fits of the model response to the upper and lower experimental ranges producing “*compliant*” and “*stiff*” materials, respectively. Material coefficients are presented in Table 3.1. Response curves for the material sets appear in Figure 3.2.

3.3.2.3 Strain Measurement via Hyperelastic Warping Analysis

Strain measurements at each of the loading scenarios were performed with each of the material responses (“baseline,” “compliant,” and “stiff” materials, respectively) to

Table 3.1. Material Coefficient Sets

	c_1	c_2	$\xi^{(1,2)}$	$\alpha^{(1,2)}$	$\varphi^{(1,2)}$	$\xi^{(3)}$	$\alpha^{(3)}$	$\xi^{(4)}$	$\alpha^{(4)}$
	[kPa]	[-]	[kPa]	[-]	[deg]	[kPa]	[-]	[kPa]	[-]
<i>“baseline”</i>	1.94	0.60	2.65e-6	4.42	62	5.87e-6	3.78	8.22e-5	0.61
<i>“stiff”</i>	2.52	0.61	2.90e-6	4.86	62	6.46e-6	4.16	9.04e-5	0.67
<i>“complia”</i>	1.36	0.63	1.86 e-6	3.27	62	5.28e-6	3.40	7.38e-5	0.55

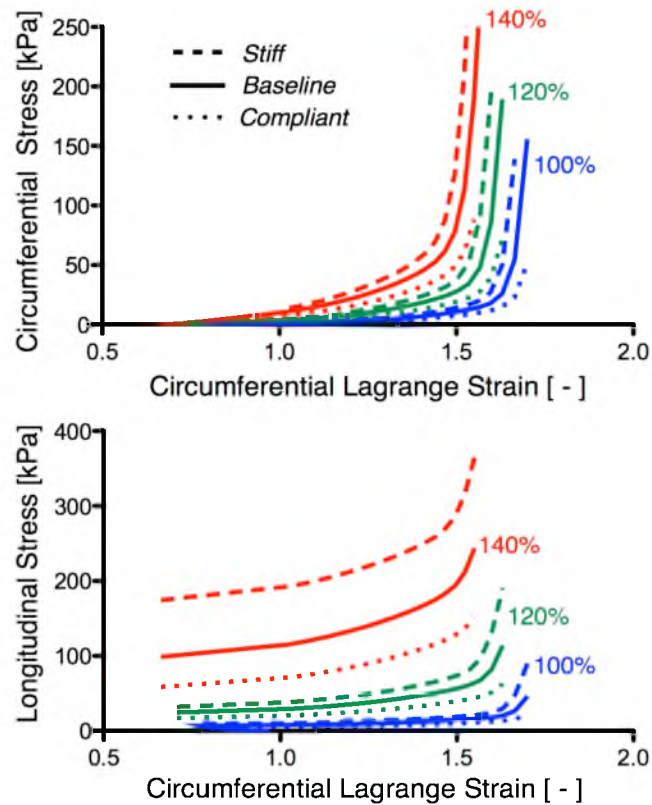


Figure 3.2: Stress-strain responses of the material models used in all computational analyses. Anisotropic stress-strain curves (solid lines) for various degrees of extension (indicated by the specified color) reflect least squares fitted results based on empirical data from inflation-extension tests of jugular vein samples [10]. Both circumferential (top) and longitudinal (bottom) responses are shown. From the “baseline” responses, two material coefficient sets, “compliant” and “stiff” (dotted and dashed lines, respectively), were obtained.

determine if image-based strain measurements via Hyperelastic Warping were independent of material properties and could be used for inverse parameter identification. To this end, Hyperelastic Warping was performed as implemented and described previously [40], [45], [46] using the FEBio software suite [43]. The reference configuration was defined as the unloaded configuration and its corresponding microCT imagery was used as the template volume for Hyperelastic Warping. The images from each of the loading scenarios were used as warping targets. For large deformations, small auxiliary loads were implemented to place the model in the vicinity of the deformed configuration and then increasing the image weighting parameter, λ , (Equation 3.6) until registration forces are predominant and drive the system towards registration. Differences in deformation results were identified by strain map comparison, and with the use of scatter plots.

3.3.2.4 Material Property Estimation

Ideally, material properties could be inferred by iteratively running physics-based simulations driven by loads equivalent to those applied experimentally, comparing the resulting strain field to that observed empirically, and using the difference as feedback. For example, a simulated strain field that was lower than experimental measurement would indicate that the stiffness in the model was too high, and vice versa [29], [30]. In practice, the existence and uniqueness of an optimization solution could be complicated by the large number of optimization variables [47]. For simplification, parameter identification was reduced to scaling coefficients for the matrix parameter c_1 , and for modification of the fiber coefficients $\xi^{(i)}$, and $\alpha^{(i)}$ in order to influence the low and

high range of load-dependent stiffness, respectively.

Physics-based FE simulations for optimization utilized the geometry described in the Geometrical and Constitutive Modeling section (3.3.2.2) but were not driven by image information. Instead, the forward analyses were used to simulate each of the loading scenarios under restricted nodal displacements, or fixed boundary conditions, at the ends of the sample similar to the pressurization apparatus. Axial deformation was prescribed in the code, but longitudinal force data could be used when available. The difference between the Green-Lagrange strain tensor components found experimentally via Hyperelastic Warping and forward simulation, E_{ij} and \hat{E}_{ij} , respectively, was quantified by the total residual RMS, $\varepsilon = \sum \varepsilon_m$. In turn, the residual RMS for the m -th loading scenario investigated, $m \in \{1, 2, 3, 4\}$, representing 100% and 120% extension under 10 and 20 mmHg pressurization over N elements in the analysis region was calculated by

$$\varepsilon_m = \sqrt{\frac{1}{N} \sum_{n=1}^N \left[\sum_{i=1}^3 \sum_{j=1}^3 (E_{ij}^{(n)} - \hat{E}_{ij}^{(n)})^2 \right]}. \quad (3.9)$$

To avoid the influence of edge effects, strains at the end of the sample were excluded, and the residual RMS computation was performed in the middle region of the model. Minimization of the total residual RMS, ε , using a multivariable derivative-free method [47] was scripted in Matlab (The Mathworks, USA) and interfaced with FEBio, which was used for forward simulations. For interpretation of results, the load-specific residual RMS, ε_m , was used as a measurement of the quality of the forward simulations for each loading scenario.

3.4 Results

Figure 3.3 shows microCT slices of the subcutaneous abdominal vein sections pretreated with different concentrations of Lugol's solution for different durations, along with local contrast quantifications. As expected, contrast increased with either concentration or duration, albeit each relationship is not proportional. Maximum contrast, 0.83, was obtained by soaking specimen sections for 2 h in 20% Lugol's solution. The contrast achieved in all the pretreated specimens was deemed sufficient for image segmentation. Although not all of the treatments were used for the pressurization experiments, structural features desirable for image registration (e.g., texture or brighter areas) can be seen in all samples, especially in the tissue treated with relatively higher concentrations (>10%). To reduce possible tissue shrinkage or material property alterations associated with higher concentrations [21], the treatment with lowest concentration and shortest soaking time (5%, 1h) was selected for use in the pressurization experiments

Selected microCT slices of the jugular vein sample at the unload configuration and the investigated loading scenarios are shown in Figure 3.4. Stretching with near-zero pressure loading produced visible reduction in the vessel diameter and wall thickness, as expected due to tissue incompressibility. Vessel collapse was not observed at low pressurization, nor was buckling seen during hypertension. The sample spanned approximately 900, 100 μm -thick slices, but because its ends were tied to the adapters, only center slices (about 640) showed conspicuous deformation characterized by larger luminal diameter, wall thinning, and rounder circumference compared to the unpressurized states. Figure 3.4 also contains some additional features, such as a

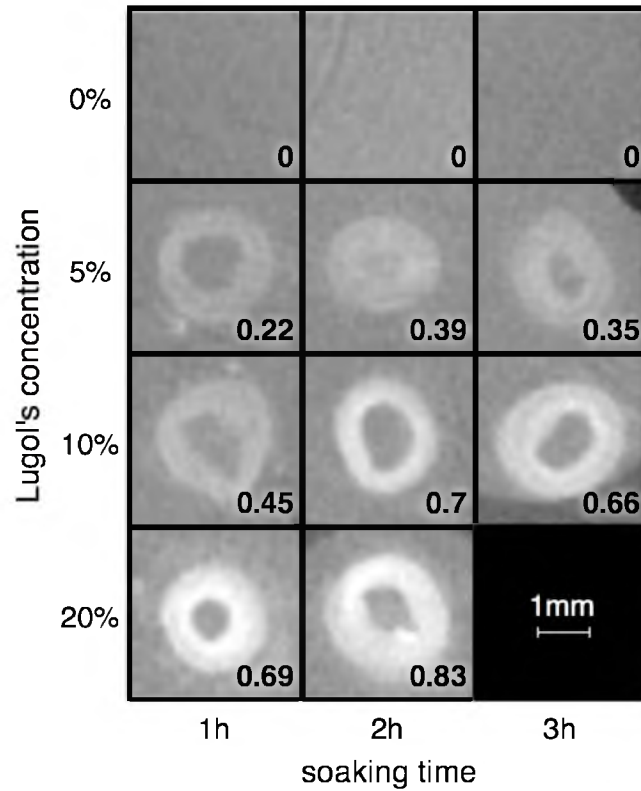


Figure 3.3: Dependence of CT contrast on soaking time and solution concentration. Each panel shows a vein cross section, and quantified contrast, obtained after pretreatment with different Lugol's solution concentration (vertical) and soaking duration (horizontal). Unstained specimens (top row) were invisible.

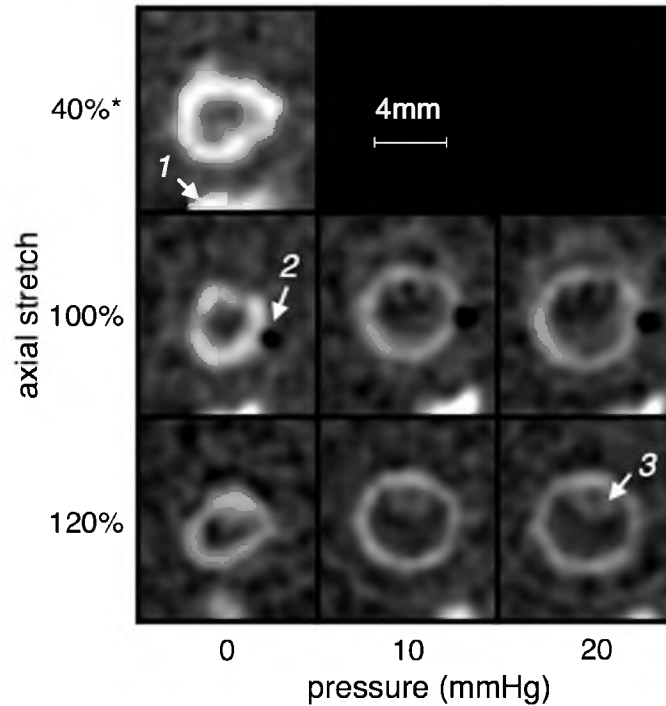


Figure 3.4: MicroCT images of a vein sample under load. The cross-sectional slices were obtained at approximately the same location of the same specimen under the specified stretching and pressurization conditions. The axial stretch is given in terms of the specimen's *in vivo* length, with 40% being the unloaded length. The intensity and contrast of the images have been enhanced to better visualize the vein. The bright region at the bottom of each image (1) is from a piece of remnant connective tissue attached to the vein. A small air bubble (2) and ring-like instrumentation off-center rotation artifacts (3) are also visible.

remnant of connective tissue, a small air bubble, and imaging artifacts (as noted in the figure caption), but these were not included in the generated model geometry and hence had minimum impact on the results.

In the construction of the computational model, mesh density convergence was determined to occur with 9,250 elements, because a 5% change in strain maxima was observed compared to the solution using 15,000 elements. For computational efficiency, given the large number of simulations needed for the study, the 9,250-element-mesh was used for subsequent analysis. Average computational time for forward simulations and Hyperelastic Warping was approximately 45 min on a 12-core, 2 GHz machine (AMD Opteron 6234).

Figure 3.5 shows longitudinal microCT slices, 3D mesh renderings, and photos (obtained after the pressurization experiments) of the internal jugular vein specimen in two of the deformed configurations, 100% to 120% extension at near-zero pressurization, which are representative of the other loading scenarios (not shown). The computational model captured the macroscopic deformation of the specimen, as evident in the microCT and optical imagery. Moreover, some large microscopic morphological features unique to the sample under investigation, like variations in diameter, also deformed consistently with visual inspection of the images. Microscopic morphological features are expected to contribute to regional strain distribution.

Representative results of the Hyperelastic Warping analysis are shown in Figure 3.6, which includes circumferential strain maps and comparative scatter plot of the x, y and z components of the Green-LaGrange strain obtained for 100% extension with 20 mmHg pressurization. Despite using three distinctly different material coefficient sets,

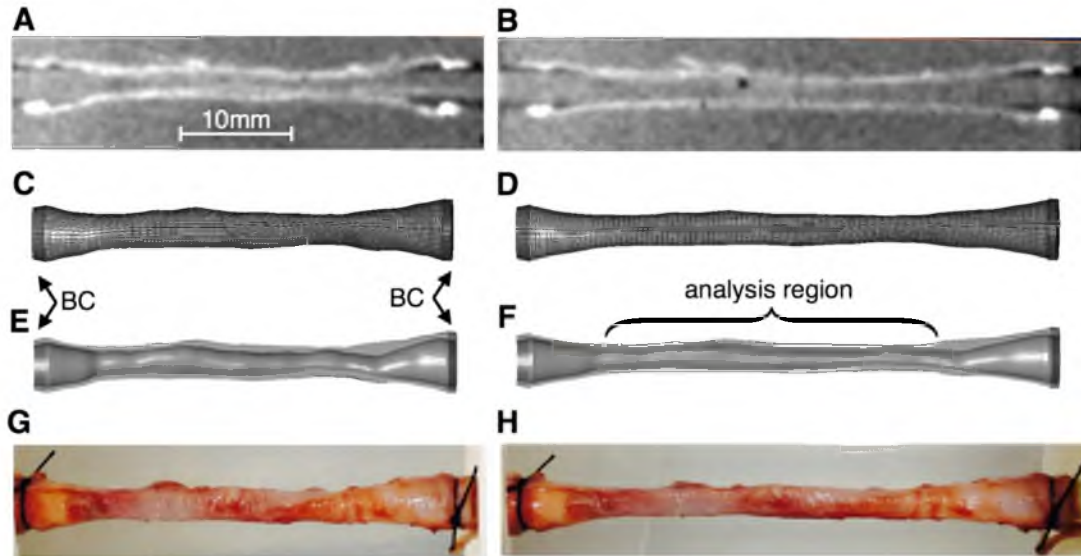


Figure 3.5: Computational model geometry. The left and right columns correspond to 100%- and 120%-stretched states of the same specimen. The microCT images (A and B) were segmented to generate the vessel wall. The computational mesh representations, in whole (C and D), and cut (E and F), illustrate the relatively heterogeneous diameter and wall thickness of the vessel. In order to reduce possible artifacts arising from boundary condition locations (BC), the computational analysis was performed over only the indicated region. Photos of the vessel (G and H) taken after the imaging experiment are included for reference.

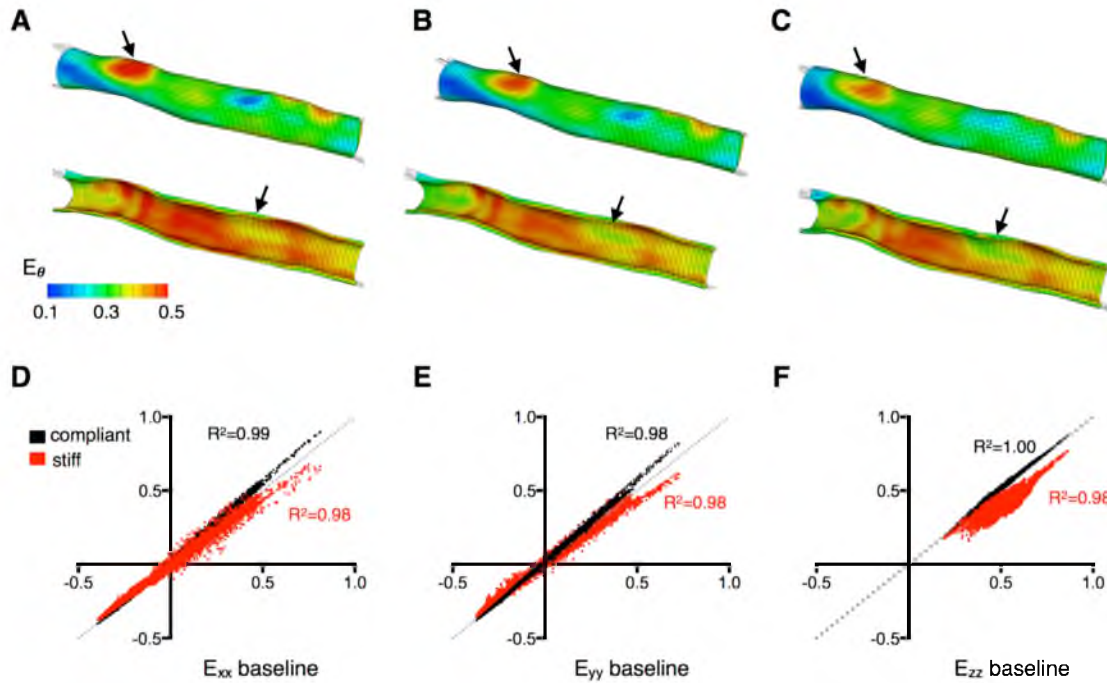


Figure 3.6: Hyperelastic Warping strain measurement. The whole and cut-away color-coded maps (A—C) show largely similar circumferential strain despite the three different sets of material assumptions used. Examples of where minor differences exist are pointed out by the matching arrows. The scatter plots (D—F) directly comparing strain tensor components obtained under different material assumptions reveal slightly overestimated and underestimated deformation when the “compliant” and “stiff” materials were used, respectively.

the circumferential strain maps are highly similar with few noticeable regional differences (e.g., at noted locations on the strain maps). Overall, the circumferential strain varied from approximately 0.11 to 0.60 for the vessel exterior, and 0.29 to 0.59 for its interior. To a first approximation, the ranges of strain observed on the vessel wall are consistent with the increase of the vessel OD (from approximately 3.2 mm in the unloaded state to 3.8 mm in the stretched and inflated state) seen in the CT cross-sectional images (see Figure 3.4). Generally, similarly consistent patterns were also observed in the responses at different loading scenarios (not shown).

Figure 3.6 also shows scatter plots directly comparing selected Green-Lagrange strain components (E_{xx} , E_{yy} and E_{zz}) between different material assumptions (“compliant” versus “baseline,” and “stiff” versus “baseline”). The high coefficients of determination, $R^2 \geq 0.98$, of the scatter plots are consistent with the highly similar strain maps. The independence of strain results from material assumptions is a direct consequence of imaging information playing the predominant role in Hyperelastic Warping, which does not preclude minor differences due to the need for fine tuning the registration parameter for each material. Not surprisingly, the general trend in the scatter plots indicates that softer materials slightly overestimated strain, consistent with observations in the circumferential strain maps. Scatter plots of other strain tensor components (not shown) followed the same trends. These small differences translated to a residual RMS of approximately 0.05 across all components of strain tensor from the investigated loading scenarios, in agreement with a prior study of tissue inflation using the same technique and similar image quality [45].

Figure 3.7 shows circumferential strain maps from physics-based FE simulations

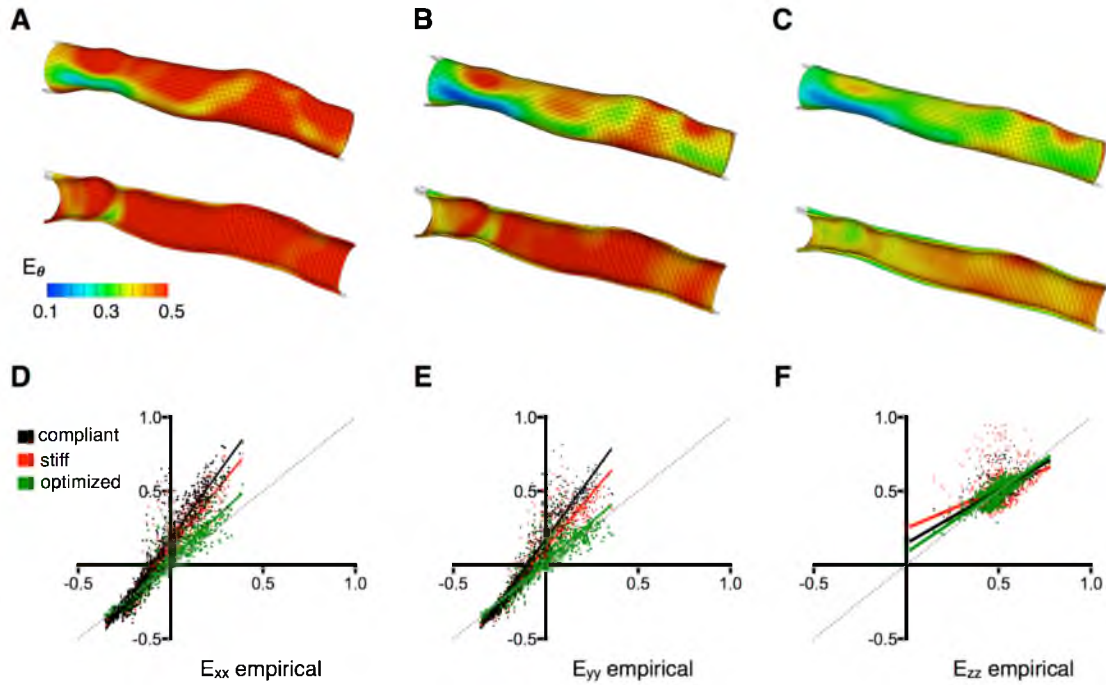


Figure 3.7: Forward FE simulations of the pressurized vein. Whole and cut-open circumferential strain maps obtained for the vein specimen at 100% stretch and 20 mmHg pressurization using "compliant" (A), "stiff" (B), and optimized (C) coefficient sets demonstrate the dependency of simulation results on material assumptions. The scatter plots of the strain tensor components (D–F) comparing between material assumptions indicate that both "compliant" and "stiff" materials overestimate the deformation. For clarity, the number of data points in the scatter plots have been down-sampled by a factor of 10.

using different material coefficient sets, and comparison of strain results of simulated strain results with respect to experimental measurements. The results of “baseline” coefficients can be readily inferred from the behaviors the “compliant” and “stiff” models shown (respectively labeled A and B in Figure 3.7). In general, under identical loads, both the “compliant” and “stiff” models result in markedly more deformation. The trend of behavior is consistent with the scatter plots, where the similarity between strains obtained by forward simulations and Hyperelastic Warping increases with the relative stiffness of the material being tested.

As expected, the circumferential strain map obtained using the optimized material parameters (Figure 3.7-C) shows good agreement with the empirical measurements (Figure 3.6) over a majority, roughly 70% of the surfaces displayed, with isolated areas of larger disagreement. The optimization procedure reduced the cumulative residual RMS from an initial value of 2.52 in the “baseline” material to a final value of 1.02. This affords a quality improvement in simulations from 0.63 to 0.19 in the 100%-stretch 10 mmHg pressurization, 0.90 to 0.43 in the 100%-stretch 20 mmHg, and 0.73 to 0.21 in the 120% 20 mmHg pressurization, but slightly elevated simulation residuals for the 120%-stretch 10 mmHg pressurization scenario (RMS increase from 0.41 to 0.46 per Equation 3.9).

The optimized parameters are $c_1 = 5.77$, $\xi^{(1,2)} = 3.11 \times (10)^{-6}$, $\xi^{(3)} = 6.93 \times (10)^{-7}$, $\xi^{(4)} = 1.01 \times (10)^{-5}$, and $\alpha^{(1,2)} = 5.22$, $\alpha^{(3)} = 4.47$, $\alpha^{(4)} = 0.73$, which roughly indicate an increase of matrix relative stiffness (via c_1) by 300% and fiber stiffness of 30%.

3.5 Discussion

The results demonstrate that, an accordingly optimized protocol (Figure 3.3), recently developed iodine tissue-staining techniques [21], [22] can also be applied on the explanted vein. The staining pretreatment allowed the vessel's morphology (Figure 3.5) and function, like deformation (Figures 3.4 and 3.6), to be evaluated in 3D and high-resolution using microCT and the appropriate testing apparatus. While a voxel dimension of 100 μm is used in the present study, higher resolution is possible with specialized instrumentation. Even with the current image resolution and quality, the results reveal detailed 3D geometry including vessel diameter and wall thickness non-uniformities despite the microscopic size of these features.

The present study also demonstrates the feasibility of coupling high-resolution CT-based geometrical characterization with computational analysis to examine functional behaviors of the vein sample. The image-driven strain analysis, as shown in Figure 3.6, shows a direct assessment of vein deformation under a loading condition that mimics its native environment and anatomical configuration. Although optical-based methods [48], [49] are also noninvasive and nondestructive, due to the limitation of light penetration, they capture only surface motion and necessitate invoking incompressibility assumptions for reconstruction of 3D information. These approaches surpass the quasi-temporal resolution of CT (i.e., intermediate imagery as pressurization occurs) making them suitable for material model form investigation. In contrast, CT imagery delivers high spatial resolution in full 3D. This allows determination of strain in complex shapes like bifurcations and fistula interfaces, which are not readily suited for optical methods. In addition to the spatial resolution in which the measurements are made, the findings

suggest that image-based functional and material analysis can be a desirable alternative or adjunct to specialize a given material model to a specific specimen, particularly in situations like examination of very small and highly fragile samples without sectioning or clamping them.

Importantly, once functional characterization is complete, computational analysis based on the same geometrical and material model can be used to examine tissue responses under a variety of loading settings, including ones that are beyond physiological conditions. As shown in Figure 3.7, material assumptions can affect the accuracy of deformation simulations. In the present study, in order to explain the discrepancy between simulated and empirical strains, the relative stiffness of the material had to be increased. The precise cause of the apparent tissue stiffening is currently unclear, but can include material property changes caused by the iodine staining, or intrinsic differences between the tissues used to obtain the initial material model and the tissue used in this investigation. Despite this result, qualitative agreement between simulated and measured strain distribution indicates that over the majority of the structure under investigation, the strain distribution is primarily driven by geometrical spatial variations due to vessel morphology. Additional minor differences may be attributed to spatial variations in material properties or other unaccounted modeling assumptions. Combined, the characterization of the regional (Figures 3.6-C and 3.7-C) as well as macroscopic response (Figure 3.5), indicate that the proposed methodology is a potentially useful means for multiscale mechanical analysis of the vein.

Being a proof-of-concept study, there are several ways in which the current work

can be improved. One obvious concern relates to the use of a single specimen in the current study. Although justified for the purpose of demonstration, a rigorous validation study based on multiple specimens and direct comparison to mechanical testing is needed to establish the accuracy of the measurements. Similarly, despite soaking the tissue in the lowest concentration of Lugol's solution and for the shortest duration deemed practical for imaging, whether there has been any adverse effect, and if so, whether the effect can be avoided (e.g., by further lowering exposure to the treatment solution or using an alternative solution) remain to be investigated. Another source of concern is the simplistic nature of assumptions made in the geometric and material modeling (e.g., homogeneous material properties) in order to focus on the complete analysis workflow and its feasibility. While there is general agreement between the Hyperelastic Warping results (Figure 3.6) and the physics-driven simulations (Figure 3.7) with optimized material parameters, the assumptions likely have contributed to the observed localized discrepancies. Likewise, because the reference configuration used in this study (the unpressurized state) is assumed to be completely unloaded, the forward simulations would have the tendency to overestimate deformation if prestrain is present in the tissue. The accuracy of the predictions can likely be improved by using more sophisticated modeling.

Despite the potential limitations, findings of the current study are promising for future work in image-based computational mechanics in the vein. As a start, as shown in arteries [35], [50] and some venous tissues [10], [36], it is possible to perform a more generalized analysis including spatially heterogeneous material characterization. However, depending on its application, the number of degrees of freedom involving

spatial characterization would render results susceptible to artifacts due to local minima, numerical ill conditioning, and a large computational expense. These challenges could be addressed, for instance, by parameterizing coefficients along the spatial directions; for instance by using polynomial and sinusoidal functions. Further, fluidic loads may be included by coupling the presented analysis with computational fluid dynamics [5], which can be valuable for understanding the mechanisms involved in varicose vein formation and venous neointimal hyperplasia, or improving arteriovenous fistulas, hemodialysis grafts, and vessels for cardiac bypass. Finally, although demonstrated for microCT, the computational analysis presented here is compatible with most imaging modalities, including *in vivo* applications, provided that sufficient resolution and contrast are achievable to capture relevant morphological features in 3D. For example, Hyperelastic Warping has already been used for *in vivo* strain characterization of tissues, including ligaments [51], coronary artery [34], and heart [51]. Given the continuing advances in MRI resolution, ultrasound imaging quality, and CT contrast, if not already feasible, it is just a matter of time until *in vivo* characterization of functional and material properties of the vein using this approach becomes a reality.

3.6 Acknowledgements

The authors thank the University of Utah's Musculoskeletal Research Laboratories for assistance in Hyperelastic Warping implementation, and Drs. Christi Terry, Huan Li, and Alfred K. Cheung, and Ilya Zhuplatov for providing experimental samples. Brian Watson, Daniel Pike and Michelle Fitts are also gratefully acknowledged.

3.7 Funding Sources

NIH grants R01-HL67646, R01-HL092055, DK088777, and R01DK100505.

3.8 Conflicts of Interest

Arnold David Gomez, Huashan Zou, Yan-Ting Shiu, and Edward W. Hsu declare that they have no conflicts of interest.

3.9 Statement of Human Studies

No human studies were carried out by the authors for this article.

3.10 Statement of Animal Studies

Animal protocols followed all institutional and national guidelines for the care and use of laboratory animals including approval by the Institutional Animal Care and Use Committees at the Veterans Affairs Salt Lake City Health Care System and the University of Utah.

3.11 References

- [1] R. Y. Kanterman, T. M. Vesely, T. K. Pilgram, B. W. Guy, D. W. Windus, and D. Picus, "Dialysis access grafts: anatomic location of venous stenosis and results of angioplasty," *Radiology*, vol. 195, no. 1, pp. 135–9, Apr. 1995.
- [2] C. P.-Y. Rohan, P. Badel, B. Lun, D. Rastel, and S. Avril, "Biomechanical response of varicose veins to elastic compression: a numerical study," *J. Biomech.*, vol. 46, no. 3, pp. 599–603, Feb. 2013.
- [3] H. Haruguchi and S. Teraoka, "Intimal hyperplasia and hemodynamic factors in arterial bypass and arteriovenous grafts: a review," *J. Artif. Organs Off. J. Japanese Soc. Artif. Organs.*, vol. 6, no. 4, pp. 227–35, Jan. 2003.
- [4] P. Patel, R. Biswas, D. Park, T. J. Cichonski, M. S. Richards, J. M. Rubin, S. Phan, J. Hamilton, and W. F. Weitzel, "Characterization of vascular strain during in-vitro angioplasty with high-resolution ultrasound speckle tracking," *Theor. Biol. Med. Model.*, vol. 7, no. 36, Jan. 2010.
- [5] Z. Kharboutly, M. Fenech, J. M. Treutenaere, I. Claude, and C. Legallais, "Investigations into the relationship between hemodynamics and vascular alterations in an established arteriovenous fistula," *Med. Eng. Phys.*, vol. 29, no. 9, pp. 999–1007, Nov. 2007.
- [6] W. D. Paulson, "Does vascular elasticity affect arteriovenous fistula maturation?" *Open Urol. Nephrol. J.*, vol. 7, no. 1, pp. 26–32, May 2014.
- [7] H. M. Atta, "Varicose veins: role of mechanotransduction of venous hypertension," *Int. J. Vasc. Med.*, vol. 2012, p. Article ID 538627, Jan. 2012.
- [8] L. Li, C. M. Terry, Y.-T. E. Shiu, and A. K. Cheung, "Neointimal hyperplasia associated with synthetic hemodialysis grafts," *Kidney Int.*, vol. 74, no. 10, pp. 1247–61, Nov. 2008.
- [9] T. Pham and W. Sun, "Comparison of biaxial mechanical properties of coronary sinus tissues from porcine, ovine and aged human species," *J. Mech. Behav. Biomed. Mater.*, vol. 6, pp. 21–9, Feb. 2012.
- [10] D. P. Sokolis, "Experimental investigation and constitutive modeling of the 3D histomechanical properties of vein tissue," *Biomech. Model. Mechanobiol.*, vol. 12, no. 3, pp. 431–51, Jun. 2013.
- [11] R. Martinez, C. A. Fierro, P. K. Shireman, and H.-C. Han, "Mechanical buckling of veins under internal pressure," *Ann. Biomed. Eng.*, vol. 38, no. 4, pp. 1345–53, Apr. 2010.

- [12] R. J. Gusic, M. Petko, R. Myung, J. William G, and K. J. Gooch, "Mechanical properties of native and ex vivo remodeled porcine saphenous veins," *J. Biomech.*, vol. 38, no. 9, pp. 1770–9, Sep. 2005.
- [13] L. Tian and N. C. Chesler, "In vivo and in vitro measurements of pulmonary arterial stiffness: a brief review," *Pulm. Circ.*, vol. 2, no. 4, pp. 505–17, Oct. 2012.
- [14] J. Kim and S. Baek, "Circumferential variations of mechanical behavior of the porcine thoracic aorta during the inflation test," *J. Biomech.*, vol. 44, no. 10, pp. 1941–7, Jul. 2011.
- [15] M. J. Thubrikar, S. K. Roskelley, and R. T. Eppink, "Study of stress concentration in the walls of the bovine coronary arterial branch," *J. Biomech.*, vol. 23, no. 1, pp. 15–26, Jan. 1990.
- [16] C. A. J. Schulze-Bauer and G. A. Holzapfel, "Determination of constitutive equations for human arteries from clinical data," *J. Biomech.*, vol. 36, no. 2, pp. 165–9, Feb. 2003.
- [17] C. L. Gilchrist, J. Q. Xia, L. A. Setton, and E. W. Hsu, "High-resolution determination of soft tissue texture correlation," *IEEE Trans. Med. Imaging*, vol. 23, no. 5, pp. 546–553, 2004.
- [18] L. Axel and L. Dougherty, "Heart wall motion: improved method for spatial modulation of magnetization for mr imaging," *Radiology*, vol. 172, no. 2, pp. 349–350, 1989.
- [19] H. Zhou and J. E. Novotny, "Cine phase contrast MRI to measure continuum Lagrangian finite strain fields in contracting skeletal muscle," *J. Magn. Reson. Imaging*, vol. 25, no. 1, pp. 175–84, Jan. 2007.
- [20] P. N. T. Wells and H. Liang, "Medical ultrasound: imaging of soft tissue strain and elasticity," *J. R. Soc. Interface*, vol. 8, no. 64, pp. 1521–49, 2011.
- [21] K. Degenhardt, A. C. Wright, D. Horng, A. Padmanabhan, and J. A. Epstein, "Rapid 3D phenotyping of cardiovascular development in mouse embryos by micro-CT with iodine staining," *Circ. Cardiovasc. Imaging*, vol. 3, no. 3, pp. 314–22, May 2010.
- [22] A. J. Kim, R. Francis, X. Liu, W. A. Devine, R. Ramirez, S. J. Anderton, L. Y. Wong, F. Faruque, G. C. Gabriel, W. Chung, L. Leatherbury, K. Tobita, and C. W. Lo, "Microcomputed tomography provides high accuracy congenital heart disease diagnosis in neonatal and fetal mice," *Circ. Cardiovasc. Imaging*, vol. 6, no. 4, pp. 551–9, Jul. 2013.
- [23] N. C. F. Codella, H. Y. Lee, D. S. Fieno, D. W. Chen, S. Hurtado-Rua, M.

- Kochar, J. P. Finn, R. Judd, P. Goyal, J. Schenendorf, M. D. Cham, R. B. Devereux, M. Prince, Y. Wang, and J. W. Weinsaft, "Improved left ventricular mass quantification with partial voxel interpolation: in vivo and necropsy validation of a novel cardiac MRI segmentation algorithm," *Circ. Cardiovasc. Imaging*, vol. 5, no. 1, pp. 137–46, Jan. 2012.
- [24] K. Kawaji, N. C. F. Codella, M. R. Prince, C. W. Chu, A. Shakoob, T. M. LaBounty, J. K. Min, R. V Swaminathan, R. B. Devereux, Y. Wang, and J. W. Weinsaft, "Automated segmentation of routine clinical cardiac magnetic resonance imaging for assessment of left ventricular diastolic dysfunction," *Circ. Cardiovasc. Imaging*, vol. 2, no. 6, pp. 476–84, Nov. 2009.
- [25] F. Maes, a Collignon, D. Vandermeulen, G. Marchal, and P. Suetens, "Multimodality image registration by maximization of mutual information," *IEEE Trans. Med. Imaging*, vol. 16, no. 2, pp. 187–98, Apr. 1997.
- [26] G. E. Christensen, R. D. Rabbitt, and M. I. Miller, "Deformable templates using large deformation kinematics," *IEEE Trans. Image Process.*, vol. 5, no. 10, pp. 1435–47, Jan. 1996.
- [27] J. P. Thirion, "Image matching as a diffusion process: an analogy with Maxwell's demons," *Med. Image Anal.*, vol. 2, no. 3, pp. 243–260, 1998.
- [28] R. D. Rabbitt, J. A. Weiss, G. E. Christensen, and M. I. Miller, "Mapping of hyperelastic deformable templates using the finite element method," in *SPIE 2573, Vision Geometry IV*, 1995, vol. 2573, pp. 252–265.
- [29] M. Kauer, V. Vuskovic, J. Dual, G. Szekely, and M. Bajka, "Inverse finite element characterization of soft tissues," *Med. Image Anal.*, vol. 6, no. 3, pp. 275–87, Sep. 2002.
- [30] D. R. Einstein, A. D. Freed, N. Stander, B. Fata, and I. Vesely, "Inverse parameter fitting of biological tissues: a response surface approach," *Ann. Biomed. Eng.*, vol. 33, no. 12, pp. 1819–30, Dec. 2005.
- [31] A. Nava, E. Mazza, M. Furrer, P. Villiger, and W. H. Reinhart, "In vivo mechanical characterization of human liver," *Med. Image Anal.*, vol. 12, no. 2, pp. 203–16, Apr. 2008.
- [32] J. F. Wenk, K. Sun, Z. Zhang, M. Soleimani, L. Ge, D. Saloner, A. W. Wallace, M. B. Ratcliffe, and J. M. Guccione, "Regional left ventricular myocardial contractility and stress in a finite element model of posterobasal myocardial infarction," *J. Biomech. Eng.*, vol. 133, no. 4, pp. 1–14, Apr. 2011.
- [33] J. A. Weiss, A. I. Veress, and G. T. Gullberg, "Strain measurement using deformable image registration," in *Mechanics of Biological Materials*, 2006, pp.

489–501.

- [34] A. I. Veress, J. A. Weiss, G. T. Gullberg, D. G. Vince, and R. D. Rabbitt, “Strain measurement in coronary arteries using intravascular ultrasound and deformable images,” *J. Biomech. Eng.*, vol. 124, pp. 734–41, Dec. 2002.
- [35] J.-J. Hu, T. W. Fossum, M. W. Miller, H. Xu, J.-C. Liu, and J. D. Humphrey, “Biomechanics of the porcine basilar artery in hypertension,” *Ann. Biomed. Eng.*, vol. 35, no. 1, pp. 19–29, Jan. 2007.
- [36] K. Hayashi, K. Mori, and H. Miyazaki, “Biomechanical response of femoral vein to chronic elevation of blood pressure in rabbits,” *Am. J. Physiol. Circ. Physiol.*, vol. 284, no. 2, pp. H511–8, Feb. 2003.
- [37] T. M. Buzug, *Computed Tomography: From Photon Statistics to Modern Cone-Beam CT*. Springer, 2008, p. 522.
- [38] L. J. Brossollet and R. P. Vito, “The effects of cryopreservation on the biaxial mechanical properties of canine saphenous veins,” *J. Biomech. Eng.*, vol. 119, no. 1, pp. 1–5, Mar. 1997.
- [39] G. A. Holzapfel, T. C. Gasser, and R. W. Ogden, “A new constitutive framework for arterial wall mechanics and a comparative study of material models,” *J. Elast. Phys. Sci. Solids*, vol. 61, no. 1–3, pp. 1–48, Jul. 2000.
- [40] N. S. Phatak, S. A. Maas, A. I. Veress, N. A. Pack, E. V. R. Di Bella, and J. A. Weiss, “Strain measurement in the left ventricle during systole with deformable image registration,” *Med. Image Anal.*, vol. 13, no. 2, pp. 354–61, Apr. 2009.
- [41] D. P. Sokolis, S. Sassani, E. P. Kritharis, and S. Tsangaris, “Differential histomechanical response of carotid artery in relation to species and region: mathematical description accounting for elastin and collagen anisotropy,” *Med. Biol. Eng. Comput.*, vol. 49, no. 8, pp. 867–79, Aug. 2011.
- [42] D. R. Veronda and R. A. Westmann, “Mechanical characterization of skin-finite deformations,” *J. Biomech.*, vol. 3, no. 1, pp. 111–24, Jan. 1970.
- [43] S. A. Maas, B. J. Ellis, G. A. Ateshian, and J. A. Weiss, “FEBio: finite elements for biomechanics,” *J. Biomech. Eng.*, vol. 134, no. 1, pp. 011005–1–10, Jan. 2012.
- [44] G. A. Ateshian, “On the theory of reactive mixtures for modeling biological growth,” *Biomech. Model. Mechanobiol.*, vol. 6, no. 6, pp. 423–45, Nov. 2007.
- [45] A. I. Veress, G. T. Gullberg, and J. A. Weiss, “Measurement of strain in the left ventricle during diastole with cine-mri and deformable image registration,” *J.*

Biomech. Eng., vol. 127, no. 7, pp. 1195–1207, Jul. 2005.

- [46] A. D. Gomez, S. S. Merchant, and E. W. Hsu, “Accurate high-resolution measurements of 3-d tissue dynamics with registration-enhanced displacement encoded MRI,” *IEEE Trans. Med. Imaging*, vol. 33, no. 6, pp. 1350–62, Jun. 2014.
- [47] J. C. Lagarias, J. A. Reeds, M. H. Wright, and P. E. Wright, “Convergence properties of the Nelder-Mead simplex method in low dimensions,” *SIAM J. Optim.*, vol. 9, pp. 112–147, 1998.
- [48] J. Ning, V. G. Braxton, Y. Wang, M. A. Sutton, and S. M. Lessner, “Speckle patterning of soft tissues for strain field measurement using digital image correlation: preliminary quality assessment of patterns,” *Microsc. Microanal.*, vol. 17, no. 1, pp. 81–90, Feb. 2011.
- [49] K. Genovese, Y. U. Lee, and J. D. Humphrey, “Novel optical system for in vitro quantification of full surface strain fields in small arteries: I. Theory and design,” *Comput. Methods in Mechanobiology*, vol. 14, no. 3, pp. 213–225, 2011.
- [50] C. Wang, M. Garcia, and X. Lu, “Three-dimensional mechanical properties of porcine coronary arteries: a validated two-layer model,” *Am. J. Physiol. Circ. Physiol.*, vol. 291, no. 3, pp. 1200–1209, 2006.
- [51] N. Phatak, Q. Sun, S.-E. Kim, D. Parker, K. Sanders, A. Veress, B. Ellis, and J. A. Weiss, “Noninvasive determination of ligament strain with deformable image registration,” *Ann. Biomed. Eng.*, vol. 35, no. 7, pp. 1175–87, Jul. 2007.

CHAPTER 4

ACCURATE HIGH-RESOLUTION MEASUREMENTS OF 3D TISSUE DYNAMICS WITH REGISTRATION-ENHANCED DISPLACEMENT ENCODED MRI¹

4.1 Abstract

Displacement fields are important to analyze deformation, which is associated with functional and material tissue properties often used as indicators of health. MRI techniques like DENSE and image registration methods like Hyperelastic Warping have been used to produce pixel-level deformation fields that are desirable in high-resolution analysis. However, DENSE can be complicated by challenges associated with image phase unwrapping, in particular offset determination. On the other hand, Hyperelastic Warping can be hampered by low local image contrast. The current work proposes a novel approach for measuring tissue displacement with both DENSE and Hyperelastic Warping, incorporating physically accurate displacements obtained by the latter to improve phase characterization in DENSE. The validity of the proposed technique is demonstrated using numerical and physical phantoms, and *in vivo* small animal cardiac MRI.

¹© 2014 IEEE. Reprinted, with permission, from Arnold David Gomez, Samer A. Merchant, and Edward W. Hsu. Accurate High-Resolution Measurements of 3-D Tissue Dynamics with Registration-Enhanced Displacement Encoded MRI. *IEEE Transactions on Medical Imaging*. March, 2014.

4.2 Introduction

Tissue displacement measurements are useful to obtain kinematic information and deformation metrics, which are associated with functional and material properties often used as indicators of an organ's state of health. For example, 3D displacements are useful to characterize skeletal muscle kinematics [1], [2], or to approximate deformation of thin tissues by means of surfaces like in the right ventricle (RV) and blood vessel walls [3], [4]. Localized myocardial strain maps of the left ventricle (LV), often derived from displacement fields, have been shown to be more effective than global parameters like ejection fraction for detecting cardiac abnormalities [5], [6]. Similar approaches have also been used to investigate brain injury [7], [8].

Clinical and experimental characterization of internal tissue motion *in vivo* has been achieved predominantly by noninvasive medical imaging techniques like ultrasound, computed tomography (CT), and magnetic resonance imaging (MRI) [9]–[11]. Echographic techniques, like speckle tracking, and displacement measurements from Doppler velocity mapping offer the advantages of portability and real-time acquisition, which are often desired for dynamic imaging. However, limited volumetric resolution and issues arising from wave scattering due to density variations around the lungs or bones, make these techniques suboptimal for some applications [12]. Although CT provides high spatial resolution images that can be beneficial and desirable for image registration [13], the modality is yet to be commonly employed for displacement measurements due to its use of ionizing radiation and limited soft tissue contrast.

Because of its soft tissue sensitivity and robust contrast, MRI has become the main tool for the development of several techniques to measure displacement fields [14]. One

of the most accepted methods for measuring displacements using MRI consists of creating traceable patterns on the image in a procedure known as tagging [15], [16]. Using the generated grid pattern or its crossings on the magnitude image as fiducial markers, the technique is still considered by many as the gold standard for 2D deformation mapping [17], [18]. Automated tag-tracking in 2D and even in 3D has been made possible by advances in computer vision and acquisition strategies [1]. The resolution, although traditionally limited to tag spacing, can be improved by interpolation, pattern matching, or harmonic phase analysis (HARP) with extended k-space filters [19], [20].

Other phase-weighted MRI techniques have also been used to measure motion directly without the need for tracking. For example, phase contrast, originally used in MR angiography for velocity mapping [21], [22], has been adapted to approximate tissue motion by integrating a velocity field over time [23]. Alternatively, displacement encoding with stimulated echoes (DENSE) [24]–[26] provides direct displacement weighting. The advantages of DENSE over, for example, tagging, include pixel-level resolution, and the ability to encode motion in the through-plane direction as well as in-plane directions. These benefits have fueled the analysis of deformation predominantly in the heart. However, practical utility of DENSE has largely been limited by the lack of a generalized approach for relating phase image information to physical displacements, though some recent progress appears promising [27]. The key challenge is to avoid potential problems arising from the angular nature of phase images, like phase wrapping and displacement offsets, which ultimately determine the overall accuracy of the measurements [28], [29].

Besides image acquisition-based methods, displacement can also be obtained by registering anatomical images acquired as the deformation occurs. The approaches include calculating displacements purely from image information with texture correlation [30], [31], local intensity [32]–[36], or other similarity metrics [37], [38]. Registration-based methods are prone to lack of fidelity in areas of poor contrast and numerical ill conditioning. Therefore, image registration continues to be actively studied [39], [40], and has involved using local intensity registration along with fluid [34], or solid [41] deformation schemes to provide regularization and numerical stability. One notable example is Hyperelastic Warping [35], [36], which uses a solid mechanics formulation by means for finite element (FE) modeling. This technique has been shown effective experimentally for deformation characterization of ligaments, blood vessels, and the LV, with different imaging modalities [4], [42], [43]. However, though adding a continuum mechanics model to the registration process can greatly increase its effectiveness, it also introduces dependency on constitutive assumptions and geometric modeling, all of which influence the accuracy of the end result [43].

When investigating tissue displacements noninvasively, it is desirable to obtain accurate information, so that mechanical information from relative deformation metrics and global kinematics of motion can be obtained without the need for *a priori* assumptions. Likewise, pixel-level resolution is preferred for localizing potential functional deficiencies, or complex motion patterns, even in cases when tissue dynamics involve large deformations over a given amount of time. In response to these requirements, this paper presents a combined method for automatically reconstructing 3D displacements by using partial image registration information to accurately

determine offsets associated with phase unwrapping in DENSE-MRI. The method enables DENSE-MRI to measure highly accurate tissue dynamics between a reference and deformed states without the need for intermediate image acquisition. This report contains the theoretical background underlying the combined analysis, which is followed by verification with numerical images, experimental validation using a moving phantom and a demonstration of the presented concepts *in vivo*.

4.3 Theoretical Background

A brief summary of displacement characterization using DENSE-MRI and Hyperelastic Warping is provided to better explain their challenges and remedies. In the ensuing text, vectorial quantities are accented with an arrow, and matrices appear underscored.

4.3.1 DENSE-MRI Reconstruction

In DENSE [24]–[26], motion is encoded in the phase angle of the complex MRI signal. Each image contains information about a component of the tissue displacement vector field, $\vec{u}(\vec{r})$, in spatial coordinates (deformed configuration), \vec{r} , observed after a deformation has occurred. The motion encoding direction and sensitivity are determined by the combined sensitizing gradients, which are related to the first moment of encoding gradient pulses placed after the first and third RF pulses in the stimulated echo sequence [24]. By expressing the directional encoding sensitivity as a vector \vec{k}_e (in rad/mm or cycles/mm), N phase images, $\phi_i(\vec{r})$, can be obtained from a set of $(\vec{k}_e)_i$ as follows:

$$\phi_i(\vec{r}) = (\vec{k}_e)_i \cdot \vec{u}(\vec{r}), \quad i = 1, 2, \dots, N. \quad (4.1)$$

3D characterization of $\vec{u}(\vec{r})$ can be obtained from phase images encoded in orthogonal directions by, for example, letting $\underline{K} = [(\vec{k}_e)_1 \ \dots \ (\vec{k}_e)_i]^T$ and solving for the least squares problem given by [44]

$$\vec{u}(\vec{r}) = (\underline{K}^T \underline{K})^{-1} \underline{K}^T \phi_i(\vec{r}). \quad (4.2)$$

In practice, each phase image also contains a spatially dependent contribution, $\Delta\phi(\vec{r})$, due to instrumentation imperfections (e.g., magnetic field inhomogeneity) such that the phase image is more accurately represented as $\phi_i(\vec{r}) = (\vec{k}_e)_i \cdot \vec{u}(\vec{r}) + \Delta\phi(\vec{r})$. The influence of the background inhomogeneity term can be corrected by subtracting a phase image without displacement encoding, often called reference, from each of the encoded images prior to the application of (4.2). Thus, the measurement of a 3D vector field via DENSE requires a minimum of four images: three motion-encoded images (often in orthogonal directions), and a nonencoded reference image [26].

Because the phase quantity is periodic, phase wrapping occurs when the encoded phase exceeds its cyclic interval of 2π , say $[-\pi, \pi]$. Figure 4.1 shows examples of true and wrapped displacement profiles. Although part of the acquisition process involves empirically optimizing \vec{k}_e to maximize resolution while minimizing phase wrapping, the latter remains unavoidable in practice especially when high spatial resolution is desired [45]. Consequently, a major part of displacement measurement via DENSE is the postprocessing of phase wrapped images, which involves two critical steps: first, the phase is unwrapped to eliminate discontinuities in phase images, and second, the resulting continuous phase maps are matched to true displacements by correcting for the phase offsets at selected pixels (known as “seed,” “true phase,” or “reference” points).

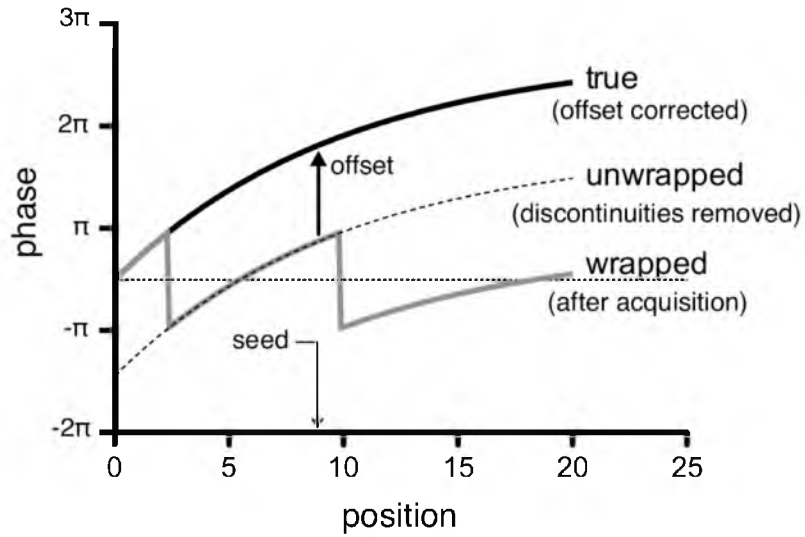


Figure 4.1: Effect of phase wrapping in displacement profiles. The measurement of the true motion (black) is initially affected by phase wrapping (gray). Phase unwrapping effectively removes the discontinuities in the displacement profile (dashed line), but an offset vector evaluated at a seed location is necessary to fully reconstruct the original displacements.

Although phase unwrapping has been well studied from its association with other fields like radar interferometry [46], [47] and geophysics [48], [49], matching the results to underlying displacements is more unique to DENSE reconstruction, which continues as an active area of research [29], [45], [50].

Given a contiguous tissue region in a slice, the contribution of a phase offset error, $(\phi_e)_i$, can be included by modifying (4.2) into,

$$\begin{aligned}\vec{u}_d(\vec{r}) &= (\underline{K}^T \underline{K})^{-1} \underline{K}^T \phi_i(\vec{r}) + (\underline{K}^T \underline{K})^{-1} \underline{K}^T (\phi_e)_i \\ &= \vec{u}(\vec{r}) + \vec{u}_{ref}\end{aligned}\tag{4.3}$$

which shows that uncorrected phase offsets would result in an unknown, but constant offset error vector \vec{u}_{ref} in the DENSE displacement field $\vec{u}_d(\vec{r})$. In the absence of any correction, errors in \vec{u}_{ref} can dominate the displacement solution and can affect estimates of motion, rotation about a given axis, and through-plane strain measurements in multislice acquisitions or strain tensor polynomial fitting [51], [52]. Therefore, it becomes necessary to approximate the reference vector, for instance, by visual inspection. Alternatively, *a priori* knowledge of the tissue motion can also be used. For example, because healthy left-ventricular (LV) motion in a 2D slice is mostly radially symmetric, it has been assumed that in-plane displacements should average to zero [26]. Offset vectors can also be estimated assuming small displacements in between frames [29], [45]. To date, means to objectively correct for arbitrarily fast or large displacements in between temporal frames remains lacking.

4.3.2 Image Registration and Hyperelastic Warping

A common strategy for nonrigid image registration consists of an optimization problem aimed at finding the deformation map, $\vec{\varphi}$, that minimizes a fidelity measure between two images: a template image, $T(\vec{x})$, and a target (or source) image $S(\vec{X})$ [32]–[35], [37]. (The upper and lower cases, \vec{X} and \vec{x} , are used here to identify coordinate systems before and after image registration, respectively.) Depending on their formulation and implementation, different registration processes may output the resulting deformation field as $\vec{\varphi}: \vec{X} \rightarrow \vec{x}$, its inverse $\vec{\varphi}^{-1}: \vec{X} \rightarrow \vec{x}$, or both. Because the proposed method involves pairing registration results with DENSE displacements, the resulting displacements must be expressed in spatial coordinates, \vec{r} , which can be obtained directly, by interpolation, or by switching the order of the input imagery depending on the registration algorithm.

In Hyperelastic Warping, $\vec{\varphi}(\vec{X}) = \vec{x}(\vec{X})$ is obtained via FE approximations [35], [36]. The resultant displacement field $\vec{U}_w(\vec{X}) = \vec{X} - \vec{x}(\vec{X})$ (or $\vec{u}_w(\vec{r})$ in spatial coordinates) corresponds to translations of the FE nodes. Magnitude image information is used to drive a mesh towards deformation by means of

$$\vec{b}(\vec{X}) \cdot \vec{\eta} = \lambda \left([T(\vec{X}) - S(\vec{\varphi})] \frac{\partial S(\vec{\varphi})}{\partial \vec{\varphi}} \cdot \vec{\eta} \right). \quad (4.4)$$

where \vec{b} is equivalent to a body force field in the general direction $\vec{\eta}$, and λ is a factor that scales the contribution of image-based forces that, according to the FE solution approach, will be balanced by stresses associated with material properties (e.g., stiffness or bulk moduli) by means of conservation of momentum as detailed in [35], [36], [43]. To capture large displacements, it is customary to apply blurring to the images in the

early stages of registration, and gradually reduced thereafter, which ensures local displacements are not impacted. The forcing term, (4), is equivalent to weighted pixel-wise intensity differences (i.e., the spatial gradient of the target image evaluated at stationary target points). While intensity differences provide a fidelity measure, the gradient component provides force scaling and directionality. In fact, the spatial gradient directs registration based on texture and edge information. Consequently, areas with no local intensity gradients do not contribute to registration forces [43].

To compensate for types of motion inherently difficult to capture using intensity images (e.g., rotation about an axis of symmetry), and for areas within an image far from object edges or without texture, Hyperelastic Warping can include physically realistic geometry, boundary conditions, and material constitutive information improve the accuracy of the results. Therefore, although Hyperelastic Warping has the advantage of capturing large displacements between frames, accuracy may be uniform, concentrated, or scattered, depending on additional compensatory information.

4.3.3 Proposed Registration Strategy

Two important observations can be made from the above discussion on DENSE and Hyperelastic Warping, that (a) each component of a given displacement can be measured from DENSE except it may contain a contribution from erroneously determined phase offset, and (b) in the absence of additional information, the confidence of the measured displacement via Hyperelastic Warping is highest in areas where image contrast is highest, since these locations have the large image-based forces as quantified via (4.4). As illustrated in Figure 4.2, these two observations lead to the

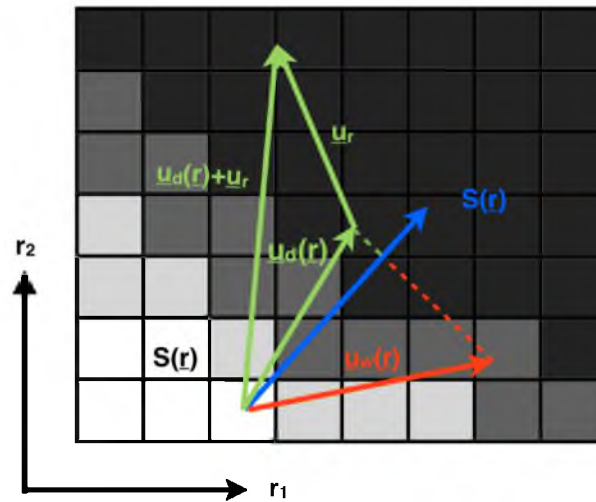


Figure 4.2: Schematic illustration of the proposed registration-enhanced DENSE reconstruction. The grid represents a zoomed view of the deformed image $S(\vec{r})$, which is defined in spatial coordinates, \vec{r} . Because intensity-based registration solutions, $\vec{u}_w(\vec{r})$, are more accurate in areas with greater local contrast, the gradient, $\nabla S(\vec{r})$, is used as a weight for the comparison to DENSE solutions, $\vec{u}_d(\vec{r})$. An offset \vec{u}_r is found so as to minimize the difference between components parallel to the gradient. In that way, the DENSE solution may retain displacements in directions that are not perceptible by the registration process.

unique criterion that correct solutions to DENSE and Hyperelastic Warping estimations of displacement should be identical along the direction of the image intensity gradient, which constitutes a measure of local contrast. In other words,

$$\vec{u}_d(\vec{r}) \cdot \nabla S(\vec{r}) = \vec{u}_w(\vec{r}) \cdot \nabla S(\vec{r}), \quad (4.5)$$

where $\nabla S(\vec{r}) = \frac{\partial S(\vec{r})}{\partial \vec{r}}$, is the intensity gradient of the image acquired after the deformation has occurred with respect to spatial coordinates. The basic premise of the current work is that image registration information, readily obtainable from images already included in the DENSE acquisition, can be used via (4.5) to regularize DENSE reconstruction such that accurate displacement fields can be obtained.

In practice, (4.5) can be implemented in DENSE reconstruction by inserting (3) and rearranging, which yields the solution for the offset error vector given by,

$$\nabla S(\vec{r}_j) \cdot \vec{u}_r = [\vec{u}_w(\vec{r}_j) \cdot \nabla S(\vec{r}_j) - \vec{u}_d(\vec{r}_j) \cdot \nabla S(\vec{r}_j)], \quad (4.6)$$

wherein every pixel in a slice, $j = 1, 2, \dots, M$, provides an equation in a linear system that can be solved using weighted least squares. If a 3D unwrapping algorithm is used [53], then (4.6) can be applied along a volume instead of a slice region, effectively reducing computation time. It should be noted that the offset error vector \vec{u}_r is defined in (4.3) for a contiguous region, and different contiguous areas (e.g., the heart and chest within a given MR image) may have different offset vectors. To solve this problem, and to better capture relative motion or other interactions, (4.6) can be applied to subregions of a volume by means of region-specific masks.

The above formulation of combined displacement field reconstruction should be flexible enough to allow (4.6) to be implemented with alternative registration techniques other than Hyperelastic Warping. Gradient-based forcing terms similar to (4) arise from

minimization of a generalized fidelity measure of image intensity energy, namely:

$$E(\vec{X}, \vec{\varphi}) = \frac{\lambda}{2} \left(T(\vec{X}) - S(\vec{\varphi}) \right)^2, \quad (4.7)$$

which assumes a Gaussian distribution for MRI intensity [54]. Actually, (4.4) becomes apparent from the first variation of (4.7) with respect to $\vec{\varphi}$. A similar minimization strategy is the basis of alternative registration formulations, including some forms of fluid and diffusion registration [32], [34], [55].

4.4 Methods

The validity, effectiveness, and practical feasibility of the proposed approach were assessed using a combination of numerical and experimental procedures. Testing was based on fast dynamics characterized by large deformations between temporal frames, which result in significant phase wrapping. The numerical procedures involved quantifying measurement errors across different simulated scenarios that might be impractical to reproduce experimentally. The experimental procedures aimed to confirm observations from simulated scenarios, and demonstrate the technique *in vivo*.

4.4.1 Numerical Verification

Two sets of computer simulations were performed: the first included different deformation scenarios, and the second consisted of a basic sensitivity analysis aimed at elucidating the effects of practical parameters on the accuracy of results.

4.4.1.1 Numerical Phantom and Image Generation

Volumetric images from a synthetic object (see top of Figure 4.3) were created using a $50 \times 50 \times 20$ matrix size. In order to capture a wide range of displacement

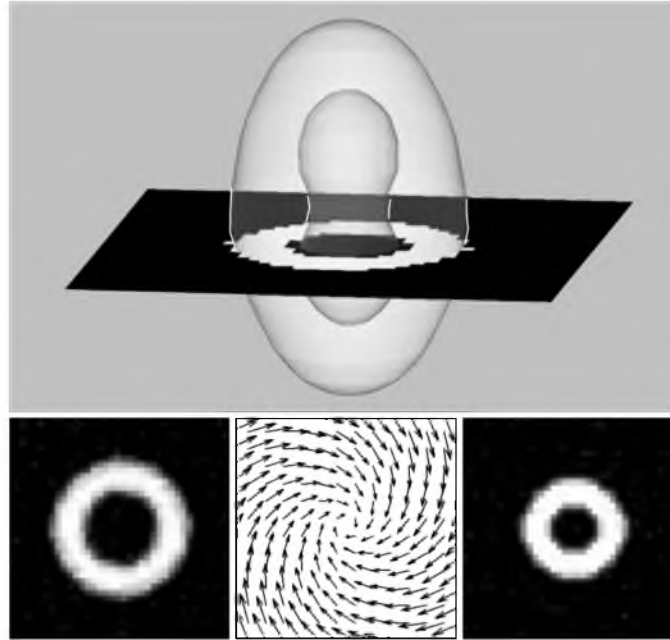


Figure 4.3: Numerical phantom and images used for verification. A thick-walled glyph (top) was used to generate testing images under various applied deformations. Examples of before (bottom left) and after (bottom right) images under the deformation (bottom center) described in scheme (c) of the text are shown.

magnitudes and directions, three deformation scenarios were used to warp the initial images, and generate simulated phase images. The deformations consisted of (a) simultaneous 20% stretch along the first in-plane axis (here referred as the x-axis) and 30% compression along the perpendicular in-plane direction (y-axis). These corresponded to a homogeneous deformation without through-plane components, (b) 10% compression along the z-axis, with a 10-pixel translation diagonal to x y and z, which was chosen to represent mostly rigid motion, and (c) contraction by 3 pixels in all directions with simultaneous 20° rotation about the z-axis. Depending on the location, displacements generated ranged from 0 to approximately 20 pixels in virtually all directions. To focus on the accuracy of deformation estimation without potential complication from noise, the images were generated with an SNR of 500.

Whereas the input images for registration consisted of the original and deformed states of the numerical phantom, complex DENSE images encoding the deformations information were simulated, with the corresponding displacements encoded in the wrapped phase angle given by:

$$\phi_i(\vec{r}) = \text{mod} \left(\frac{\pi}{u_i^{max}} \vec{u}_i(\vec{r}) - \pi, 2\pi \right) - \pi, \quad (4.8)$$

where mod stands for the modulo operator, and u_i^{max} indicates the maximum displacement before phase wrapping, set at 2 pixels in the in-plane directions, and 1 pixel in the out-of-plane direction. The maximum limit was chosen partly based on empirical observations, and partly to ensure nearly all images were affected by phase warping artifacts.

4.4.1.2 Displacement Field Reconstruction

To represent the measurements obtained by each of the approaches described in section 4.3.2, displacement fields were reconstructed using Hyperelastic Warping (subsequently referred to as *registration* solution), DENSE with offset correction for bulk motion of the imaged object (*bulk corrected* solution), and the proposed approach of combining DENSE and Hyperelastic Warping (*combined* solution).

3D registration was performed using a validated implementation of Hyperelastic Warping in NIKE3D software [56]. The registration code was embedded in a MATLAB (Mathworks, MA, USA) script, which automatically generated an FE model, determined image blurring, and optimized the registration parameter λ from (4) according to the following: The FE model consisted of hexahedral elements with nodes coinciding with pixel locations, assumed to behave as an isotropic Neo-Hookean solid [57] with coefficients $C_1 = 8$ kPa and bulk modulus of $\kappa = 0.1$ kPa. The initial size of the blurring mask was made to be a fixed 20% of the average number of pixels in each dimension. Because material coefficients were arbitrary, given that the maximum agreement between two images was obtained following convergence with the highest registration parameter, λ , the latter was optimized according to convergence so that maximum registration was achieved. The optimization began with a small value for λ (0.1), which was then increased if the registration process converges, or vice versa by means of bisection. To obtain a displacement field in the same coordinate frame as the DENSE results, all registration was done using the absolute reference configuration as the target, and subsequent images as the template.

For DENSE reconstruction, each image slice was first unwrapped as previously

described in [58]. To approximate the phase offset without using registration, a bulk motion displacement was defined as the translation of the synthetic object's centroid from before and after deformation. In contrast, for the proposed approach, essentially the same DENSE reconstruction was performed except registration information was used to correct for the phase offset via (4.6), which was evaluated at every slice.

4.4.1.3 Performance Assessment

With the displacements used to generate the input images as ground truth, the accuracy of the three solutions was evaluated based on percent absolute length and angular differences at each voxel (e.g., if a vector was 1.3 times the magnitude, and perpendicular to the true vector, then the errors would be 30% and 90° , respectively). Error values were averaged across the volume and reported along with their standard deviation. Finally, to provide insight on deformation calculations, the principal components of the Euler-Lagrange strain tensor were computed using a finite-difference deformation gradient approximation and eigenvalue decomposition [59].

4.4.1.4 Sensitivity Analysis

The experiments created as a sensitivity analysis included variations in noise levels, warping parameters, and compatibility of the proposed method with other registration approaches. These tests included: (a) signal-to-noise ratio (SNR) variations (500, 100, 50 and 15), (b) changes in registration parameters, with C_1 and bulk modulus decreased or increased by 50% ($0.5C_1$, $1.5C_1$, 0.5κ , and 1.5κ), and (c) replacing the registration algorithm with the automatic, nonrigid technique delineated in [55] instead of

Hyperelastic Warping. In each of these cases, the combined solution displacement fields were obtained for all deformation scenarios and compared to the ground truth as described above. The performance was averaged for the three deformation scenarios and reported.

4.4.2 Validation With Experimental Phantom

Based on previously documented DENSE-MRI studies such as [60], a precision apparatus was designed to move a phantom along a predictable path, which served as a benchmark displacement field. The motion of the phantom was designed to both induce phase wrapping since the initial time frame, and include displacement in a direction without local contrast. To achieve these goals, the rotational speed was set to produce motion beyond the wrapping interval, and the phantom was constructed with a substantial lack of internal contrast.

4.4.2.1 Motion Apparatus

A phantom consisting of a cylindrical container 16 mm in diameter filled with a water-based gel (1.0 mg/L CuSO_4 in 2.0% Agarose) was mounted to a case inside the MRI bore (Figure 4.4, top). The case was rotated by an externally positioned motor at a rate of 4 rev/s, which ensured phase wrapping of all images. An optical encoder was used to provide angular speed and position monitoring, as well as acquisition triggering. The phantom was eccentrically placed within the rotation apparatus, and slices were chosen so that the trajectory, a combination of bulk motion and rotation, could be described analytically as follows:

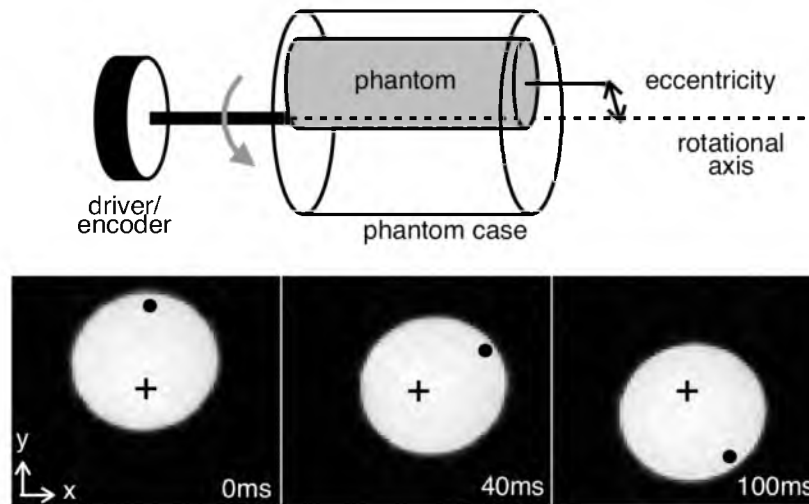


Figure 4.4: Schematic and MR images of the controlled motion apparatus. The schematic (top) shows the location of the phantom with respect to the rotation apparatus. The trajectory of the object can be obtained either from imaging data or from the encoder output, and an eccentricity measurement. To visualize the motion, the magnitude MR images (bottom) are overlaid with the approximate location of the axis of rotation (+), and a point near the edge of the phantom (•) as time progresses.

Given a rotation matrix \underline{Q} ,

$$\underline{Q}(\theta) = \begin{bmatrix} \cos \theta & \sin \theta \\ -\sin \theta & \cos \theta \end{bmatrix} \quad (4.9)$$

and the identity matrix \underline{I} , the displacement field can be defined as

$$\vec{u}(\vec{r}, \theta) = (\underline{I} - \underline{Q}(\theta)) \vec{r}, \quad (4.10)$$

where the angle of rotation, θ , is proportional to the phantom rotational velocity and multiples of the repetition time at each frame.

4.4.2.2 Imaging Parameters and Image Preparation

The moving phantom was imaged using a CINE DENSE pulse sequence [26] on a Bruker Biospec 7T scanner (Bruker Biospin, MA, USA), and a 72-mm ID quadrature volume coil. Other pertinent imaging specifications included 20.0 ms TR, 2.0 ms TE, 40 x 40 mm FOV, 96 x 96 matrix size, and 0.7 cycles/mm motion encoding gradients in each of the x and y directions. DENSE magnitude images (i.e., images after k-space subtraction and low pass filtering), obtained in all displacement encoding directions were averaged to compensate for stimulated echo signal loss, and then used as input to the registration algorithm

4.4.2.3 Displacement Field Analysis

Equation (4.9) served as the ground truth to which image-based motion measurements were compared. The error analysis and reconstruction approaches were identical to the numerical verification steps described above. Additionally, to assess displacement field quality in terms of pixel correspondence across time points, intensity differences between the images at time zero and material point evaluations of images at

later times (i.e., using deformation field to effectively move the image back to the original configuration) were also reported in maps and as root-mean-squared (RMS) difference measured in arbitrary units (a.u.). To calculate the center of rotation used for the benchmark displacement field, the best center points at each time frame (per RMS minimization) were averaged assuming that the center of rotation does not change in time. Differences in vector fields resulting from using the mean and the best center rotation for each time point were averaged to estimate this uncertainty.

4.4.3 *In Vivo* Experiment

Cardiac imaging was selected as the means for *in vivo* demonstration of the combined methodology to test whether general practical challenges (e.g., the usage of gradients or practical SNR) are fundamental impediments to its application, and if controlled experiment results are able to carry over to an *in vivo* setting. The resulting displacements were compared to manually tracked tags, systolic twist angles and circumferential strains were compared to previous studies [59], [61]. Each result compares a reference configuration, end diastole (ED), to subsequent time points. No intermediate data are used to obtain a given result.

4.4.3.1 Animal Protocol

All animal protocols were approved by the Institutional Animal Care and Use Committee at the University of Utah in accordance with the Guide for the Care and Use of Laboratory Animals issued by the US National Institutes of health (NIH Publication No. 85-23, rev. 1996). An adult male (350 g) Sprague Dawley rat was anesthetized with

1–3% isoflurane and 0.8 L/min O₂. For imaging, the animal was placed prone inside the RF coil. Vital signs (respiration, temperature, heart rate ECG, and oxygen saturation) were continuously monitored using a MR-compatible physiological monitoring system (SA Instruments, Stony Brook, NY, USA).

4.4.3.2 MRI Acquisition

The DENSE pulse sequence described in the previous section was applied in four cardiac short axis slices including the ventricles, ribs and surrounding tissue. Image acquisition was double-gated (to respiration and ECG) to start at beginning systole ($t = 0$) and continue with 20 ms frames (i.e., 50 frames/s) thereafter. To provide a qualitative comparison of the results, tagged MRI images [16] (with 2mm tag spacing) were also acquired in the same slice locations.

4.4.3.3 Displacement Reconstruction and Deformation Analysis

An average of the magnitude DENSE displacement-encoded images was registered using the simplified application of Hyperelastic Warping described above. Images at each cardiac time point were registered to the image at $t = 0$, so that results were not dependent on temporally adjacent images. Displacement fields within a segmented region of the LV myocardium were obtained using (4.9), unwrapped DENSE phase images, and the registration solution. For comparison, additional displacements at select locations around the LV were also obtained by manual tracking of tag intersections using customized interactive software. Lastly, to illustrate the utility of the displacement measurements, circumferential strain and midventricular longitudinal shortening,

(approximated by the average principal strain closest to the circumferential and through-plane directions, respectively), as well as slice twist, and left-ventricular torsion were also recorded for comparison with previously published values of a healthy rat [59], [61].

4.5 Results

4.5.1 Numerical Simulations

4.5.1.1 Reconstruction of Displacement Vector Fields

The displacement vector fields obtained for a representative image slice under test deformation scenario (c), where there existed a large variability in the performance among the different estimation schemes, is shown in Figure 4.5. Compared to the ground truth, it can be seen that the bulk motion-corrected technique conspicuously underestimated the through-plane displacements included in the deformation scenario (c). This is in agreement with the known limitation of the technique for the particular type of motion examined. Similarly, the registration-based method was largely unable to capture the prescribed rotational motion. In contrast, the proposed approach performed much better in characterizing the displacements under identical circumstances.

The performance of the different reconstruction schemes, in terms of quantified errors in the measured displacements, under different deformation scenarios are listed in Table 4.1. Consistent with the above observations, the proposed combined approach out-performed the registration and bulk motion-corrected schemes under all scenarios tested, resulting, in some instances, in magnitude error reductions of approximately

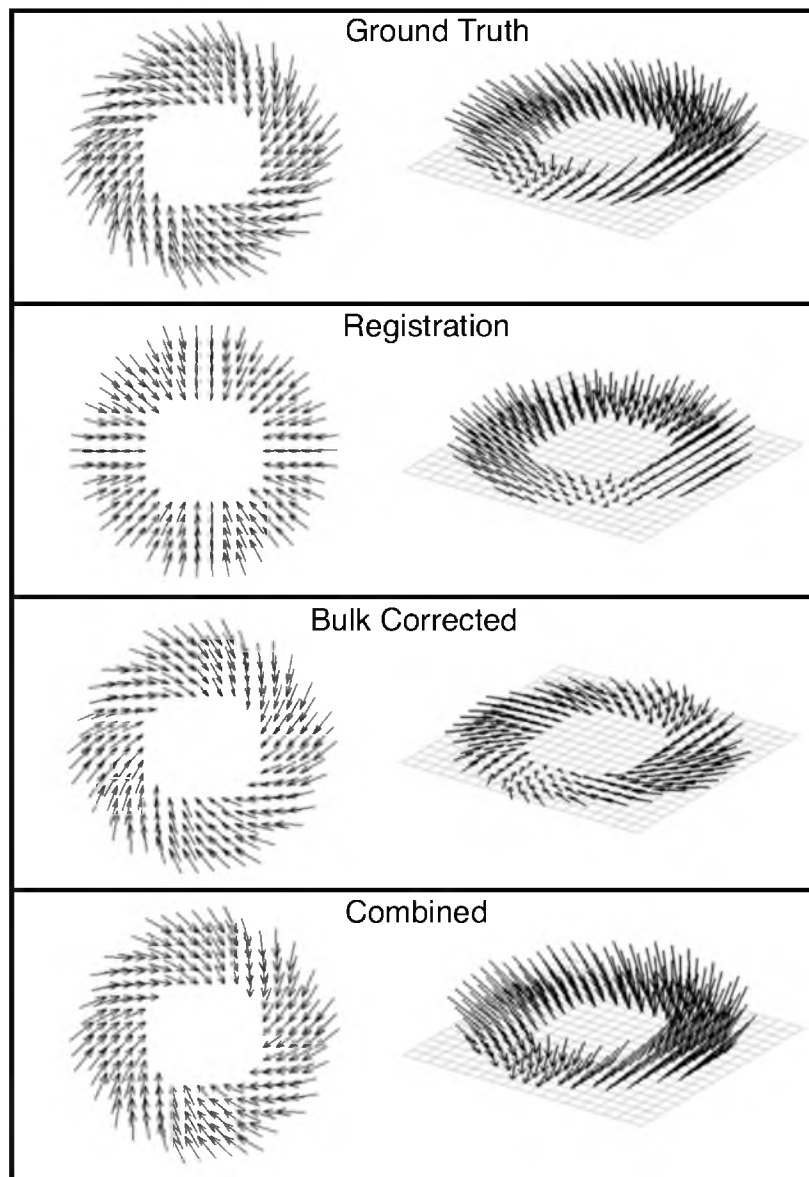


Figure 4.5: Displacement vector fields obtained by the different schemes for deformation scenario (c). The deformation consisted of rotation within the imaging plane as well as contraction in all axes. The vector fields estimated for a single as viewed from above (left column) and obliquely (right) to highlight the in-plane and through-plane components of the motion, respectively.

Table 4.1: Mean error in displacement estimations under different deformation conditions

	Scenario (a) Stretch (x) Compression (y)	Scenario (b) Rigid Motion Compression (z)	Scenario (c) Contraction and Rotation
<i>Registration</i>	$21 \pm 12\%$ $9.5 \pm 5.3^\circ$	$20 \pm 24\%$ $14 \pm 7.6^\circ$	$26 \pm 4.7\%$ $33 \pm 6.0^\circ$
<i>Bulk Correction</i>	$7.3 \pm 7.4\%$ $7.8 \pm 3.2^\circ$	$29 \pm 15\%$ $24 \pm 19^\circ$	$31 \pm 9.4\%$ $24 \pm 11^\circ$
<i>Combined Method</i>	$5.5 \pm 4.9\%$ $4.6 \pm 1.8^\circ$	$14 \pm 4.5\%$ $5.4 \pm 3.4^\circ$	$11 \pm 7.4\%$ $8.4 \pm 3.1^\circ$

Entries correspond to the mean and standard deviation of vectorial error in percent magnitude and angular differences from the ground truth.

75%, 50% and 66% (i.e., with respect to registration alone in case scenario (a), and bulk correction alone in scenarios (b) and (c)). On the other hand, the registration solutions performed rather poorly, likely because the simulation phantom lacked internal contrast and was thus biased against the scheme. Overall, the performance of all schemes was best when the deformation was limited to the imaging plane under scenario (a), and progressively deteriorated when through-plane and rotational motion were introduced in scenarios (b) and (c).

Simulated strain results in Figure 4.6 correspond to the same slice seen in Figure 4.5 where the principal strain components align with the circumferential, radial, and axial directions. The registration solution offers adequate agreement in principal directions and mean circumferential and through-plane strain, but there are discrepancies in radial strains likely due by concentration of registration forces near the borders, which result in overestimation of radial deformation. Because strains were calculated using relative motion, bulk correction results are unaffected by offset in the in-plane direction, but, because the average through-plane motion of the slice is different than the bulk motion of the volume, bulk correction fails to accurately approximate local through-plane strain. Similar observations were made in test scenario (b), but not in scenario (a) since through-plane deformation in that case was rigid (not shown). Finally, The combined method was able to better capture deformation and displacement in all directions.

4.5.1.2 Sensitivity Analysis

The performance of the presented approach with respect to variations in SNR is shown in Table 4.2, which contains errors averaged across all displacement scenarios

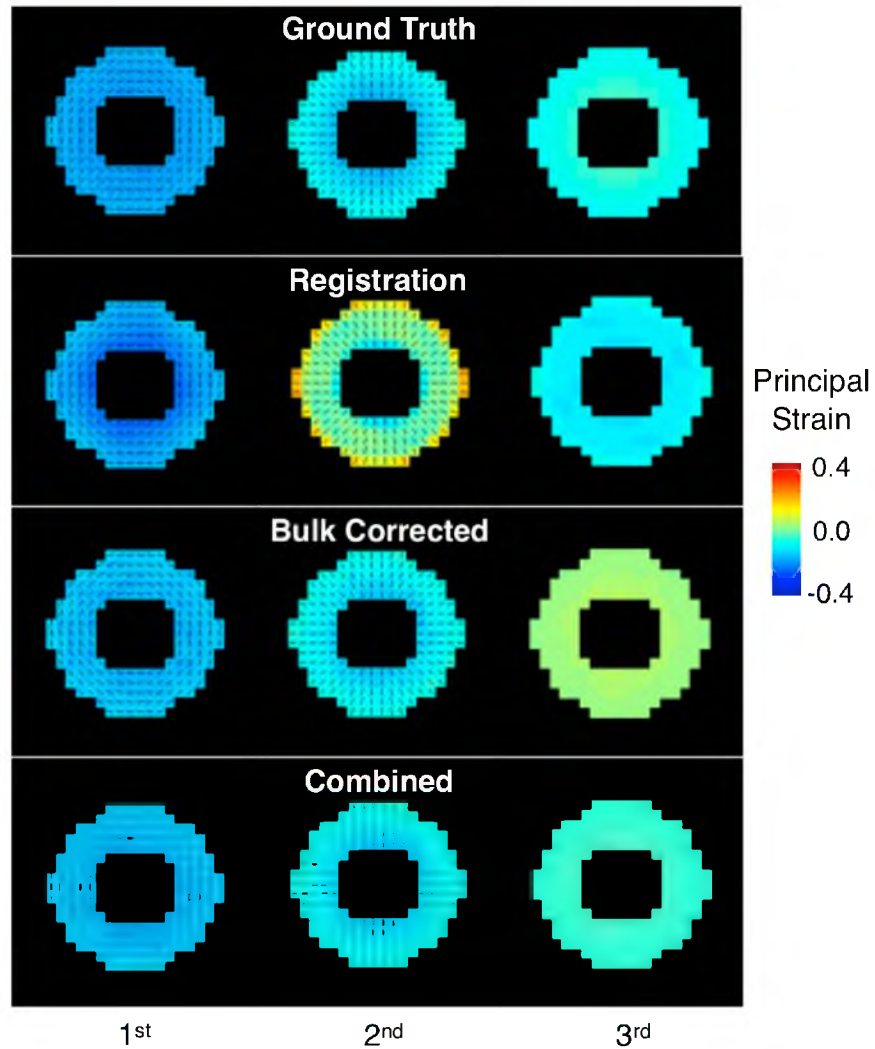


Figure 4.6: Strain maps obtained by the different schemes for deformation scenario (c). Circumferential, radial, and through plane (longitudinal) strains are, respectively, represented by the first, second, and third principal strains. Except for the through-plane direction, principal strain directions are shown in black lines.

Table 4.2: Performance of the proposed displacement measurement approach as a function of image SNR

SNR	500	200	50	15
Error	$10 \pm 4.7 \%$	$10 \pm 4.6 \%$	$10 \pm 4.6 \%$	$17 \pm 10 \%$
	$6.1 \pm 2.2^\circ$	$6.0 \pm 2.2^\circ$	$6.1 \pm 2.2^\circ$	$10 \pm 5.6^\circ$

Entries correspond to the mean and standard deviation of vectorial error in percent magnitude and angular differences from the ground truth.

investigated. Compared to the case of SNR of 500 (essentially noiseless), the method performed consistently and accurately within the range of practical SNR values (50-200) despite moderate noise. The consistency can be attributed to the use of smoothing in Hyperelastic Warping and the inherent robustness of phase imagery in DENSE. Not unexpectedly, the error of the method became noticeably increased at the lowest case, SNR=15.

The effects of variations in the material coefficients used in Hyperelastic Warping on the performance of the proposed combined method are shown in Table 4.3. The performance is shown to be relatively stable across the range (50% to 150%) of the stiffness parameter C_1 and bulk modulus κ investigated, with the exception that slightly elevated errors were observed when higher κ was used. The relative insensitivity to C_1 is indicative of the effectiveness of the penalty parameter λ optimization, which reduces the dependency on material assumptions. In contrast, the increased error associated with higher κ is likely due increased resistance to changes in volume.

Lastly, replacing Hyperelastic Warping with the fundamentally dissimilar nonrigid registration technique resulted in averaged percent magnitude and angular errors (across all deformation scenarios) of $6.1 \pm 9.4 \%$ and $5.7 \pm 7.0^\circ$, respectively, which are comparable to those for Hyperelastic Warping, $10 \pm 4.7 \%$ and $6.2 \pm 2.2^\circ$. The option to use an alternative registration method is attractive when Hyperelastic Warping is unavailable or for whatever reason not applicable.

Most computational time was used for the registration step, which given its iterative nature varied from 3 min to 1 h. Application of (4.6) increased computation time by a few seconds, which were needed to process the entire volume.

Table 4.3: Mean error with respect to true displacement field for all deformations with registration parameter variations

Parameter Change	0.5C ₁	1.5C ₁	0.5k	1.5k
<i>Error</i>	$10 \pm 5 \%$	$10 \pm 5 \%$	$10 \pm 6 \%$	$15 \pm 6 \%$
	$6.1 \pm 2.2^\circ$	$6.1 \pm 2.3^\circ$	$7.7 \pm 3.7^\circ$	$7.5 \pm 5.1^\circ$

Entries correspond to the mean and standard deviation of vectorial error in percent magnitude and angular differences from the ground truth.

4.5.2 Validation Using Experimental Phantom

Figure 4.7 contains representative images obtained for the rotating phantom, as well as corresponding displacement fields estimated by the different schemes. Based on error with respect to the ground truth averaged over all time points, the three displacement measurement approaches compare as follows: While image registration provided excellent match between the acquired and reverse-estimated images of the phantom at initial position and yielded a low average RMS of 0.2 ± 1.3 a.u. across time points, it was largely unable to describe the phantom's internal rotation resulting in high vectorial percent magnitude and angular errors of 56 ± 82 % and $57 \pm 46^\circ$, respectively. The DENSE field corrected by bulk displacement approximation revealed a conspicuous offset in the image difference, which translated to quantified errors of 1.6 ± 6.6 a.u., 23 ± 31 %, and $9.0 \pm 14^\circ$. By correctly estimating the offset, the proposed approach generated the most accurate displacement measurement, with the corresponding errors reduced to 0.6 ± 2.8 a.u., 7.2 ± 12 %, and $4.7 \pm 6.9^\circ$. The relatively poor performance of the registration method was expected, given the phantom's lack of internal texture, which can be compensated by tags [62], material properties [42], [43], or the inherent nature of DENSE, provided adequate correction of offset bias [63]. In reconstruction schemes involving DENSE (i.e., the bulk motion-corrected and proposed combined methods), the effects of image noise can be seen in the jagged border of the reverse-estimated initial-position image. However, the noise appeared not to have adversely impacted the displacement estimations.

It is worth noting that the benchmark displacement field resulted in a small but visible discrepancy in the difference image (Figure 4.7 top), which is due to the

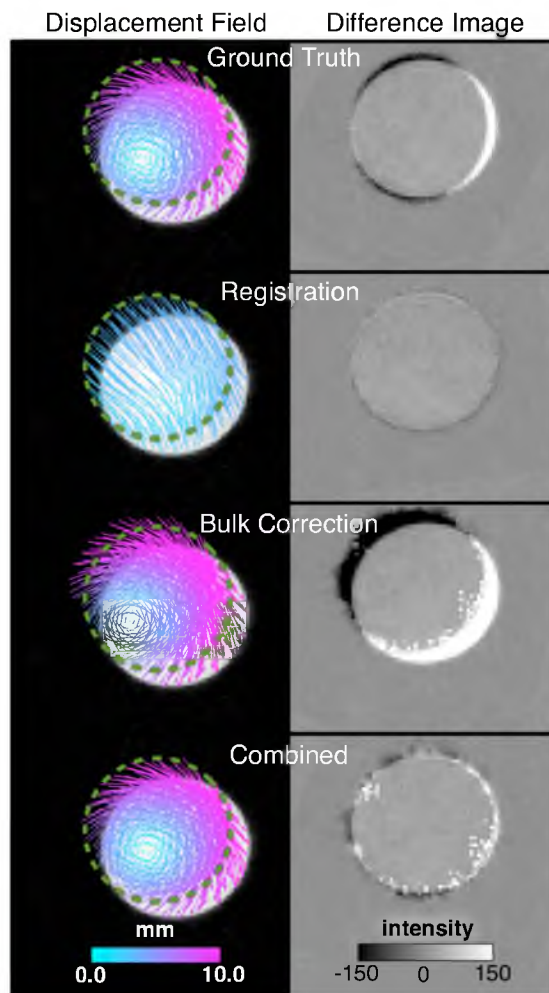


Figure 4.7: Experimental validation measurements on the rotating phantom. The left column shows prescribed (ground truth) and measured displacement vector fields superimposed on the axial image of the phantom at $t = 40$ ms according to the description in Figure 4.4. The green dashed line delineates the edge of the phantom at $t = 0$. The right column shows intensity difference images between actual and reverse-estimated initial location of the phantom.

unavoidable disparity between the prescribed and actuated motions. The errors associated with the disparity were 0.41 ± 1.56 a.u., 1.6 ± 2.2 % and $0.9 \pm 1.1^\circ$, which fall well below those of any scheme investigated and provides justification for the field obtained by (4.9) to be used as the ground truth.

4.5.3 *In Vivo* Demonstration

Figure 4.8 shows the displacements of the LV myocardium measured in a slice near the cardiac base as the rat's heart deformed from ED towards end systole (ES). In general, as observed with both tag tracking and registration-enhanced DENSE, the movement of the myocardium from ED to ES exhibited the familiar wall thickening and cavity reduction associated with LV contraction. The anterior part of the septum was relatively stationary, and most displacement occurred in the LV free wall. The above observation is consistent with visual inspection with respect to the anterior portion of the ribcage, which remains relatively stationary throughout the imaged time points likely due to the animal's prone orientation, as body weight presses the sternum against the bed. Additionally, qualitative interpretation of Figure 4.8, and comparing in-plane motion across different slices in Figure 4.9, shows good agreement between the displacement fields obtained by tag tracking and the proposed method. The computational time needed for registration and combined reconstruction of *in vivo* data averaged 30 min.

A rendering of the 3D LV motion at ES constructed from displacement fields obtained in multiple slices is shown in Figure 4.10. In contrast to the above noted variability of displacements within the imaging plane, the through-plane motion was

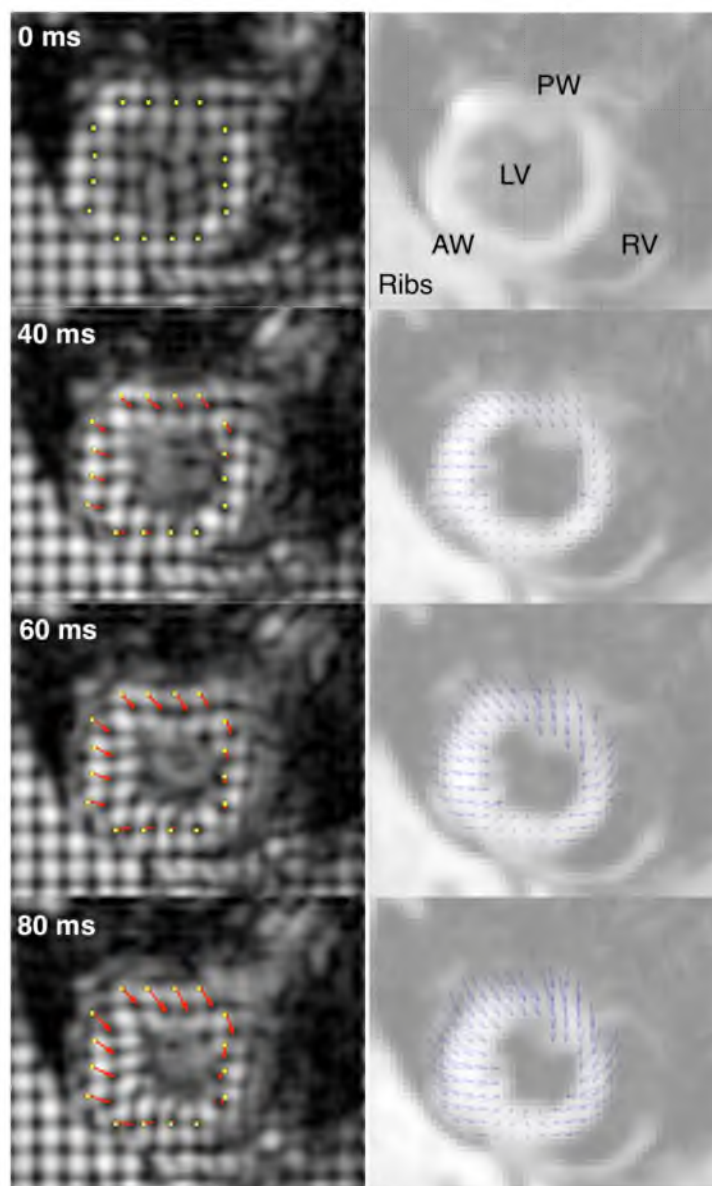


Figure 4.8: Tissue displacements by tagging and registration-enhanced DENSE. Sixteen reference points (yellow dots) placed around the LV myocardium on the tagged images (left column) were manually tracked to yield displacements (red arrows). DENSE vector plots (blue arrows) are overlaid on intensity-scaled magnitude images (right column). RV and LV indicate right and left ventricle, respectively. AW and PW stand for anterior and posterior walls. For clarity, only half the vectors in the registration-enhanced DENSE field are shown.

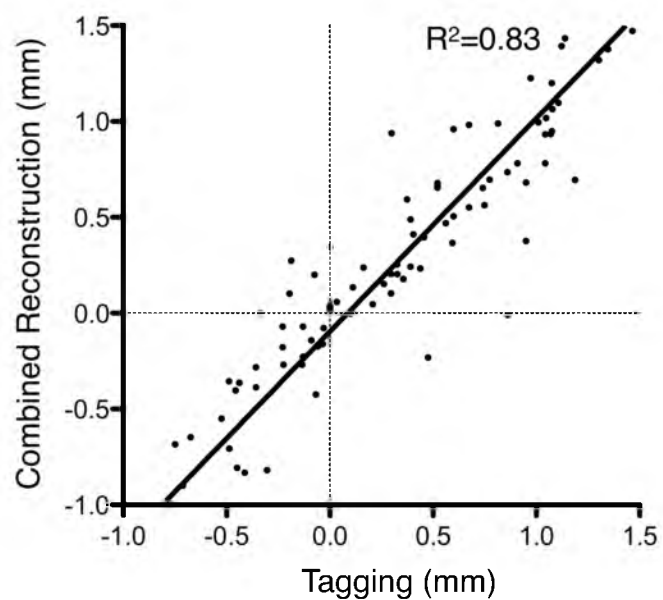


Figure 4.9: Direct comparison of displacements obtained by the proposed technique and tagging. Each point corresponds to a component-by-component comparison of in-plane displacements at the same locations at $t = 80$ ms. R^2 indicates coefficient of determination.

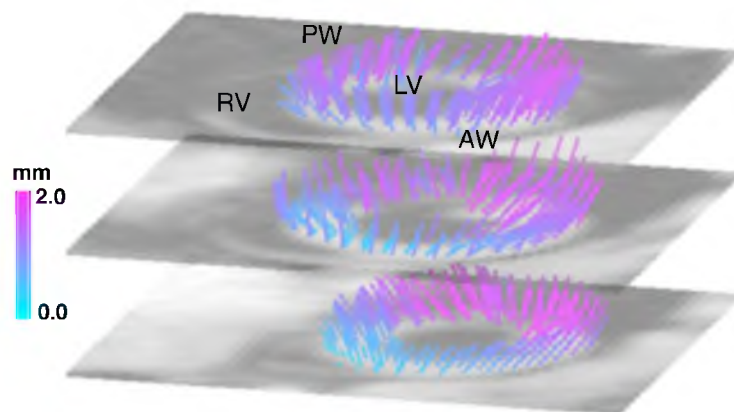


Figure 4.10: Multislice reconstruction of 3D left-ventricular motion. The color indicates the magnitude of the vectors. Despite of the through-plane motion, the total motion in the anterior wall (AW) near the septum separates the left and right ventricles, (LV and RV, respectively). The largest displacements occur in near the posterior wall (PW).

relatively uniform, in agreement with previous observations of animal cardiac motion [64], [65]. From the 3D displacement fields, the LV twist angles were measured to be $-3.0 \pm 3.0^\circ$ (mean \pm SD for the slice), $2.8 \pm 3.2^\circ$ and $8.9 \pm 3.8^\circ$ at the base, midventricle and apex, respectively. These values are similar to the $-5.6 \pm 1.9^\circ$ and $9.0 \pm 2.3^\circ$ reported previously for the base and apex, respectively [59].

Also based on the estimated displacement fields, the systolic LV circumferential strain was found to be -0.16 ± 0.08 (slice mean \pm SD), -0.19 ± 0.06 , and, -0.23 ± 0.04 at the base, midventricle, and the apex, respectively, which are in excellent agreement with values of -0.16 ± 0.02 , -0.19 ± 0.01 , and -0.21 ± 0.01 reported previously for the same measurements [59]. Midventricular shortening was measured at $-15 \pm 4\%$, which also compared very well with previously reported values of $-16 \pm 3\%$ [61]. Figure 4.11 shows the unsmoothed circumferential strain maps from displacement fields obtained using the proposed technique acquired shortly after ED and at ES. The reduction in strain magnitude from approximately zero (as some contraction took place during the mixing time in the DENSE pulse sequence) at ED towards the negative systolic strain was relatively uniform, indicating that the deformation was evenly distributed across the myocardium, including regions where absolute displacement was near zero.

4.6 Discussion

Overall, results of the numerical simulation, empirical phantom and live animal demonstration experiments shown in Figures. 4.5, 4.7, 4.8, and 4.9, and Tables 4.1-4.3, are strongly supportive of the basic premise of the current study, that image registration can be used to enhance the accuracy of DENSE displacement field mapping. As

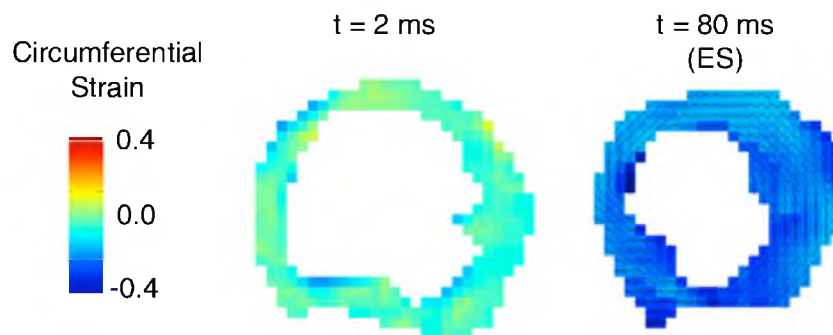


Figure 4.11: Circumferential strain maps in the rat LV myocardium. Compared to its value near end diastole ($t = 2$ ms), end-systolic (ES) strain indicates tissue shortening along the circumferential direction (black lines), which in contrast to the displacement field, occurs relatively uniformly across the entire myocardium despite a nonuniform displacement field (Figure 4.8).

explained in the Methods section, the accuracy of DENSE reconstruction critically depends on the ability to match unwrapped image phases to the underlying motion to eliminate cyclic phase offsets. The phase offsets are conventionally determined and corrected manually at only selected seed point locations using presumed displacement values. The excellent performance seen in the proposed approach can be attributed to the fact that via image registration it essentially employs all tissue borders (i.e., locations of high intensity gradient) as seed points and assigns them with actually measured displacements.

Besides the technical advantages, the proposed registration-enhanced DENSE reconstruction also offers some practical benefits. The approach uses images already in the dataset for its registration step, in as few as two time points, which reduces the need for intermediate acquisitions or other additional data. Moreover, because the reconstruction can estimate and correct the phase offsets with high degree of accuracy under a wide range of conditions, there is more flexibility in choosing the displacement encoding parameter (i.e., k_e) for the DENSE acquisition. Higher k_e values can be desirable for encoding small displacements or resolving small displacement differences without the concern that at the same time larger displacements would be undermined by phase offset determination. The enhanced sensitivity and expanded encoding range can be potentially significant in characterizing functional remodeling associated with diseases where tissue deformations can be both subtle and inhomogeneous.

The proposed displacement measurement scheme also facilitates postacquisition reconstruction. Although accurate DENSE displacement measurements are attainable in theory, subjectivity error may be introduced in instances where offset estimations

requires visual inspection. In contrast, the proposed scheme can accomplish the necessary phase offset correction largely free of user input or assumption of motion, and thus eliminate major sources of subjectivity and error in DENSE reconstruction. The present implementation of the reconstruction scheme requires only a small degree of user interaction, in defining contiguous regions of the tissue or organ in question. However, it is not inconceivable that the process can be made fully automated by incorporating more sophisticated image analysis methods, though such endeavor is outside the scope of the current investigation.

The current work is neither the first nor likely the last to improve the DENSE reconstruction accuracy via registration or other empirical means of motion estimation. In recent studies on cardiac mechanics [3], [29], [44], first-order approximations of velocity were used to estimate small deformations in intermediate DENSE scan time points. The deformation fields were then incorporated in the DENSE reconstruction to improve the accuracy tracking and phase offset determination [27]. Although a direct comparison may yield comparable performances, as noted above, the current direct registration-based reconstruction can be advantageous since it does not require (a) additional high temporal-resolution scans, or (b) the condition that the local deformations between frames to be small enough to be approximated by a first order velocity integration. Without these constraints, the proposed approach is better suited for characterizing deformation that involve relatively fast motion (or large displacement with respect to the scan intervals) or wide range of motions.

Needless to say, the proposed approach is not by any means perfect, especially in its dependence on image registration. Because of the complexity and heterogeneity of

deformations found in tissues, no image registration is truly accurate for all situations in reality. Though the presented implementation and (4.5) itself minimize the effects of the deformation model used and the lack of trackable local intensity contrast, the accuracy of image registration is still influenced by the pixelation of tissue borders, which is dependent on the spatial resolution of the images. In the present study, these factors are likely responsible for the small but nonzero displacement measurement errors incurred by the proposed technique under near-ideal (e.g., numerical simulation with high SNR) testing conditions. Additionally, related to the effect of image resolution, the ability of the proposed approach to track through-plane motion is dependent on the number and thickness of the image slices in the dataset. Due to experimental considerations, the slice thickness in an MRI scan is usually coarser than the in-plane resolution, resulting in poorer performance of the technique in characterizing through-plane motion. An extreme limiting case can be conceptualized by an inhomogeneous motion of a cylinder without local contrast in the z direction, which would result in the left hand side of (4.3) being zero and the inability to solve (4.4). In this case, compensatory information, like stiffness gradients, may be necessary to achieve an accurate result. Despite these practical limitations, it should be noted that the proposed scheme combining registration and DENSE reconstruction still resulted in accuracy improvement in the investigated scenarios. Through-plane motion characterization, or other organ-specific dynamics, can be optimized by careful study, design, and scan prescription to achieve a desired level of repeatability and reproducibility before testing a biological hypothesis.

Finally, although designed to correct for DENSE additive phase offsets for a demonstration within cardiac kinematics, the proposed methodology may be furthered

in several ways. As a start, instead of tuning Hyperelastic Warping towards automation (i.e., material parameter or geometry independence), as was done in the current study, it can be adjusted to include adequate geometrical, material, and load characterization [4], [42], [43], [66] to deliver a much more comprehensive mechanical analysis, like approximation of fiber shortening and stress. Such an approach may be susceptible to element inversion, which was avoided here by allowing volumetric deformation, but can also be addressed with suitable material characterization including fiber directionality and active contraction. Moreover, the regularization criterion stated in (4.5), plus a parameter-driven minimization of the image energy equation in (4.7), can be used to correct for other types of uncertainty besides DENSE phase offsets. For example, rather than using an additive model specified in (4.3), a multiplicative or combined (additive and multiplicative) model may be constructed to better model the effects of phase accumulation resulting from the individual contributions and interactions among displacement-encoding and other imaging gradient pulses, such as slice refocusing, or spoiler pulses. Similar strategies involving the comparison of results via (4.5) can be used for phase unwrapping, scaling, and confidence analysis. For example by using information from registration for constraining the unwrapping problem, or vice versa. Beyond DENSE, registration-based phase correction can be extended to other types of MRI like velocity imaging [23] where the phase contrast needs to be accurately related to the underlying motion. In terms of applications, the present approach can be employed to improve the utility of DENSE or other MRI characterization of motion where the measurement is technologically limited, like in the study of impact mechanics [8], and large deformation characterization [1], [23]. All of

the above can be worthy directions of future work.

4.7 Conclusion

Tissue deformation imaging via DENSE offers the benefit of pixel-level measurements, but has been hampered in practice by the necessary phase unwrapping, and more importantly, phase offset determination. The current study introduced a method for reconstructing DENSE displacement field by making use of image registration information as an alternative for *a priori* assumptions, visual inspection, or separate scans to estimate motion to compensate for the phase offset uncertainty. Numerical and empirical phantom testing and demonstration on a live animal showed the approach to be highly accurate, automated, robust and compatible with 3D displacement fields. These findings are very promising for incorporating the proposed registration enhancement to improve the practical utility of DENSE.

4.8 Acknowledgements

The authors would like to thank the Musculoskeletal Research Laboratories, and the Scientific Computation and Imaging Institute at the University of Utah for their support and resources, Osama Abdullah and Steve Maas for their technical assistance, and Dr. David Bull with the Department of Surgery (University of Utah) for additional resources.

4.9 References

- [1] K. M. Moerman, A. J. Nederveen, S. L. Evans, and S. C. K, “Inverse analysis of skeletal muscle tissue based on mri-derived 3d geometry, deformation, and fibre architecture,” in *Proceedings of the 11th International Symposium, Computer Methods in Biomechanics and Biomedical Engineering*, 2013, pp. 74–5.
- [2] X. Zhong, F. H. Epstein, B. S. Spottiswoode, P. A. Helm, and S. S. Blemker, “Imaging two-dimensional displacements and strains in skeletal muscle during joint motion by cine DENSE MR,” *J. Biomech.*, vol. 41, no. 3, pp. 532–40, Jan. 2008.
- [3] D. A. Auger, X. Zhong, F. H. Epstein, and B. S. Spottiswoode, “Mapping right ventricular myocardial mechanics using 3D cine DENSE cardiovascular magnetic resonance,” *J. Cardiovasc. Magn. Reson.*, vol. 14, no. 1, p. 4, Jan. 2012.
- [4] A. I. Veress, J. A. Weiss, G. T. Gullberg, D. G. Vince, and R. D. Rabbitt, “Strain measurement in coronary arteries using intravascular ultrasound and deformable images,” *J. Biomech. Eng.*, vol. 124, pp. 734–41, Dec. 2002.
- [5] T. P. Abraham and R. A. Nishimura, “Myocardial strain: can we finally measure contractility?” *J. Am. Coll. Cardiol.*, vol. 37, no. 3, pp. 731–4, Mar. 2001.
- [6] E. Kraigher-Krainer, A. M. Shah, D. K. Gupta, A. Santos, B. Claggett, B. Pieske, M. R. Zile, A. E. Voors, M. P. Lefkowitz, M. Packer, J. J. V McMurray, and S. D. Solomon, “Impaired systolic function by strain imaging in heart failure with preserved ejection fraction,” *J. Am. Coll. Cardiol.*, Oct. 2013.
- [7] P. V Bayly, E. H. Clayton, and G. M. Genin, “Quantitative imaging methods for the development and validation of brain biomechanics models,” *Annu. Rev. Biomed. Eng.*, vol. 14, pp. 369–96, Jan. 2012.
- [8] Y. Feng, T. M. Abney, R. J. Okamoto, R. B. Pless, G. M. Genin, and P. V Bayly, “Relative brain displacement and deformation during constrained mild frontal head impact,” *J. R. Soc. Interface*, vol. 7, pp. 1677–88, Dec. 2010.
- [9] M. V Burri, D. Gupta, R. E. Kerber, and R. M. Weiss, “Review of novel clinical applications of advanced, real-time, 3-dimensional echocardiography,” *Transl. Res.*, vol. 159, no. 3, pp. 149–64, Mar. 2012.
- [10] M. Tee, J. A. Noble, and D. A. Bluemke, “Imaging techniques for cardiac strain and deformation: comparison of echocardiography, cardiac magnetic resonance and cardiac computed tomography,” *Expert Rev. Cardiovasc. Ther.*, vol. 11, no. 2, pp. 221–31, Feb. 2013.
- [11] E.-S. H. Ibrahim, “Myocardial tagging by cardiovascular magnetic resonance:

- evolution of techniques-pulse sequences, analysis algorithms, and applications,” *J. Cardiovasc. Magn. Reson.*, vol. 13, no. 1, p. 36, Jan. 2011.
- [12] M. K. Feldman, S. Katyal, and M. S. Blackwood, “US Artifacts,” *Radiographics*, vol. 29, no. 4, pp. 1179–1189, 2009.
- [13] V. Tavakoli and N. Sahba, “Cardiac motion and strain detection using 4D CT images: comparison with tagged MRI, and echocardiography,” *Int. J. Cardiovasc. Imaging*, Oct. 2013.
- [14] A. A. Young and J. L. Prince, “Cardiovascular magnetic resonance: deeper insights through bioengineering,” *Annu. Rev. Biomed. Eng.*, vol. 15, pp. 433–61, Jan. 2013.
- [15] E. A. Zerhouni, D. M. Parish, W. J. Rogers, A. Yang, and E. P. Shapiro, “Human heart: tagging with MR imaging—a method for noninvasive assessment of myocardial motion,” *Radiology*, vol. 169, no. 2, pp. 59–63, 1988.
- [16] L. Axel and L. Dougherty, “Heart wall motion: improved method for spatial modulation of magnetization for MR imaging,” *Radiology*, vol. 172, no. 2, pp. 349–350, 1989.
- [17] B. D. Hoit, “Strain and strain rate echocardiography and coronary artery disease,” *Circ. Cardiovasc. Imaging*, vol. 4, no. 2, pp. 179–90, Mar. 2011.
- [18] Z. Qian, W.-N. Lee, E. E. Konofagou, D. N. Metaxas, and L. Axel, “Ultrasound myocardial elastography and registered 3D tagged MRI: quantitative strain comparison,” *Med. Image Comput. Comput. Assist. Interv.*, vol. 10, no. Pt 1, pp. 800–8, Jan. 2007.
- [19] N. F. Osman, E. R. McVeigh, and J. L. Prince, “Imaging heart motion using harmonic phase MRI,” *IEEE Trans. Med. Imaging*, vol. 19, no. 3, pp. 186–202, Mar. 2000.
- [20] N. F. Osman, W. S. Kerwin, E. R. McVeigh, and J. L. Prince, “Cardiac motion tracking using CINE harmonic phase (HARP) magnetic resonance imaging,” *Magn. Reson. Med.*, vol. 42, no. 6, pp. 1048–60, Dec. 1999.
- [21] N. J. Pelc, M. A. Bernstein, A. Shimakawa, and G. H. Glover, “Encoding strategies for three-direction phase-contrast MR imaging of flow,” *J. Magn. Reson. Imaging*, vol. 1, no. 4, pp. 405–13.
- [22] N. J. Pelc, R. J. Herfkens, A. Shimakawa, and D. R. Enzmann, “Phase contrast cine magnetic resonance imaging,” *Magn. Reson. Q.*, vol. 7, no. 4, pp. 229–54, Oct. 1991.

- [23] H. Zhou and J. E. Novotny, "Cine phase contrast MRI to measure continuum Lagrangian finite strain fields in contracting skeletal muscle," *J. Magn. Reson. Imaging*, vol. 25, no. 1, pp. 175–84, Jan. 2007.
- [24] A. H. Aletras, S. Ding, R. S. Balaban, and H. Wen, "DENSE: displacement encoding with stimulated echoes in cardiac functional MRI," *J. Magn. Reson.*, vol. 137, no. 1, pp. 247–52, Mar. 1999.
- [25] A. H. Aletras, R. S. Balaban, and H. Wen, "High-resolution strain analysis of the human heart with fast-DENSE," *J. Magn. Reson.*, vol. 140, no. 1, pp. 41–57, Sep. 1999.
- [26] D. Kim, W. D. Gilson, C. M. Kramer, and F. H. Epstein, "Myocardial tissue tracking with two-dimensional cine imaging : development and initial evaluation," *Radiology*, 2004.
- [27] A. D. Gilliam and F. H. Epstein, "Automated motion estimation for 2-D cine DENSE MRI," *IEEE Trans. Med. Imaging*, vol. 31, no. 9, pp. 1669–81, Sep. 2012.
- [28] A. A. Young, B. Li, R. S. Kirton, and B. R. Cowan, "Generalized spatiotemporal myocardial strain analysis for DENSE and SPAMM imaging," *Magn. Reson. Med.*, vol. 67, no. 6, pp. 1590–9, Jun. 2012.
- [29] A. D. Gilliam, X. Zhong, K. C. Bilchick, and F. H. Epstein, "Automated cardiac strain estimation from 2D cine DENSE MRI," *Proc. Intl. Soc. Mag. Reson. Med.*, vol. 19, no. 2011, p. 733, 2011.
- [30] G. Vendroux and W. G. Knauss, "Submicron deformation field measurements: part 2. Improved digital image correlation," *Exp. Mech.*, vol. 38, no. 2, pp. 86–92, Jun. 1998.
- [31] C. L. Gilchrist, J. Q. Xia, L. A. Setton, and E. W. Hsu, "High-resolution determination of soft tissue texture correlation," *IEEE Trans. Med. Imaging*, vol. 23, no. 5, pp. 546–553, 2004.
- [32] J. P. Thirion, "Image matching as a diffusion process: an analogy with Maxwell's demons," *Med. Image Anal.*, vol. 2, no. 3, pp. 243–260, 1998.
- [33] T. Vercauteren, X. Pennec, A. Perchant, and N. Ayache, "Symmetric log-domain diffeomorphic registration: a demons-based approach," in *International Conference on Medical Image Computing and Computer-Assisted Intervention*, 2008, vol. 11, no. Pt 1, pp. 754–61.
- [34] G. E. Christensen, R. D. Rabbitt, and M. I. Miller, "Deformable templates using large deformation kinematics," *IEEE Trans. image Process.*, vol. 5, no. 10, pp.

1435–47, Jan. 1996.

- [35] R. D. Rabbitt, J. A. Weiss, G. E. Christensen, and M. I. Miller, “Mapping of hyperelastic deformable templates using the finite element method,” in *SPIE 2573, Vision Geometry IV*, 1995, vol. 2573, pp. 252–265.
- [36] J. Weiss, A. Veress, and G. Gullberg, “Strain measurement using deformable image registration,” in *Mechanics of Biological Materials*, 2006, pp. 489–501.
- [37] F. Maes, a Collignon, D. Vandermeulen, G. Marchal, and P. Suetens, “Multimodality image registration by maximization of mutual information,” *IEEE Trans. Med. Imaging*, vol. 16, no. 2, pp. 187–98, Apr. 1997.
- [38] P. Cachier, E. Bardinet, D. Dormont, X. Pennec, and N. Ayache, “Iconic feature based nonrigid registration: the PASHA algorithm,” *Comput. Vis. Image Underst.*, vol. 89, pp. 272–298, Feb. 2003.
- [39] C. W. Hsia and M. H. Tawhai, “What can imaging tell us about physiology? Lung growth and regional mechanical strain,” *J. Appl. Physiol.*, vol. 113, no. 6, pp. 937–46, Sep. 2012.
- [40] B. Glocker, A. Sotiras, N. Komodakis, and N. Paragios, “Deformable medical image registration: setting the state of the art with discrete methods,” *Annu. Rev. Biomed. Eng.*, vol. 13, pp. 219–44, Aug. 2011.
- [41] J. A. Schnabel, C. Tanner, A. D. Castellano-Smith, A. Degenhard, M. O. Leach, D. R. Hose, D. L. G. Hill, and D. J. Hawkes, “Validation of nonrigid image registration using finite-element methods: application to breast MR images,” *IEEE Trans. Med. Imaging*, vol. 22, no. 2, pp. 238–47, Feb. 2003.
- [42] N. Phatak, Q. Sun, S.-E. Kim, D. Parker, K. Sanders, A. Veress, B. Ellis, and J. A. Weiss, “Noninvasive determination of ligament strain with deformable image registration,” *Ann. Biomed. Eng.*, vol. 35, no. 7, pp. 1175–87, Jul. 2007.
- [43] N. S. Phatak, S. a Maas, A. I. Veress, N. a Pack, E. V. R. Di Bella, and J. a Weiss, “Strain measurement in the left ventricle during systole with deformable image registration,” *Med. Image Anal.*, vol. 13, no. 2, pp. 354–61, Apr. 2009.
- [44] X. Zhong, P. A. Helm, and F. H. Epstein, “Balanced multipoint displacement encoding for DENSE MRI,” *Magn. Reson. Med.*, vol. 61, no. 4, pp. 981–8, Apr. 2009.
- [45] B. S. Spottiswoode, X. Zhong, A. T. Hess, C. M. Kramer, E. M. Meintjes, B. M. Mayosi, and F. H. Epstein, “Tracking myocardial motion from cine DENSE images using spatiotemporal phase unwrapping and temporal fitting,” *IEEE Trans. Med. Imaging*, vol. 26, no. 1, pp. 15–30, Jan. 2007.

- [46] R. M. Goldstein, H. A. Zebker, and C. L. Werner, "Satellite radar interferometry: two-dimensional phase unwrapping," *Radio Sci.*, vol. 23, no. 4, pp. 713–720, Jul. 1988.
- [47] R. Gens, "Two-dimensional phase unwrapping for radar interferometry: developments and new challenges," *Int. J. Remote Sens.*, vol. 24, no. 4, pp. 703–710, Jan. 2003.
- [48] A. P. Shatilo, "Seismic phase unwrapping: methods, results, problems," *Geophys. Prospect.*, vol. 40, no. 2, pp. 211–225, Feb. 1992.
- [49] U. Spagnolini, "2-D phase unwrapping and phase aliasing," *Geophysics*, vol. 58, no. 9, pp. 1324–1334, Sep. 1993.
- [50] T. Lan and D. Erdogmus, "Phase unwrapping and background correction in MRI," in *Machine Learning for Signal Processing*, 2008, pp. 239–243.
- [51] I. K. Rüssel, M. J. W. Götte, J. G. Bronzwaer, P. Knaapen, W. J. Paulus, and A. C. van Rossum, "Left ventricular torsion: an expanding role in the analysis of myocardial dysfunction," *JACC Cardiovasc. Imaging*, vol. 2, no. 5, pp. 648–55, May 2009.
- [52] K. Kindberg, H. Haraldsson, A. Sigfridsson, J. Engvall, N. B. Ingels, T. Ebbers, and M. Karlsson, "Myocardial strains from 3D displacement encoded magnetic resonance imaging," *BMC Med. Imaging*, vol. 12, no. 9, Jan. 2012.
- [53] W. Liu, X. Tang, Y. Ma, and J.-H. Gao, "3D phase unwrapping using global expected phase as a reference: application to MRI global shimming," *Magn. Reson. Med.*, vol. 70, no. 1, pp. 160–8, Jul. 2013.
- [54] E. R. McVeigh, R. M. Henkelman, and M. J. Bronskill, "Noise and filtration in magnetic resonance imaging," *Med. Phys.*, vol. 12, no. 5, pp. 586–91, 1985.
- [55] D.-J. Kroon and C. H. Slump, "MRI modality transformation in demon registration," in *2009 IEEE International Symposium on Biomedical Imaging: From Nano to Macro*, 2009, pp. 963–966.
- [56] B. N. Maker, R. M. Ferencz, and J. O. Hallquist, "NIKE3D: A non-linear, implicit, three-dimensional finite element code for solid and structural mechanics," Lawrence Livermore National Laboratory, Report UCRL-MA, Oct. 1991.
- [57] R. W. Ogden, "Large deformation isotropic elasticity – on the correlation of theory and experiment for incompressible rubberlike solids," *Proc. R. Soc. A Math. Phys. Eng. Sci.*, vol. 326, pp. 565–584, Feb. 1972.

- [58] M. Costantini, "A novel phase unwrapping method based on network programming," *IEEE Trans. Geosci. Remote Sens.*, vol. 36, no. 3, pp. 813–821, 1998.
- [59] W. Liu, M. W. Ashford, J. Chen, M. P. Watkins, T. A. Williams, S. A. Wickline, and X. Yu, "MR tagging demonstrates quantitative differences in regional ventricular wall motion in mice, rats, and men," *Am. J. Physiol. Heart Circ. Physiol.*, vol. 291, no. 5, pp. H2515–21, Nov. 2006.
- [60] B. S. Spottiswoode, X. Zhong, C. H. Lorenz, B. M. Mayosi, E. M. Meintjes, and F. H. Epstein, "3D myocardial tissue tracking with slice followed cine DENSE MRI," *J. Magn. Reson. Imaging*, vol. 27, no. 5, pp. 1019–27, May 2008.
- [61] N. Bachner-Hinenzon, O. Ertracht, M. Leitman, Z. Vered, S. Shimoni, R. Beeri, O. Binah, and D. Adam, "Layer-specific strain analysis by speckle tracking echocardiography reveals differences in left ventricular function between rats and humans," *Am J Physiol Hear. Circ Physiol*, vol. 299, no. 3, pp. 664–672, 2010.
- [62] S. Y. Chun, T. G. Reese, J. Ouyang, B. Guerin, C. Catana, X. Zhu, N. M. Alpert, and G. El Fakhri, "MRI-based nonrigid motion correction in simultaneous PET/MRI," *J. Nucl. Med.*, vol. 53, no. 8, pp. 1284–91, Aug. 2012.
- [63] D. D. Chan and C. P. Neu, "Transient and microscale deformations and strains measured under exogenous loading by noninvasive magnetic resonance," *PLoS One*, vol. 7, no. 3, p. e33463, Jan. 2012.
- [64] Y. Liu, H. Wen, R. C. Gorman, J. J. Pilla, J. H. Gorman, G. Buckberg, S. D. Teague, and G. S. Kassab, "Reconstruction of myocardial tissue motion and strain fields from displacement-encoded MR imaging," *Am. J. Physiol. Heart Circ. Physiol.*, vol. 297, no. 3, pp. H1151–62, Sep. 2009.
- [65] W. D. Gilson, Z. Yang, B. A. French, and E. F. H, "Measurement of myocardial mechanics in mice before and after infarction using multislice displacement-encoded MRI with 3D motion encoding," *Am J Physiol Hear. Circ Physiol*, vol. 288, pp. H1491–H1497, 2005.
- [66] A. I. Veress, G. T. Gullberg, and J. A. Weiss, "Measurement of strain in the left ventricle during diastole with cine-MRI and deformable image registration," *J. Biomech. Eng.*, vol. 127, no. 7, pp. 1195–1207, Jul. 2005.

CHAPTER 5

PREDICTION OF MYOCARDIAL STRUCTURAL ALTERATION ACROSS THE CARDIAC CYCLE USING COMPUTATIONAL MECHANICS¹

5.1 Abstract

Myocardial microstructures are responsible for key aspects of mechanical cardiac function. Natural myocardial deformation across the cardiac cycle induces measurable structural alteration, which varies disease. Yet, comprehensive structural information needed to study variability through atlases, in 3D and time, is virtually unachievable with current noninvasive imaging technology. Therefore, the use of finite-element analysis to deform an initial DT-MRI dataset was investigated in terms of material symmetry, structural input and warping approach. Simulations and transformed data were, respectively, compared against *in vivo* MRI displacement measurements, and DT-MRI of an isolated heart preparation. Overall, transverse isotropic models with subject-specific fiber structure input provided reasonable approximation of kinematics, and structural alterations. Isotropic models yielded the poorest performance, and orthotropic models were more accurate but more computationally expensive.

¹Included with permission by Arnold D. Gomez, David A. Bull, and Edward W. Hsu from a manuscript in preparation entitled: Extrapolation of Myocardial Structural Alteration Across the Cardiac Cycle Using Computational Mechanics.

5.2 Introduction

There is a profound link between ventricular structure and mechanical cardiac function, which has been consistently observed experimentally and clinically. The structural aspects of myocyte aggregation give rise to wall thickening (the basis of stroke volume), circumferential strain, torsion, and other kinematics that serve as functional indicators [1]–[5]. There is evidence that structural information indicates fiber disarray. Thus, fiber orientation has been proposed as a measure to detect interstitial tissue fibrosis, to quantify the extent and progression of tissue damage due to ventricular infarction, and to assess changes after surgical restoration [6]–[9]. Disease has also been shown to alter normal structural dynamics, i.e., the natural structural alteration of the heart with the cardiac cycle [10]–[14]. From a computational standpoint, fundamental aspects of myocardial structure have been integrated with computational biomechanics to derive significant observations regarding stress distribution and contractility, as well as the optimization of devices and surgical techniques [4], [7], [15]–[17].

Ventricular myocyte aggregation, the basic component of myocardial structures, has been observed to exhibit a distinctive helical alignment of myocytes known as fiber structure, as well as a secondary sheet-like arrangement conceptualized from the observation of cleavage planes [18]–[22]. Historically, ventricular structure has been elucidated by different means including, among others, histology, electron microscopy and diffusion tensor MRI (DT-MRI) [20], [23], [24]. From the latter—which is often considered a tool of choice because it is nondestructive does not use ionizing radiation, and it is inherently 3D—the average direction of myocardial structures can be extracted

from the principal directions, or eigenvectors, of the diffusion tensor at every voxel [21], [23]–[25]. Fiber orientations has been correlated to the first eigenvector, while the secondary eigenvalue has been associated to the general direction of myocardial sheetlets [23], [26]. A third direction orthogonal to the first two describes the so-called sheet-normal direction [25]. Being an orthonormal set, if two vectorial directions are known, the third is granted by means of the cross product. To facilitate visualization and quantification of these structures, directional information is often expressed in terms of angular measurements with respect to a local coordinate system with components in the circumferential, radial (endocardium towards epicardium), and longitudinal (apex to base) directions [18], [27]. In this research, the planes formed by any two of these directions are referred by the normal (e.g., the *radial plane* refers to the plane shared by the circumferential and longitudinal direction, tangent to the surface of the heart). Thus, the angular descriptors that define the fiber direction, or \vec{f} as shown in Figure 5.1, and can be described as follows: The helix angle, α , the angle that the projection of the primary eigenvector in the local radial plane makes with the circumferential direction, and the transverse, or imbrication, angle, α' , made by the projection of the primary eigenvector in the longitudinal plane and the local circumferential direction [18], [28]. Likewise, (also in Figure 5.1) sheet structure, or \vec{s} , has been associated to the angles made by projections of the second eigenvector in the longitudinal and circumferential planes and the local radial direction, respectively labeled β and β' [25], [29]. While fiber orientation angles follow a quasilinear transmural profile (Figure 5.2), the spatial patterns of the angles associated with sheet distribution are not obviously evident, and their analysis is based on their population, which is semiquantitatively expressed with

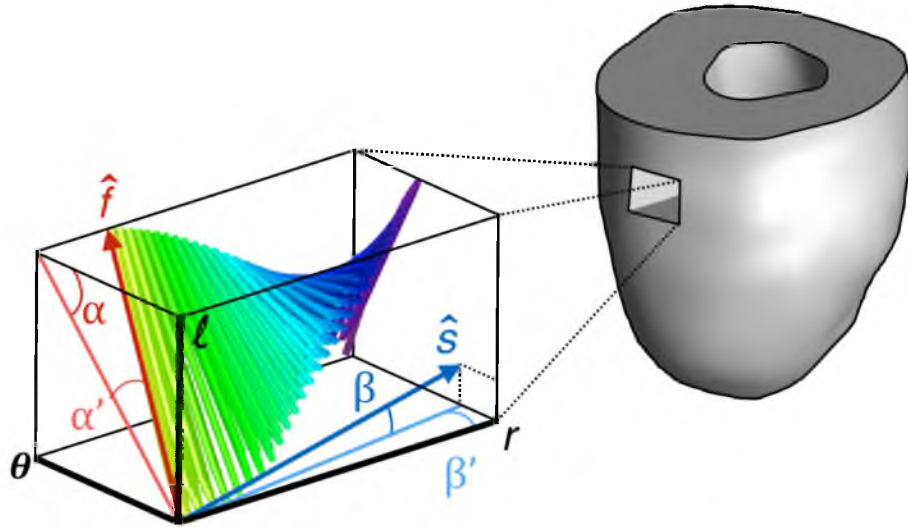


Figure 5.1: Angular quantification of fiber and sheet structures. The local fiber (\hat{f}) or sheet direction (\hat{s}) can be expressed numerically as rotations about a coordinate system defined by the local circumferential, radial and longitudinal direction (θ , r , and l , respectively). The fiber orientation is described by the helix α (which takes on negative values on the epicardium) and transverse α' angles. A similar approach can be used to express sheet orientation (β and β').

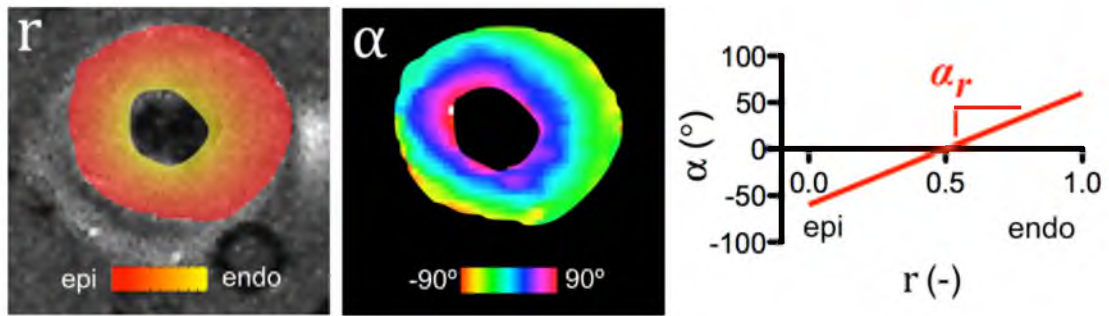


Figure 5.2: Spatial distribution of LV helix angle along the radial direction. Normalization of the transmural location of a given point in the myocardium (left) allows description of angular measures of structure. For instance, helix angle (center) can roughly be described by a first order polynomial (right). Some alterations due to cardiac deformation can be measured by the magnitude of the transmural helix angle slope α_r .

histograms [1], [10], [13], [14].

Differences between systole and diastole have been observed with DT-MRI both *in vivo* in human volunteers, as well as *ex vivo* with the aid of isolated heart preparations. These changes have been explained with geometrical models, which, although are not readily integrated in terms of continuum mechanics, because material anisotropy and contractility are not expressly included, provide nevertheless a basic explanation about the relationship between fiber shortening and wall thickening through conservation of volume [30]. The most evident changes between systolic and diastolic structural configuration consists of an overall longitudinal fiber alignment at systole with respect to diastole [1], [31], [32]. Compared to diastole, with the wall thickness normalized, systolic fiber structure has a larger transmural rate of change of the helical angle, α , which is also visible on a histogram as an increased population of voxels with relatively large angles. A similar trend is observed on transverse angles, α' , which tend to populate towards zero in diastole [1], [14]. Sheet information is scarcer, and sometimes expressed using the complementary angles to those used here, but a distinct reconfiguration of the transverse angle, β , has been observed as a shift from having relatively large populations of voxels near larger angles at diastole, towards a larger concentration near zero degrees at systole [10], [13].

Structural dynamics are a promising frontier for the study of mechanisms enabling key aspects of cardiac function though research focused on variability and disease characterization. However, obtaining detailed description of the 3D structural dynamics of the beating heart faces severe technical and experimental challenges. In the last 10 years, advances structural imaging *in vivo* via DT-MRI and in atlas generation have,

respectively, introduced whole-tensor statistics, and enabled the acquisition of structural information in the living heart [33]–[37]. Currently, *in vivo* DT-MRI lacks resolution and requires long scan times to acquire the type of data needed for comprehensive variability analysis and atlas construction, but it is feasible to achieve a reasonable amount of data at a discrete points in the cardiac cycle [10], [38], [39]. In theory, this information could be employed to extrapolate temporal evolution with the aid of computational biomechanics.

Although computational models of ventricular mechanics have long existed, many of them with outstanding descriptive and predictive power, little research has been focused on the design and experimental validation of models dedicated to study predictions of dynamic structural behavior. Instead, the role of ventricular structure in the context of numerical simulations has been considered mostly from a sensitivity standpoint, whereby the performance of computer simulations has been measured against global metrics like pressure and volume, and to some extent, stress and strain distribution. Many of these previous studies have yielded an improved understanding regarding the role of parameterization and distribution of helical structure in ventricular modeling, and have pointed to the need for further investigation regarding the role of additional aspects of structural characterization on the performance of computational models [3], [15], [19], [30], [40]–[42].

The main objective for this research is to identify a numerical approach for extending the application of a discrete set of initial structural DT-MRI information to the rest of the cardiac cycle. To this end, the investigation approach has been divided into two components: First, a systematic evaluation of selected structural dynamics

simulations against experimental data and, second, evaluation of the applicability of the method beyond validation points. The first step was intended to prioritize practical elements needed to capture left-ventricular (LV) structural dynamics, and also to address some of the ambiguity surrounding the nature and net effect of sheet structures on simulated deformation. The second step served to integrate simulated structural dynamics with common visualization techniques of cardiac structure.

5.3 Methods

5.3.1 Overview

This study focused on three aspects of numerical simulation of structural alterations: material assumptions, inclusion of subject-specific data, and application of simulated deformation to DT-MRI. To this end, structural data were acquired *ex vivo* in an isolated heart preparation at early diastole (EAD), end diastole (ED) and end systole (ES). DT-MRI at EAD provided an initial set of structural data to be transformed, by means of simulations, into predictions at ED and ES, which were then compared to experimental observations. Finite-element mechanical simulations of healthy rat left ventricles were constructed in four variations as follows:

- (i) An isotropic material model was used for the passive myocardium and contraction in the circumferential direction, and was designed to represent basic geometrical changes disregarding contribution from a realistic structural modeling.
- (ii) Myocardial tissue was assumed to be transverse isotropic with a fiber structure characterized by linear transmural variation of α from -60° at the epicardium to 60° at the endocardium, and similarly for α' , except from -20° to 20° . Case *ii* assumes a

nominal, population-based approximation of fiber structure based on the literature [43], [44]. By being transversely isotropic, the material model disregards sheet structures.

- (iii) A transversely isotropic material was used, but a subject-specific fiber distribution is generated from DT-MRI data.
- (iv) An orthotropic material model was used to allow inclusion of subject-specific sheet structure from DT-MRI.

These combinations of material behavior and integration of structural data can be thought as modeling approaches of increasing sophistication depending on the available input information to the analyst. To study the application of simulated deformation to a set of initial set of DT-MRI data, two approaches previously presented in the literature were investigated [35], [37]. (Vectorial quantities are identified with an arrow accent, and tensorial variable appear underscored.) First, a “rotation-only” approach was followed, whereby the simulation-generated deformation map $\vec{\varphi}(\vec{X}) = \vec{X} - \vec{x}$ (\vec{X} and \vec{x} represent reference and current coordinates, respectively) was applied to displace a vector, say \vec{E} but also applies to \vec{f} and \vec{s} , which was then rotated according to

$$\vec{e}_R = \underline{R}\vec{E}, \quad (5.1)$$

where uppercase represents the vector in the current configuration, and \underline{R} was obtained from single-value decomposition of the deformation gradient

$$\underline{F} = \frac{\partial \vec{x}}{\partial \vec{X}}. \quad (5.2)$$

Second, the structural vectors were translated in the same manner, but with “full deformation” by direct application of the deformation gradient \underline{F} , or

$$\vec{e}_F = \frac{F\vec{E}}{\|F\vec{E}\|}. \quad (5.3)$$

Each of the four finite-element predictions yielded two approximations of the actual set of alterations observed on the experimental. The simulated and experimental structural alterations were semiquantitatively compared by measuring transmural variations in helical angle and construction of histograms as described in recent literature [1], [10], [14]. Additional information from *in vivo* imaging (CINE and displacement-encoded MRI), was used to characterize the volume changes, strain, and torsion on the living heart as additional measures of simulation performance.

5.3.2 *In Vivo* Imaging

5.3.2.1 Animal Preparation

All animal protocols were approved by the Institutional Animal Care and Use Committee at the University of Utah in accordance to the *Guide for the Care and Use of Laboratory Animals* issued by the US National Institutes of health (NIH Publication No. 85-23, rev. 1996). Adult male (300 g) Sprague Dawley rats (n=3) were anesthetized with 1–3% isoflurane and 0.6-0.9 L/min O₂. The animals were placed prone inside a 72-mm ID quadrature volume RF coil in a Bruker Biospec 7T imaging instrument (Bruker Biospin, MA, USA). Continuous monitoring of vital signs (respiration, temperature, heart rate ECG, and oxygen saturation) was performed using a MR-compatible physiological monitoring system (SA Instruments, Stony Brook, NY).

5.3.2.2 Anatomical Imaging

Retrospectively gated CINE, eight-short slices covering the left ventricle, was used to measure morphology and volume change along the cardiac cycle (Fast Low Angle Shot, FLASH, 20.0 ms TR, 2.0 ms TE, 40 x 40 mm FOV, 96 x 96 matrix size). Images were semi-automatically segmented (Amira, Visage imaging, CA), and volume was approximated via Simpson's rule [41].

5.3.2.3 Displacement-Encoded MRI

Displacement encoding with stimulated echoes DENSE pulse sequence [45], [46] was used to measure deformation on three slices (3 mm thick) at the LV base, middle and apex. Other pertinent imaging specifications included 20.0 ms TR, 2.0 ms TE, 40 x 40 mm FOV, 96 x 96 matrix size, and 0.7 cycles/mm motion encoding gradients in the read, phase, and slice directions. DENSE phase images (after k-space subtraction and low pass filtering) were unwrapped using a fuzzy logic approach, and offset corrected using registration of magnitude images [46], [47]. The displacements were used to calculate the average systolic circumferential and radial strain (with ED as the reference) at each slice based on the principal components of the Lagrange strain, slice rotations, and longitudinal torsion according to previous studies in rat hearts [48], [49].

5.3.3 *Ex Vivo* Imaging

5.3.3.1 Isolated Heart Apparatus

A custom, MRI-compatible isolated heart preparation was constructed for DT-MRI of the heart at the three states under consideration. After animal euthanasia, each of the

hearts (n=3) was rapidly extracted and cannulated for retrograde perfusion with 100% oxygenated Tyrode's solution (and modifications described below) at about 90 mmHg at approximately 15 mL/min with a positive displacement pump (Cole-Palmer, Item# EW-77120-42). A temperature-controlled perfusion chamber and imaging coil assembly was built to allow imaging while keeping the heart vertically hanging from the cannula, which is essential to maintain adequate perfusion. A balloon was inserted in the ventricle to control volume based on *in vivo* readings for each subject, and a small perforation was made by the pulmonary vein to allow perfusion fluid outflow. Continuous pressure, temperature, and electrical activity measurements were used to adjust perfusion rates depending on the state of the heart (diastole required slightly more flow rate to maintain pressure).

5.3.3.2 Cardioplegic Treatment

The goal of the study was to acquire DT-MRI at EAD, ED and ES [1], [13], [31]. After initial conditioning of about 5 min of perfusion using Tyrode's solution (in mM: NaCl 140.0, Glucose 11.0, KCl 5.4, HEPES 5.0, CaCl₂ 1.8, MgCl₂ 1.0), the heart was treated to emulate conditions at EAD by being arrested with an elevated KCl concentration solution (in mM: NaCl 105.0, KCl 25.0, Glucose 11.0, HEPES 10.0, MgCl₂ 1.0) and the balloon was kept deflated allowing the tissue to remain lax. For ED, the heart was arrested by similar means, but the balloon was adjusted to ED volume. Contracture (ES) was induced by adding LiCl (in mM: LiCl 125.0, Glucose 11.0, HEPES 10.0, KCl 5, CaCl₂ 2.5, MgCl₂ 1.0). The solutions were titrated to pH 7.4 and kept at 37 °C for the duration of the experiments. Bovine serum albumen was added to

achieve osmotic equilibrium (4 mg/L). Change of solutions included perfusion for approximately 15 min prior to imaging to achieve tissue equilibrium.

5.3.3.3 DT-MRI

During each state in the MRI compatible apparatus, DT-MRI was acquired using a velocity-compensated, multishot segmented EPI sequence (FOV 36.3x36.3 mm, 128x128 pixels, 4 slices, TR 2000ms, TE 20ms, 24 directions and 900 mm/cm b-value). Additional slices were acquired for morphological characterization using a FLASH sequence (256x256 pixels, 4 long slices, 4 short slices, TR 10ms, TE 1.5 ms, 30° flip). The diffusion tensor and principal directions were reconstructed from diffusion weighted images with a nonlinear least squares reconstruction protocol [45]. After the isolated heart preparation, the specimens were fixed and scanned at high resolution to generate fiber tracts (Spin Echo Sequence, FOV 30x30x30 mm 128x128x128 pixels, TR 2000ms, TE 20ms).

5.3.4 Computational Mechanics

5.3.4.1 LV Meshing and Boundary Conditions

Approximately 75% of the myocardial volume of rat LV (n=3), starting at the apex until approximately two-thirds in the longitudinal direction towards the base, was discretized into a finite element domain composed of linear hexahedral elements (TrueGrid, XYZ Applications, CA, USA) using semi-automatically labeled images obtained from long- and short-axis anatomical MRI (FEI Life Sciences, OR, USA). Labeled data were combined to create a single surface by means of implicit spline

fitting [50]. The final mesh was composed of approximately 8,000 elements, after evaluating models from about 3,000 to 13,200 element meshes, per 3% convergence analysis using maximum first principal strains and maximum effective shear under 4kPa pressurization on the LV cavity (Figure 5.3). For simulation of the validation points, the endocardial LV surface was pressurized to 2.3 kPa (17 mmHg) and 15 kPa (113 mmHg) for ED and ES, respectively. For simulation of the whole cardiac cycle, pressures and volumes load curves were constructed based on a confidence interval of *in vivo* volume measurements and pressure waveforms of the healthy rat [51]. Additional constraining was achieved by surrounding the LV with a block made of a low-stiffness, compressible support material and applying the boundary conditions shown in Figure 5.4 [52]. The additional mesh was also applied to facilitate interpolation of displacements near the LV outer surface. (Supporting material was modeled as Neo-Hookean with modulus of elasticity of 0.01 kPa, and Poisson ratio of zero—a 10-fold change on support material stiffness had indiscernible effects on the solution.)

5.3.4.2 Constitutive Relationships of Myocardial Material

A single Fung-type strain energy function was used to model all the material representations of passive constitutive behavior in this study [53], [54]. The myocardium is assumed to be homogeneous across the ventricular volume, hyperelastic, and nearly incompressible. The strain energy, W , was assumed to follow

$$W = \frac{1}{2}c(e^{\varrho} - 1) + \frac{1}{2}K \ln(J) \quad (5.4)$$

where K is the material's bulk modulus set at 200 kPa, $J = \det(\underline{F})$ and, for the

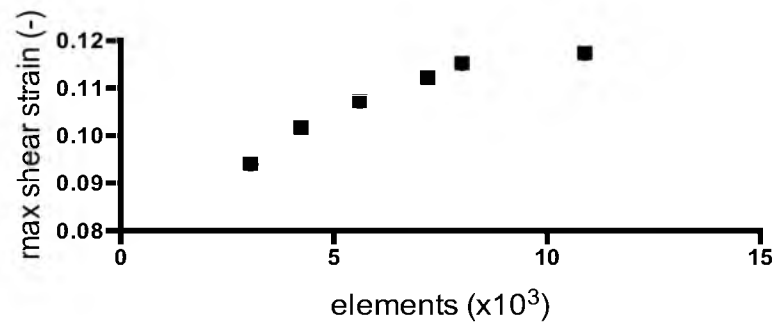


Figure 5.3: Mesh convergence via maximum shear strain. As the number of elements increases, the maximum shear strain converges to a constant number. Convergence (at 3%) occurred at approximately 8 thousand elements.

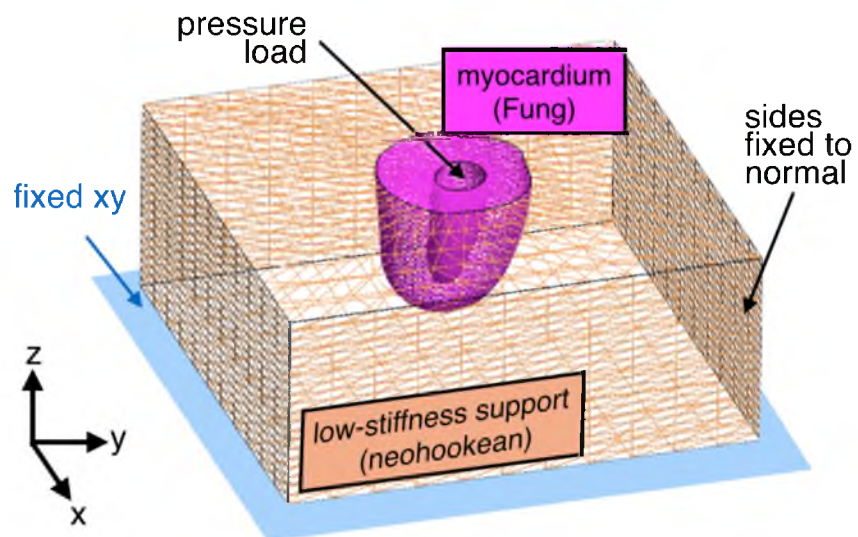


Figure 5.4: Representative finite-element model of the LV wall. The myocardium was represented as a mesh extracted from anatomical imaging embedded in a support block. LV mechanics were represented by a Fung-type constitutive model, and the surroundings were composed of a compliant and compressible material. The boundary conditions included the displacement constraints are shown and also a hydrostatic pressure in the endocardial surface.

myocardium in terms the local coordinate system defined by fiber and sheet structures

$$Q = c_1 E_{ff}^2 + c_2 E_{ss}^2 + c_3 E_{nn}^2 + c_4 (E_{fs}^2 + E_{sf}^2) + c_5 (E_{nf}^2 + E_{fn}^2) + c_6 (E_{sn}^2 + E_{ns}^2). \quad (5.5)$$

The coefficients c , and c_1 through c_6 defined the stiffness and isotropy with respect to the deviatoric components of the Green-Lagrange strain tensor in local coordinates, i.e., E_{ij} where i or $j = f, s, n$ for fiber, sheet and sheet-normal, respectively. For instance, an isotropic material with identical response along all directions would imply $c_1 = c_2 = c_3$, and $c_4 = c_5 = c_6$. To enable a more even comparison on the deviatoric behavior of the different decoupled constitutive models, Lagrangian augmentation iterations were added to enforce incompressibility by keeping changes of volume under 1%. The material coefficients used to define isotropic, and transverse isotropic behavior were based on previous studies on perfused heart of rat hearts [54]. Orthotropic shear response was based on shear experimental data from dog tissue [55]. To reduce effects of biological variability on material coefficients, c was adjusted to match the simulated response to the measured ED volume of each subject [7], [56]. The material coefficients prior to subject-specific scaling are listed in Table 5.1, and response curves are shown in Figure 5.5. A frame-invariant formulation of the strain energy function was used to integrate (5.5) into the solver [57].

Active stress generation responsible for ventricular contraction was modeled with an implementation of active contraction based on a steady-state specialization of the time-varying elastance modification to Hill's active muscle contraction model [58], [59]. In short, the total simulated Cauchy stress tensor \underline{T} results from superimposed

Table 5.1: Material coefficient sets for passive myocardium

	c (kPa)	c_1 (-)	c_2 (-)	c_3 (-)	c_4 (-)	c_5 (-)	c_6 (-)
<i>isotropic</i>	0.35	9.2	9.2	9.2	7.4	7.4	7.4
<i>transverse iso.*</i>	1.3	9.2	2	2	3.7	2	3.7
<i>orthotropic</i>	0.75	20.2	1.4	0.3	8.1	6.0	3.7

* These coefficients were obtained from perfused rat heart data [54]. Additional coefficients were obtained from curve fitting.

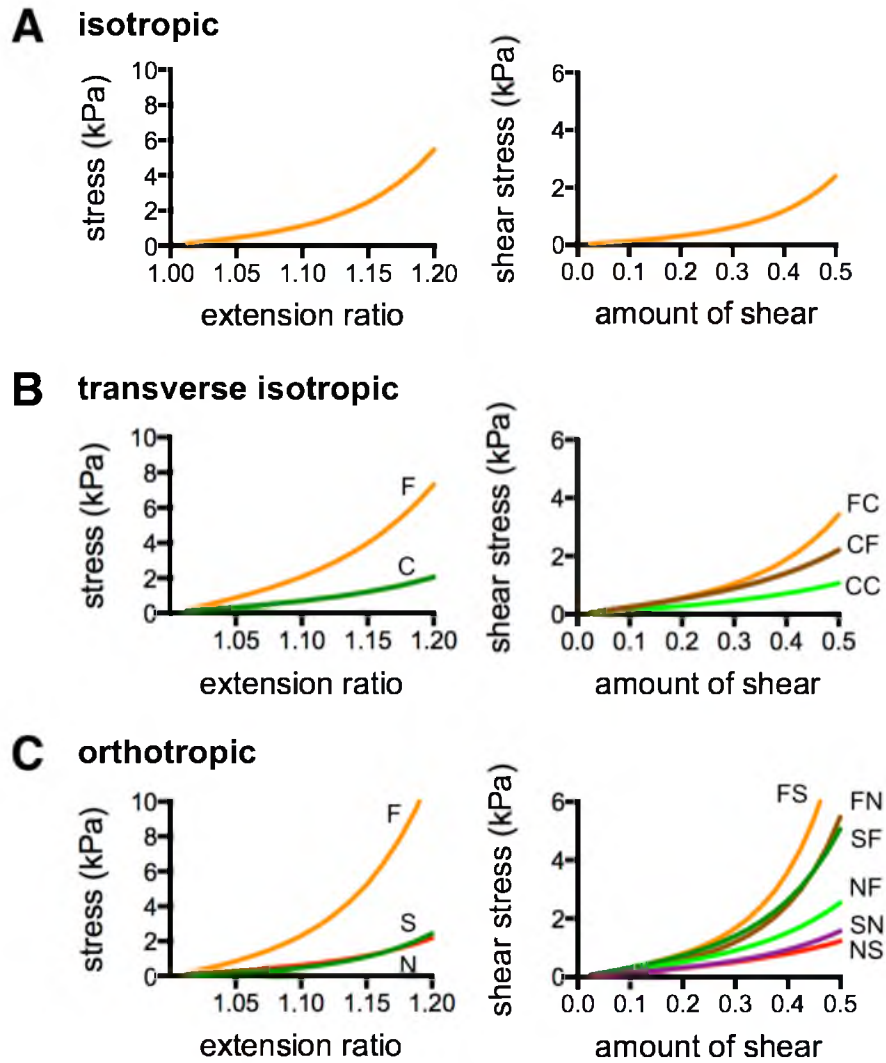


Figure 5.5: Material symmetry assumptions. The simulation cases included three material behavior models: (A, top) isotropic, (B, middle) transverse isotropic, where the fiber and cross-fiber directions exhibit different responses (labeled F and C), and orthotropic (C, bottom), where shear response was defined in terms of the local fiber (F), sheet (S), and sheet-normal (N) directions.

contributions from the passive material response $\underline{T}^{[p]}$, and an active component $\underline{T}^{[a]}$ along \vec{f} , or

$$\underline{T} = \underline{T}^{[p]} + \underline{T}^{[a]} \vec{f} \otimes \vec{f}. \quad (5.6)$$

The active component was defined as a function of fiber stretch and a scaling parameter $C_{lc}(t)$, which determines the shape of the activation curve [45], as:

$$\underline{T}^{[a]} = T_{max} \frac{Ca_0^2}{Ca_0^2 + ECa_{50}^2(l)} C_{lc}(t), \quad (5.7)$$

where the maximum activation stress $T_{max} = 135.7$ kPa was based on the isometric tension at the peak intracellular calcium concentration, $Ca_0 = 4.35$ μ M. Calcium sensitivity, $ECa_{50}^2(l)$, was modeled with respect to the maximum calcium concentration $(Ca_0)_{max} = 4.35$ μ M, the zero-tension sarcomere length, $l_0 = 1.58$ μ m, an experimentally derived weight $B = 4.75$ μ m⁻¹ and the current sarcomere length, l , resulting from scaling the resting sarcomere length (1.2 μ m) by the fiber stretch,

$$ECa_{50}^2 = \frac{(Ca_0^2)_{max}}{\sqrt{\exp(B(l - l_0)) - 1}}. \quad (5.8)$$

Both the passive and active representations of cardiac tissue are available in the FEBio Software Suite, which was used for all the finite-element simulations in this study [60].

5.3.4.3 Inclusion of Structural Information into Mechanical Model

To incorporate structural information, defined at the element centroid, into the model, a local coordinate system was constructed using a distribution of potentials, described as the Laplace-Dirichlet method for structural definition [27]. However, instead of a rule-based approach, structural information was defined with volumetric polynomials with respect to the radial and longitudinal coordinates ℓ and r assuming

circumferential symmetry. Then, the angular value at each element was used to rotate the longitudinal or radial direction (defined as the gradients ℓ and r) into alignment with the local fiber or sheet orientation, respectively. The polynomial form and order, N , was defined based on spatial angular distributions, and previous investigations [29], [61], [62], in terms of coefficients k_i^α , $k_i^{\alpha'}$, k_i^β , and $k_i^{\beta'}$ where $i = 1, 2, \dots, N$, as:

$$\alpha(\ell, r) = k_1^\alpha + k_2^\alpha r + k_3^\alpha \ell, \quad (5.8)$$

$$\alpha'(\ell, r) = k_1^{\alpha'} + k_2^{\alpha'} r + k_3^{\alpha'} \ell + k_4^{\alpha'} r^2 + k_5^{\alpha'} \ell^2 + k_6^{\alpha'} r \ell, \quad (5.9)$$

$$\beta(\ell, r) = k_1^\beta + k_2^\beta r + k_3^\beta \ell, \text{ and} \quad (5.10)$$

$$\beta'(\ell, r) = k_1^{\beta'} + k_2^{\beta'} r + k_3^{\beta'} \ell + k_4^{\beta'} r^2. \quad (5.11)$$

For case (i) all structural coefficients were zero, as well as for case (ii) except that $k_1^\alpha = -60$, $k_2^\alpha = 120$, $k_1^{\alpha'} = -20$, and $k_2^{\alpha'} = 40$. The coefficient sets for cases (iii) and (iv) are shown in Table 5.2.

5.3.5 Deformation and Visualization Across Cardiac Cycle

Given an approximation of cardiac deformation, angular measures of fiber and sheet structures were obtained by regenerating the gradients that define the local coordinate system using current (deformed) nodal positions, and interpolating their values to the deformed DT-MRI slices by means of inverse isoperimetric mapping [63]. The same approach was applied to fiber tracts obtained from high-resolution DT-MRI of a fixed LV specimen (TracVis, Center for Biomedical Imaging, Massachusetts General Hospital, MA, USA).

Table 5.2: Fiber and sheet distribution coefficients

<i>fiber</i>									
subject	(α)			(α')					
	k_1^α	k_2^α	k_3^α	$k_1^{\alpha'}$	$k_2^{\alpha'}$	$k_3^{\alpha'}$	$k_4^{\alpha'}$	$k_5^{\alpha'}$	$k_6^{\alpha'}$
	(°)	(-)	(-)	(°)	(-)	(-)	(-)	(-)	(-)
<i>rat 1</i>	75.6	126	-153	152	730	-619	-59.7	473	-702
<i>rat 2</i>	54.1	77.8	-103	308	830	233	-44.8	110	-851
<i>rat 3</i>	100	109	-162	569	1068	-1639	-67.0	1084	-1051

<i>sheet</i>							
subject	(β)			(β')			
	k_1^β	k_2^β	k_3^β	$k_1^{\beta'}$	$k_2^{\beta'}$	$k_3^{\beta'}$	$k_4^{\beta'}$
	(°)	(-)	(-)	(°)	(-)	(-)	(-)
<i>rat 1</i>	-4.61	-314	639	-38.0	47.0	-101	106
<i>rat 2</i>	-36.0	-497	480	49.3	-44.2	-169	151
<i>rat 3</i>	10.9	-654	639	55.9	-55.4	-180	165

5.4 Results

5.4.1 *In Vivo* Cardiac Kinematics

Mean ejection fraction (EF) was measured to be 0.71 ± 0.04 (mean \pm SD). Circumferential strain in the base, midventricle, and apex was -0.23 ± 0.05 , -0.27 ± 0.04 , and -0.28 ± 0.04 , respectively. Radial strain values in the same locations were 0.55 ± 0.06 , 0.57 ± 0.06 , and 0.49 ± 0.07 . (Recall that *in vivo* strain measures correspond to systolic values having ED as reference.) Longitudinal torsion was 1.3 ± 0.8 degrees/mm⁻¹ based on slice rotations of $-15.9^\circ \pm 3.3$ at the base, $-14.2^\circ \pm 4.3$ at the midventricle, and $-11.5^\circ \pm 3.5$ at the apex. These values agreed with previous studies on healthy rats of similar size [49], [64].

5.4.2 Morphology of Isolated Heart Preparation

The morphological variations in the isolated heart were similar to those observed *in vivo*, including volumetric variations and wall thickness (Figure 5.6). Electrical activity and regular pressure fluctuations were briefly observed in between imaging protocols during solution change intervals indicating tissue viability. The total experimental time varied between 40-50 min from excision to completion of the last imaging protocol. In the isolated heart, the mean wall thickness of the three subjects on the investigated states was (mean \pm SD) 3.17 ± 0.6 in EAD, 1.83 ± 0.6 in ED, and 3.65 ± 0.2 in ES. The same measurements *in vivo* yielded 2.8 ± 0.3 in EAD, 2.00 ± 0.1 in ED, and 3.63 ± 0.2 in ES. The mean of volume of the three subjects on the investigated states was 127.2 ± 16.7 μ L for EAD, 382.8 ± 72.1 μ L for ED, and 76.3 ± 22.8 for ES. The same measurements for these subjects *in vivo* were 132.0 ± 68.1 μ L for EAD, 310.3 ± 37.8

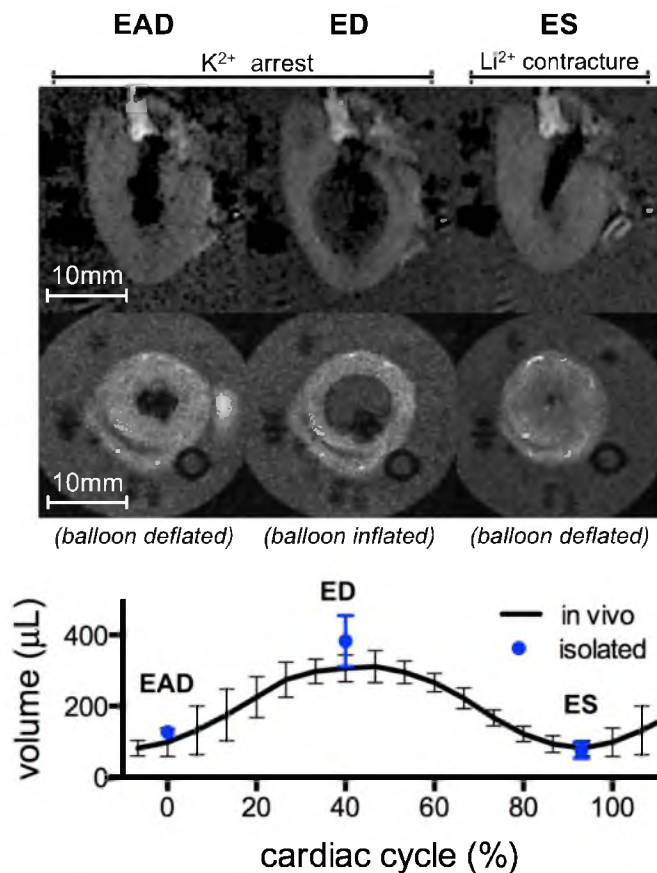


Figure 5.6: Isolated heart during arrest and contracture. The isolated heart exhibited morphological alterations coherent with the target cardiac states. Compared to potassium-arrested heart (top left), balloon inflation resulted in volume increase and wall thinning (top center), and deflation accompanied by contracture-inducing solution produced volume decrease and wall thickening (top right). These morphological alterations were similar to individual and group measurements *in vivo* at early diastole (EAD), end diastole (ED), and end systole (ES).

μL for ED, and 82.3 ± 22.5 for ES. Despite the general agreement, on a given subject, there was a slight tendency for overinflating the balloon at ED.

5.4.3 Structural Variations of Isolated Heart Preparation

The total transmural change of helical angle at ES was approximately 26% larger than the same measure at ED (increase to approximately 130° from 100° in rat 1, to 110° from 90° in rat 2, and to 140° from 110° in rat 3), which was consistent to the longitudinal alignment described in previous studies [13], [14]. The histograms of helical distribution in Figure 5.7 showed a larger population near zero for ED than ES. Transverse angle distribution showed increased circumferential alignment during systole (larger population about zero). The clearest difference in structural distribution was seen on the sheet angle histogram, which showed a marked increase in pixel count near zero at ES. Similar characteristic observations have been made in previous DT-MRI studies using isolated heart preparations.

5.4.4 Simulated Myocardial Kinematics

Some of the principal parameters associated with LV deformation are listed in Table 5.3. The finite-element predictions of volumetric changes were in excellent agreement with measurements *in vivo*, with errors of less than 10% in ED and ES volumes as well as EF. As expected, the isotropic model grossly underestimated the amount of systolic longitudinal torsion, but the models with more realistic fiber distribution (cases *ii* through *iv*) had the tendency of overestimation. There was also good agreement in terms of circumferential strain values, although the mild longitudinal change observed

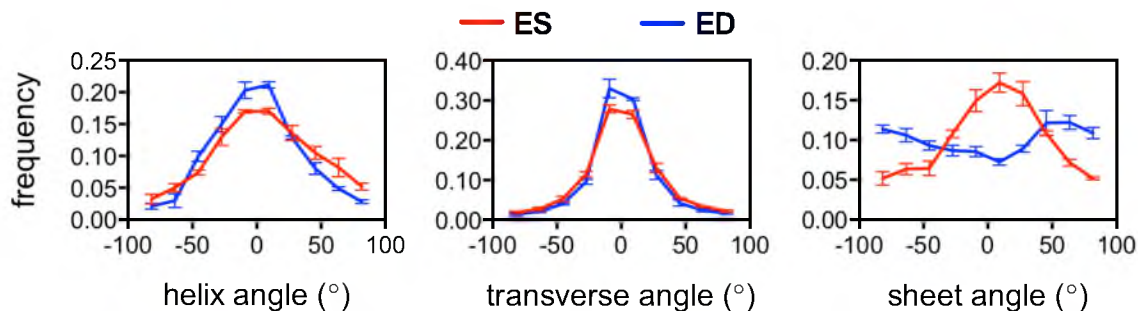


Figure 5.7: Histogram representation of structural angles populations at ED and ES. Compared to ED, systolic helix angle population is more concentrated at higher angles, which indicates longitudinal alignment. During diastole, the transverse fiber angle population increases near zero degrees, which indicates alignment in the circumferential direction. Sheet angle distribution is markedly different between both states and tends to concentrate about zero at ES.

Table 5.3. Mean simulated kinematic parameters

		<i>in vivo</i>	<i>case i</i>	<i>case ii</i>	<i>case iii</i>	<i>case iv</i>
<i>ESV</i>	μL	82(22)	95(35)	104(21)	100(22)	103(25)
<i>EDV</i>	μL	310(38)	298(47)	311(30)	313(38)	302(31)
<i>EF</i>	μL	0.71(0.10)	0.69(0.09)	0.67(0.03)	0.68(0.03)	0.66(0.05)
<i>torsion</i>	$^{\circ}/\text{mm}$	1.3(0.8)	0.07(0.04)	1.73(0.14)	2.17(0.35)	2.24(0.44)
E_{θ} (<i>base</i>)	(-)	-0.28(0.04)	-0.28(0.02)	-0.24(0.09)	-0.28(0.01)	-0.28(0.02)
E_{θ} (<i>mid</i>)	(-)	-0.27(0.04)	-0.28(0.02)	-0.24(0.09)	-0.29(0.02)	-0.28(0.02)
E_{θ} (<i>apex</i>)	(-)	-0.23(0.05)	-0.29(0.02)	-0.25(0.07)	-0.30(0.01)	-0.29(0.01)
E_r (<i>base</i>)	(-)	0.49(0.07)	0.26(0.12)	0.68(0.27)	0.75(0.09)	0.74(0.12)
E_r (<i>mid</i>)	(-)	0.57(0.06)	0.43(0.11)	0.66(0.30)	0.77(0.09)	0.82(0.12)
E_r (<i>apex</i>)	(-)	0.55(0.06)	0.41(0.14)	0.64(0.18)	0.75(0.20)	0.75(0.20)
T_{max}	(kPa)	-	25(8)	56(4)	53(14)	44(9)
c	(kPa)	-	0.14(0.09)	0.95(0.48)	0.77(0.31)	0.27(0.17)

Values shown correspond to mean (std. deviation). *ESV* = end-systolic volume, *EDV* = end-diastolic volume, *EF* = ejection fraction, E_{θ} = circumferential strain, E_r = longitudinal strain.

experimentally (larger *in vivo* strain at the base compared to the apex) was reversed likely due to the boundary conditions. Some systematic variation in terms of radial strain were observed, whereby the measure fell below the *in vivo* measurements in case *i*, and above in the remaining cases. Parameter identification resulted in reduction of the stiffness parameter c in all cases except case (*iii*) where the reduction was insignificant.

The average computation time per simulation including systole and diastole was 30 min on a 2 GHz, 12-core workstation, but simulations in cases (*i*) and (*iv*) required approximately twice as much time to reach convergence.

5.4.5 Simulated Structural Alterations

Each numerical result produced a set of results for each, the rotation-only and the full-deformation, approach for application of the deformation to the initial DT-MRI data. Table 5.4 shows a comparison of ED and ES helix angle slopes. While all of the systolic values show some degree of longitudinal alignment, values obtained by applying only a rotation vary more drastically among simulation cases with (*i*) being the smallest at 3%, and (*ii*) being the largest at 30%. (Variation *in vivo* was about 26%.) Using full deformation, case (*i*) largely overestimates the measurement, and case (*iv*) underestimates it, although, unlike the first, the last case also does so using the rotation-only approach. Cases (*ii*) and (*iii*) show reasonable agreement with the experimental observation.

Histograms of the simulated structural alterations using the rotation-only approach appear in Figure 5.8. Case (*i*) yielded no visible changes in helix, transverse, or sheet.

Table 5.4: Mean transmural helix angle slope

			<i>case i</i>	<i>case ii</i>	<i>case iii</i>	<i>case iv</i>
<i>rotation-only</i>	<i>ED</i>	(°)	107(24)	117(27)	113(28)	113(28)
	<i>ES</i>	(°)	110(15)	151(33)	138(32)	131(29)
	<i>change*</i>	(%)	3	30	22	16
<i>full deformation</i>	<i>ED</i>	(°)	92(24)	102(27)	95(23)	101(26)
	<i>ES</i>	(°)	145(48)	134(29)	117(26)	114(25)
	<i>change*</i>	(%)	58	31	23	13

Values shown correspond to mean (std. deviation). * measured with respect to ED using means.

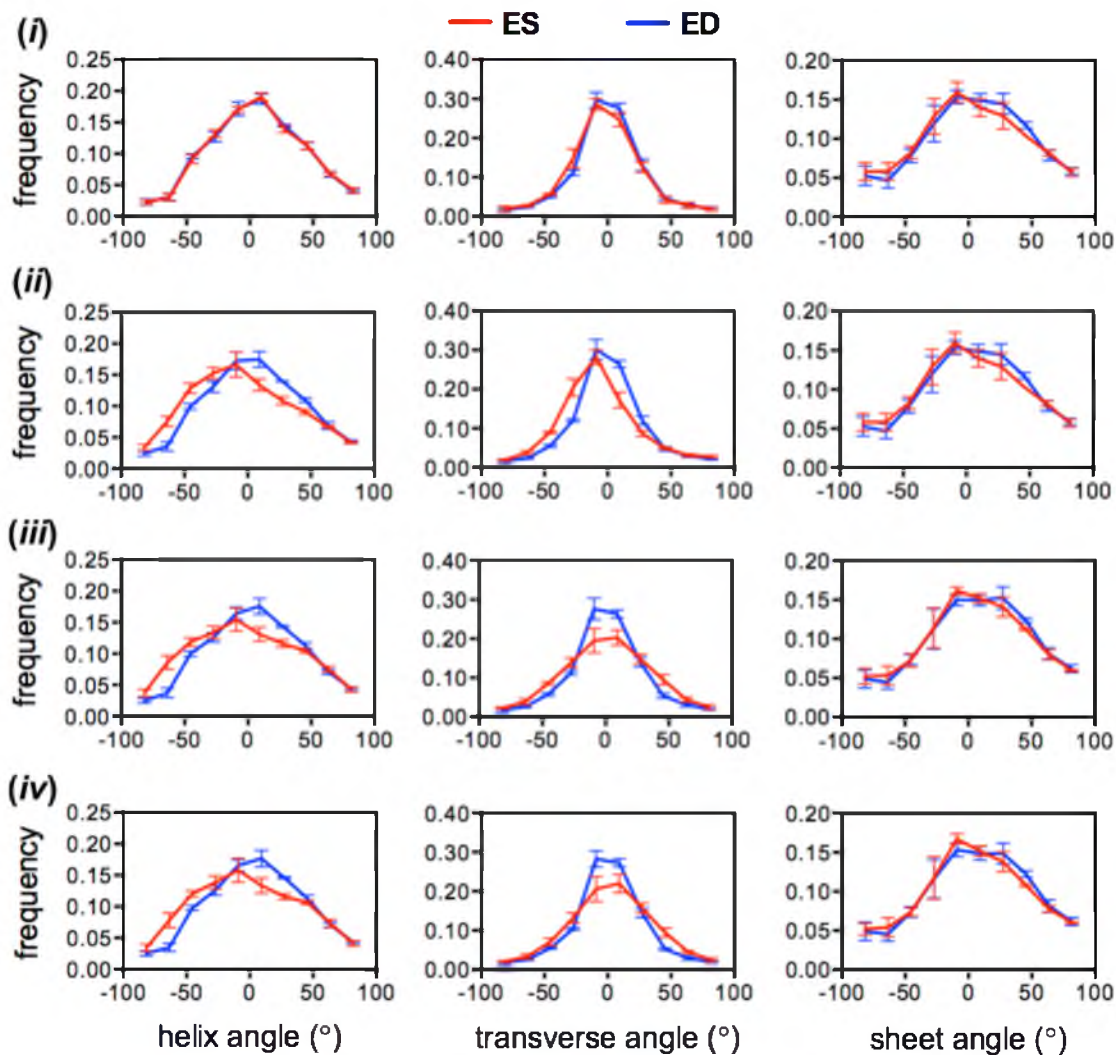


Figure 5.8: Histograms of structural angle populations using the “rotation-only” approach to transform DTI data from an initial time point to ED and ES. The deformation results from case (iii) do not show any difference between states and constitute a poor prediction with respect to the experimental observations (top). Cases (ii through iv) produced similar helix angle distribution alterations, which better describe experimental data. Transverse angle alterations are more realistic in cases (iii) and (iv). Using the rotation-only approach produced no visible differences in sheet angle distributions.

Additional cases produced similar changes in helix angle populations. These were consistent with experimental observations that indicate some circumferential alignment of transverse angles in ED, which is more visible in cases (*ii* and *iv*). Sheet angle population remained unchanged regardless of the simulation case.

Results obtained using the full-deformation approach appear in Figure 5.9. Helix angle population for case (*i*) follows a pattern consistent with the transmural slope, where there is a drastically different distribution compared to the rotation-only method. Distribution changes of the same angular measure in the other cases are similar to that obtained with the rotation-only method, and also consistent with slope measurements in that helical changes are less marked on case (*iv*). Circumferential alignment of transverse angles can be observed in all the simulation cases. Unlike in the rotation-only approach, sheet distribution changes start to appear in (*ii*) through (*iv*), and appear to be slightly more evident in case (*iv*), although not to the same extent as the alterations observed experimentally.

Some examples of extrapolation beyond the verification points can be seen in Figure 5.10 where the nodal locations have been readjusted for a more realistic representation of cardiac motion (fixed apex). The initial DT-MRI information at EAD is shown at zero time followed by some frames of the simulated progression using case (*iii*) across the cardiac cycle. At each time, there is a corresponding change in volume and wall thickness, as well as fiber rotations, which are more evident at 60% and ES where element deformation can be observed on the model, and a larger area of helix angles close to -90 (shades of red) can be seen on near the epicardium. Similar observations can be made on the tractography representation of ED and ES shown in

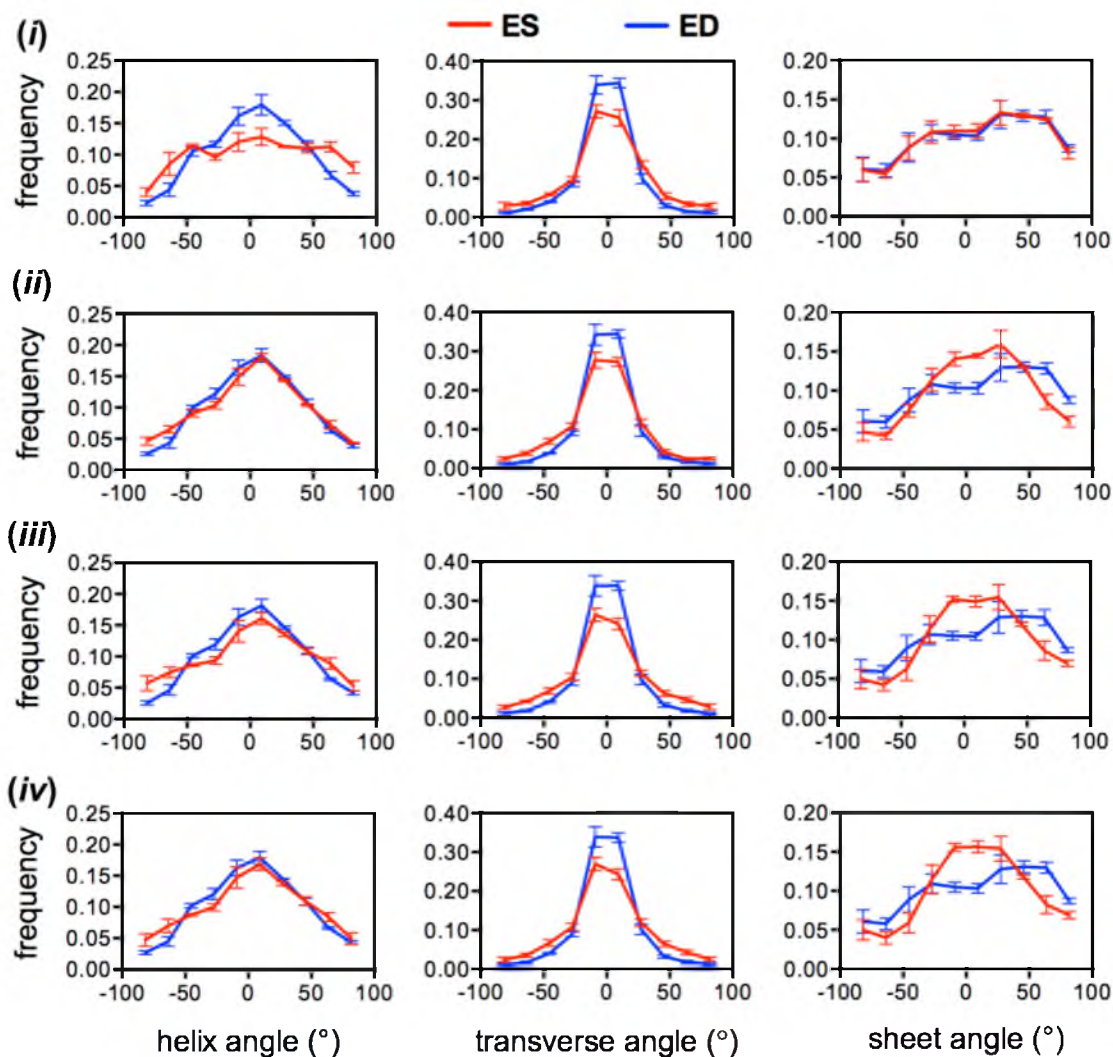


Figure 5.9. Histograms of structural angle populations using the “full deformation” approach to transform DTI data from an initial time point to ED and ES. Helix angle populations generated with deformation estimate (i) showed both longitudinal alignment at ES and circumferential enlightenment at ED, but no alterations of sheet angle populations. Fiber and sheet alterations could be seen on case (ii), although fiber distribution changes are more concentrated in the negative population. Cases (iii) and (iv) showed the most similar alterations with respect to experimental data, particularly in sheet angle population.

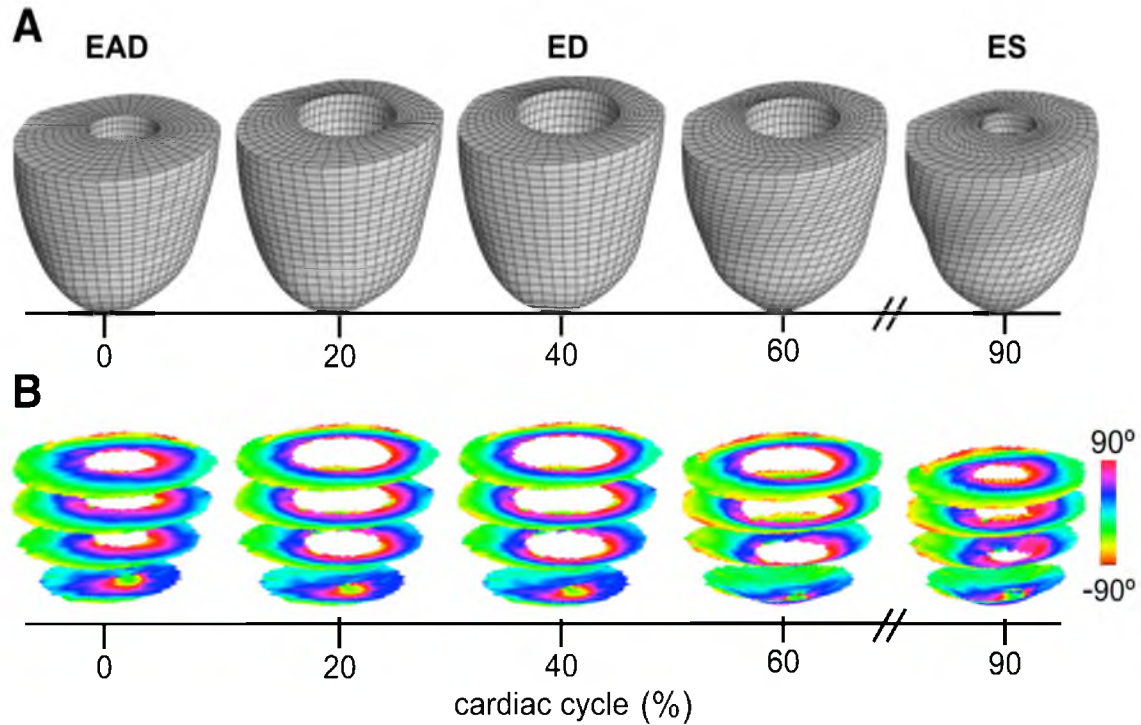


Figure 5.10: Warping DTI data across the cardiac cycle. The finite-element model (A) was used to generate deformation estimates at times beyond the validation points (ED and ES). The modeling approach follows a realistic temporal representation of pressure, volume, and contractility as opposed to a linear scaling of the deformation at known time points.

Figure 5.11, where the epicardial longitudinal alignment of helical structure can be seen directly

5.5 Discussion

Simulated structural alterations can be obtained in different manners, as evident in Figures 5.8 and 5.9. Interpretation of results in light of tissue kinematics, like strain and torsion measures shown in Table 5.3, can be used to obtain more reasonable approximations than simply relying on volume and volumetric variations (such as EF). The ability to achieve simulated LV volumes similar to those *in vivo* regardless of the modeling strategy is in agreement with previous studies, which for the most part show that pressure and volume can be relatively insensitive to structural variations [3], [40]. Radial strain (associated to wall thickening) was more sensitive to structural information, and the subject specific models (cases *iii* and *iv*) had the tendency to overestimate experimental values partially confirming previous speculations [40]. In the context of this study, radial strain serves as an indicator of the mechanism for LV volume variation, which in the cases with realistic structural input (cases *ii* through *iv*) was mediated by wall thickening, unlike the isotropic material case (*i*) where cavity volume changed due to elongation. This distinction can be used to avoid misleading results. For instance, direct application of the deformation gradient to warp data using case (*i*) yielded ES longitudinal alignment and ED circumferential alignment (Figure 5.8 top), even though the model completely disregards myocardial fiber and sheet distribution. This can be explained because each of the components of the fiber orientation vector were stretched by different amounts, resulting in an angular change.

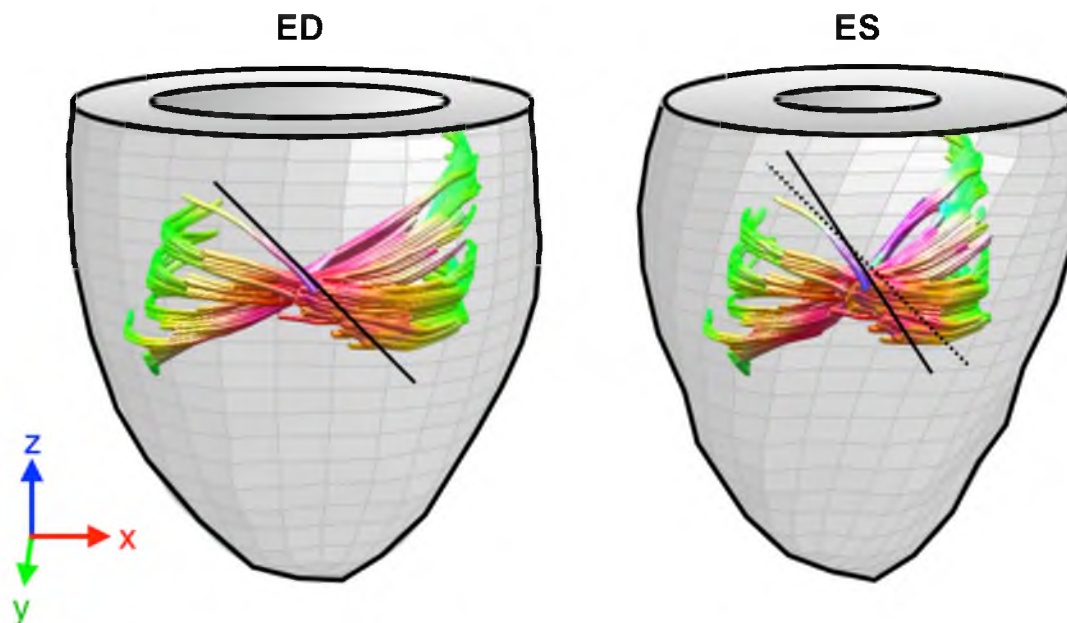


Figure 5.11: Deformed tracts of a collection of fibers in a longitudinal isocline along the radial direction. Comparing the local inclination of an epicardial fiber tract at ED (black line, left), with respect to its warping configuration at ES (right) showed longitudinal alignment typical of systolic structural state.

Comparing the rotation-only with the full deformation results indicates that, for the more realistic cases (*ii* through *iv*), fiber structure alterations, i.e., helical and transverse angle distributions, seems to be respectively mediated by rotation, because transmural slopes (Table 5.3) and histograms (Figures 5.8 and 5.9) show similar distribution regardless of the warping approach. The same cannot be said for the sheet angle population, which appears to be mediated mostly by transmural shear. Out of the simulated cases, the orthotropic model (*iv*) has the most visible alteration of sheet angle with case (*iii*) being a close second. These models have in common that subject-specific structural information was used as structural input. These data may be required if sheet deformation is the subject of study, e.g., to simulate structural alteration in hearts with hypertrophic cardiomyopathy, because it is possible that the distinct structural alterations between ED and ES caused by the disease [10] may be associated with shear stiffening in the transmural direction.

Being an exploration study, a fundamental limitation of this study is its qualitative nature. Although consistent numerical quantifications were used whenever possible, it is currently impossible to say with certainty the precise accuracy of simulated structural alterations. Thus, interpretation of results was limited to clear trends on the visible evidence. Secondly, this study included intricate experimental as well as numerical components containing several assumptions; the most important include the effectiveness of the isolated heart preparation, and basic components on the numerical simulation. Although Langendorff rigs have been used to study cardiac physiology for at least 50 years, recent investigations using MRI-compatible isolated hearts were used as platform to ensure experimental soundness [1], [13], [31], [65], [66]. In this research,

additional steps were taken to ensure proper irrigation, temperature control, and verification of tissue viability. It is worth noting that *in vivo* DT-MRI in the rat heart was not demonstrated until very recently [67]. Nevertheless, the presented extrapolation method is still expected to be useful, since scan time for whole-heart coverage across the cardiac cycle will be prohibitive [38], [39]. In terms of the numerical simulations, the ventricle was assumed to be homogeneous and stress-free in its unloaded configuration. These assumptions were invoked partly due to the lack of experimental data needed to include these features onto the models, although preliminary numerical studies indicate that myocardial residual stress has a relatively small effect in ventricular deformation [7], [68], [69]. Further, cases (*iii* and *iv*) include some spatial heterogeneity at least from a structural sense.

This research can stem in several future directions. First, the authors believe that the methodology in this report applies without loss of generality to *in vivo* DT-MRI results. Using this imaging technology may reduce the experimental error associated with the isolated heart, and will be a more suitable alternative to validate structural atlases of the living heart. There are also improvements to be made from a numerical perspective, such as the inclusion of mechanics-based image registration to warp the results. This would facilitate point-to-point comparison of structural data for error quantification, and mesh construction with quadratic elements to improve mesh convergence and increase computational efficiency. Finally, additional research towards incorporating the right ventricle could be performed by expanding the computational strategy in combination with high-resolution *in vivo* DT-MRI.

5.6 Conflicts of Interest

None of the authors have any conflict of interests to report.

5.7 Acknowledgements

The authors would like to thank Samer Merchant, and Osama Abdullah at the Small Animal Imaging Facility at the University of Utah. Dr. Jeffrey Weiss, Steve Maas, and Dave Rawlins at the Musculoskeletal Research Laboratories (U. of Utah) are gratefully acknowledged for their assistance with computational mechanics. Additional thanks to Garvin Tran, David Zou, and Adam Schmidt for laboratory assistance. This work is funded by the National Health Institutes (grants R01 HL092055, and S10 RR023017).

5.8 References

- [1] P. W. Hales, J. E. Schneider, R. A. B. Burton, B. J. Wright, C. Bollensdorff, and P. Kohl, "Histo-anatomical structure of the living isolated rat heart in two contraction states assessed by diffusion tensor MRI," *Prog. Biophys. Mol. Biol.*, vol. 110, no. 2–3, pp. 319–30, Oct. 2012.
- [2] N. H. L. Kuijpers, E. Hermeling, P. H. M. Bovendeerd, T. Delhaas, and F. W. Prinzen, "Modeling cardiac electromechanics and mechano-electrical coupling in dyssynchronous and failing hearts: insight from adaptive computer models," *J. Cardiovasc. Transl. Res.*, vol. 5, no. 2, pp. 159–69, Apr. 2012.
- [3] T. Arts, P. Bovendeerd, T. Delhaas, and F. Prinzen, "Modeling the relation between cardiac pump function and myofiber mechanics," *J. Biomech.*, vol. 36, no. 5, pp. 731–6, May 2003.
- [4] P. H. Bovendeerd, T. Arts, J. M. Huyghe, D. H. van Campen, and R. S. Reneman, "Dependence of local left ventricular wall mechanics on myocardial fiber orientation: a model study," *J. Biomech.*, vol. 25, no. 10, pp. 1129–40, Oct. 1992.
- [5] L. K. Waldman, D. Nosan, F. Villarreal, and J. W. Covell, "Relation between transmural deformation and local myofiber direction in canine left ventricle," *Circ. Res.*, vol. 63, no. 3, pp. 550–62, Sep. 1988.
- [6] G. J. Strijkers, A. Bouts, W. M. Blankesteyn, T. H. J. M. Peeters, A. Vilanova, M. C. van Prooijen, H. M. H. F. Sanders, E. Heijman, and K. Nicolay, "Diffusion tensor imaging of left ventricular remodeling in response to myocardial infarction in the mouse," *NMR Biomed.*, vol. 22, no. 2, pp. 182–90, Feb. 2009.
- [7] J. C. Walker, M. B. Ratcliffe, P. Zhang, A. W. Wallace, B. Fata, E. W. Hsu, D. Saloner, and J. M. Guccione, "MRI-based finite-element analysis of left ventricular aneurysm," *Am. J. Physiol. Heart Circ. Physiol.*, vol. 289, no. 2, pp. H692–700, Aug. 2005.
- [8] O. M. Abdullah, S. G. Drakos, N. A. Diakos, O. Wever-Pinzon, A. G. Kfoury, J. Stehlik, C. H. Selzman, B. B. Reid, K. Brunisholz, D. R. Verma, C. Myrick, F. B. Sachse, D. Y. Li, and E. W. Hsu, "Characterization of diffuse fibrosis in the failing human heart via diffusion tensor imaging and quantitative histological validation," *NMR Biomed.*, vol. 27, no. 11, pp. 1378–86, Nov. 2014.
- [9] B. Schmitt, K. Fedarava, J. Falkenberg, K. Rothaus, N. K. Bodhey, C. Reischauer, S. Kozerke, B. Schnackenburg, D. Westermann, P. P. Lunkenheimer, R. H. Anderson, F. Berger, and T. Kuehne, "Three-dimensional alignment of the aggregated myocytes in the normal and hypertrophic murine heart," *J. Appl. Physiol.*, vol. 107, no. 3, pp. 921–7, Sep. 2009.

- [10] P. F. Ferreira, P. J. Kilner, L.-A. McGill, S. Nielles-Vallespin, A. D. Scott, S. Y. Ho, K. P. McCarthy, M. M. Haba, T. F. Ismail, P. D. Gatehouse, R. de Silva, A. R. Lyon, S. K. Prasad, D. N. Firmin, and D. J. Pennell, "In vivo cardiovascular magnetic resonance diffusion tensor imaging shows evidence of abnormal myocardial laminar orientations and mobility in hypertrophic cardiomyopathy," *J. Cardiovasc. Magn. Reson.*, vol. 16, p. 87, Jan. 2014.
- [11] L. Axel, V. J. Wedeen, and D. B. Ennis, "Probing dynamic myocardial microstructure with cardiac magnetic resonance diffusion tensor imaging," *J. Cardiovasc. Magn. Reson.*, vol. 16, p. 89, Jan. 2014.
- [12] D. A. MacKenna, J. H. Omens, and J. W. Covell, "Left ventricular perimysial collagen fibers uncoil rather than stretch during diastolic filling," *Basic Res. Cardiol.*, vol. 91, no. 2, pp. 111–22, Jan.
- [13] M. Lohezic, I. Teh, C. Bollensdorff, R. Peyronnet, P. W. Hales, V. Grau, P. Kohl, and J. E. Schneider, "Interrogation of living myocardium in multiple static deformation states with diffusion tensor and diffusion spectrum imaging," *Prog. Biophys. Mol. Biol.*, vol. 115, no. 2–3, pp. 213–25, Aug. 2014.
- [14] C. T. Stoeck, A. Kalinowska, C. von Deuster, J. Harmer, R. W. Chan, M. Niemann, R. Manka, D. Atkinson, D. E. Sosnovik, C. Mekkaoui, and S. Kozerke, "Dual-phase cardiac diffusion tensor imaging with strain correction," *PLoS One*, vol. 9, no. 9, p. e107159, Jan. 2014.
- [15] J. Rijcken, P. H. Bovendeerd, A. J. Schoofs, D. H. van Campen, and T. Arts, "Optimization of cardiac fiber orientation for homogeneous fiber strain during ejection," *Ann. Biomed. Eng.*, vol. 27, no. 3, pp. 289–97, 1999.
- [16] C. Yang, C. Tang, I. Haber, T. Geva, and P. J. del Nido, "In vivo MRI-based 3D FSI RV/LV models for human right ventricle and patch design for potential computer-aided surgery optimization," *Comput. Struct.*, vol. 85, no. 11–14, pp. 988–997, 2009.
- [17] J. Wenk, L. Ge, and Z. Zhang, "A coupled biventricular finite element and lumped-parameter circulatory system model of heart failure," *Comput. Methods in Biomechanics and Bioengineering*, vol. 16, no. 8, pp. 807–818, 2013.
- [18] D. D. Streeter and W. T. Hanna, "Engineering mechanics for successive states in canine left ventricular myocardium. II. Fiber angle and sarcomere length," *Circ. Res.*, vol. 33, no. 6, pp. 656–64, Dec. 1973.
- [19] T. Arts, K. D. Costa, J. W. Covell, and A. D. McCulloch, "Relating myocardial laminar architecture to shear strain and muscle fiber orientation," *Am. J. Physiol. Heart Circ. Physiol.*, vol. 280, no. 5, pp. H2222–9, May 2001.

- [20] I. J. LeGrice, B. H. Smaill, L. Z. Chai, S. G. Edgar, J. B. Gavin, and P. J. Hunter, "Laminar structure of the heart: ventricular myocyte arrangement and connective tissue architecture in the dog," *Am. J. Physiol. Circ. Physiol.*, vol. 269, no. 2, pp. H571–H582, 1995.
- [21] P. A. Helm, H.-J. Tseng, L. Younes, E. R. McVeigh, and R. L. Winslow, "Ex vivo 3D diffusion tensor imaging and quantification of cardiac laminar structure," *Magn. Reson. Med.*, vol. 54, no. 4, pp. 850–9, Oct. 2005.
- [22] P. P. Lunkenheimer, K. Redmann, N. Kling, X. Jiang, K. Rothaus, C. W. Cryer, F. Wübbeling, P. Niederer, P. U. Heitz, S. Y. Ho, and R. H. Anderson, "Three-dimensional architecture of the left ventricular myocardium," *Anat. Rec. A. Discov. Mol. Cell. Evol. Biol.*, vol. 288, no. 6, pp. 565–78, Jun. 2006.
- [23] E. W. Hsu, A. L. Muzikant, S. A. Matulevicius, R. C. Penland, and C. S. Henriquez, "Magnetic resonance myocardial fiber-orientation mapping with direct histological correlation," *Am. J. Physiol.*, vol. 5 pt 2, no. 274, pp. H1627–H1627, 1998.
- [24] D. F. Scollan, A. Holmes, R. Winslow, and J. Forder, "Histological validation of myocardial microstructure obtained from diffusion tensor magnetic resonance imaging," *Am. J. Physiol.*, vol. 275, no. 6 Pt 2, pp. H2308–18, Dec. 1998.
- [25] W.-Y. I. Tseng, V. J. Wedeen, T. G. Reese, R. N. Smith, and E. F. Halpern, "Diffusion tensor MRI of myocardial fibers and sheets: correspondence with visible cut-face texture," *J. Magn. Reson. Imaging*, vol. 17, no. 1, pp. 31–42, Jan. 2003.
- [26] P. Helm, M. F. Beg, M. I. Miller, and R. L. Winslow, "Measuring and mapping cardiac fiber and laminar architecture using diffusion tensor MR imaging," *Ann. N. Y. Acad. Sci.*, vol. 1047, pp. 296–307, Jun. 2005.
- [27] J. D. Bayer, R. C. Blake, G. Plank, and N. A. Trayanova, "A novel rule-based algorithm for assigning myocardial fiber orientation to computational heart models," *Ann. Biomed. Eng.*, vol. 40, no. 10, pp. 2243–54, Oct. 2012.
- [28] R. H. Anderson, D. Sanchez-Quintana, K. Redmann, and P. P. Lunkenheimer, "How are the myocytes aggregated so as to make up the ventricular mass?" *Semin. Thorac. Cardiovasc. Surg.*, pp. 76–86, Jan. 2007.
- [29] S. H. Gilbert, A. P. Benson, P. Li, and A. V Holden, "Regional localisation of left ventricular sheet structure: integration with current models of cardiac fibre, sheet and band structure," *Eur. J. Cardio-Thoracic Surg.*, vol. 32, no. 2, pp. 231–49, Aug. 2007.
- [30] P. J. Hunter, A. D. McCulloch, and H. E. ter Keurs, "Modelling the mechanical

- properties of cardiac muscle,” *Prog. Biophys. Mol. Biol.*, vol. 69, no. 2–3, pp. 289–331, Jan. 1998.
- [31] J. Chen, W. Liu, H. Zhang, L. Lacy, X. Yang, S.-K. Song, S. A. Wickline, and X. Yu, “Regional ventricular wall thickening reflects changes in cardiac fiber and sheet structure during contraction: quantification with diffusion tensor MRI,” *Am. J. Physiol. Circ. Physiol.*, vol. 289, no. 5, pp. H1898–907, Nov. 2005.
- [32] M. Smerup, J. Partridge, P. Agger, S. Ringgaard, M. Pedersen, S. Petersen, J. M. Hasenkam, P. Niederer, P. P. Lunkenheimer, and R. H. Anderson, “A mathematical model of the mechanical link between shortening of the cardiomyocytes and systolic deformation of the left ventricular myocardium,” *Technol. Health Care*, vol. 21, no. 1, pp. 63–79, Jan. 2013.
- [33] L.-A. McGill, T. F. Ismail, S. Nielles-Vallespin, P. F. Ferreira, A. D. Scott, M. Roughton, P. J. Kilner, S. Y. Ho, K. P. McCarthy, P. D. Gatehouse, R. de Silva, P. Speier, T. Feiweier, C. Mekkaoui, D. E. Sosnovik, S. K. Prasad, D. N. Firmin, and D. J. Pennell, “Reproducibility of in-vivo diffusion tensor cardiovascular magnetic resonance in hypertrophic cardiomyopathy,” *J. Cardiovasc. Magn. Reson.*, vol. 14, p. 86, Jan. 2012.
- [34] C. Nguyen, Z. Fan, B. Sharif, Y. He, R. Dharmakumar, D. S. Berman, and D. Li, “In vivo three-dimensional high resolution cardiac diffusion-weighted MRI: a motion compensated diffusion-prepared balanced steady-state free precession approach,” *Magn. Reson. Med.*, no. Nov 20, Nov. 2013.
- [35] D. C. Alexander, C. Pierpaoli, P. J. Basser, and J. C. Gee, “Spatial transformations of diffusion tensor magnetic resonance images,” *IEEE Trans. Med. Imaging*, vol. 20, no. 11, pp. 1131–9, Nov. 2001.
- [36] P. Lorenzen, B. Davis, and S. Joshi, “Unbiased atlas formation via large deformations metric mapping,” *Med. Image Comput. Comput. Assist. Interv.*, vol. 8, no. Pt 2, pp. 411–8, Jan. 2005.
- [37] J.-M. Peyrat, M. Sermesant, X. Pennec, H. Delingette, C. Xu, E. R. McVeigh, and N. Ayache, “A computational framework for the statistical analysis of cardiac diffusion tensors: application to a small database of canine hearts,” *IEEE Trans. Med. Imaging*, vol. 26, no. 11, pp. 1500–14, Nov. 2007.
- [38] A. Z. Lau, E. M. Tunnicliffe, R. Frost, P. J. Koopmans, D. J. Tyler, and M. D. Robson, “Accelerated human cardiac diffusion tensor imaging using simultaneous multislice imaging,” *Magn. Reson. Med.*, vol. 73, no. 3, pp. 995–1004, Mar. 2015.
- [39] S. Nielles-Vallespin, C. Mekkaoui, P. Gatehouse, T. G. Reese, J. Keegan, P. F. Ferreira, S. Collins, P. Speier, T. Feiweier, R. de Silva, M. P. Jackowski, D. J.

- Pennell, D. E. Sosnovik, and D. Firmin, "In vivo diffusion tensor MRI of the human heart: reproducibility of breath-hold and navigator-based approaches," *Magn. Reson. Med.*, vol. 70, no. 2, pp. 454–65, Aug. 2013.
- [40] V. Carapella, R. Bordas, P. Pathmanathan, M. Lohezic, J. E. Schneider, P. Kohl, K. Burrage, and V. Grau, "Quantitative study of the effect of tissue microstructure on contraction in a computational model of rat left ventricle," *PLoS One*, vol. 9, no. 4, p. e92792, Apr. 2014.
- [41] T. Delhaas, W. Kroon, W. Decaluwe, M. Rubbens, P. Bovendeerd, and T. Arts, "Structure and torsion of the normal and situs inversus totalis cardiac left ventricle. I. Experimental data in humans," *Am. J. Physiol. Heart Circ. Physiol.*, vol. 295, no. 1, pp. H197–201, Jul. 2008.
- [42] T. P. Usyk, R. Mazhari, and A. D. McCulloch, "Effect of laminar orthotropic myofiber architecture on regional stress and strain in the canine left ventricle," *J. Elast. Phys. Sci. Solids*, vol. 61, no. 1–3, pp. 143–164, Jul. 2000.
- [43] L. J. Healy, Y. Jiang, and E. W. Hsu, "Quantitative comparison of myocardial fiber structure between mice, rabbit, and sheep using diffusion tensor cardiovascular magnetic resonance," *J. Cardiovasc. Magn. Reson.*, vol. 13, p. 74, Jan. 2011.
- [44] S. H. Gilbert, D. Benoist, A. P. Benson, E. White, S. F. Tanner, A. V. Holden, H. Dobrzynski, O. Bernus, and A. Radjenovic, "Visualization and quantification of whole rat heart laminar structure using high-spatial resolution contrast-enhanced MRI," *AJP Hear. Circ. Physiol.*, vol. 302, no. 1, pp. H287–H298, 2012.
- [45] A. H. Aletras, S. Ding, R. S. Balaban, and H. Wen, "DENSE: displacement encoding with stimulated echoes in cardiac functional MRI," *J. Magn. Reson.*, vol. 137, no. 1, pp. 247–52, Mar. 1999.
- [46] D. Kim, W. D. Gilson, C. M. Kramer, and F. H. Epstein, "Myocardial tissue tracking with two-dimensional cine imaging: development and initial evaluation," *Radiology*, vol. 230, no. 3, pp. 862–71, 2004.
- [47] M. Costantini, "A novel phase unwrapping method based on network programming," *IEEE Trans. Geosci. Remote Sens.*, vol. 36, no. 3, pp. 813–821, 1998.
- [48] A. D. Gomez, S. S. Merchant, and E. W. Hsu, "Accurate high-resolution measurements of 3D tissue dynamics with registration-enhanced displacement encoded MRI," *IEEE Trans. Med. Imaging*, vol. 33, no. 6, pp. 1350–62, Jun. 2014.
- [49] W. Liu, M. W. Ashford, J. Chen, M. P. Watkins, T. A. Williams, S. A. Wickline,

- and X. Yu, “MR tagging demonstrates quantitative differences in regional ventricular wall motion in mice, rats, and men,” *Am. J. Physiol. Heart Circ. Physiol.*, vol. 291, no. 5, pp. H2515–21, Nov. 2006.
- [50] M. Rouhani and A. D. Sappa, “Implicit B-spline fitting using the 3L algorithm,” in *2011 18th IEEE International Conference on Image Processing*, 2011, pp. 893–896.
- [51] P. Pacher, T. Nagayama, P. Mukhopadhyay, S. B atkai, and D. A. Kass, “Measurement of cardiac function using pressure-volume conductance catheter technique in mice and rats,” *Nat. Protoc.*, vol. 3, no. 9, pp. 1422–34, Jan. 2008.
- [52] A. I. Veress, G. T. Gullberg, and J. A. Weiss, “Measurement of strain in the left ventricle during diastole with CINE-MRI and deformable image registration,” *J. Biomech. Eng.*, vol. 127, no. 7, pp. 1195–1207, Jul. 2005.
- [53] K. D. Costa, J. W. Holmes, and A. D. McCulloch, “Modelling cardiac mechanical properties in three dimensions,” *Philos. Trans. R. Soc. A Math. Phys. Eng. Sci.*, vol. 359, no. 1783, pp. 1233–1250, Jun. 2001.
- [54] J. H. Omens, D. A. MacKenna, and A. D. McCulloch, “Measurement of strain and analysis of stress in resting rat left ventricular myocardium,” *J. Biomech.*, vol. 26, no. 6, pp. 665–676, Jun. 1993.
- [55] S. Dokos, B. H. Smaill, A. A. Young, and I. J. LeGrice, “Shear properties of passive ventricular myocardium,” *Am. J. Physiol. Heart Circ. Physiol.*, vol. 283, no. 6, pp. H2650–9, Dec. 2002.
- [56] K. Sun, N. Stander, C.-S. Jhun, Z. Zhang, T. Suzuki, G.-Y. Wang, S. Maythem, A. W. Wallace, E. E. Tseng, A. J. Baker, D. Saloner, D. R. Einstein, M. B. Ratcliffe, and J. M. Guccione, “A computationally efficient formal optimization of regional myocardial contractility in a sheep with left ventricular aneurysm,” *J. Biomech. Eng.*, vol. 131, no. 11, pp. 1–21, 2009.
- [57] G. A. Ateshian and K. D. Costa, “A frame-invariant formulation of Fung elasticity,” *J. Biomech.*, vol. 42, no. 6, pp. 781–5, Apr. 2009.
- [58] J. M. Guccione and A. D. McCulloch, “Mechanics of active contraction in cardiac muscle: part I--constitutive relations for fiber stress that describe deactivation,” *J. Biomech. Eng.*, vol. 115, no. 1, pp. 72–81, Feb. 1993.
- [59] J. M. Guccione, L. K. Waldman, and A. D. McCulloch, “Mechanics of active contraction in cardiac muscle: part II--cylindrical models of the systolic left ventricle,” *J. Biomech. Eng.*, vol. 115, no. 1, pp. 82–90, Feb. 1993.
- [60] S. A. Maas, B. J. Ellis, G. A. Ateshian, and J. A. Weiss, “FEBio: finite elements

- for biomechanics,” *J. Biomech. Eng.*, vol. 134, no. 1, pp. 011005–1,–10, Jan. 2012.
- [61] D. D. Streeter, R. N. Vaishnav, D. J. Patel, H. M. Spotnitz, J. Ross, and E. H. Sonnenblick, “Stress distribution in the canine left ventricle during diastole and systole,” *Biophys. J.*, vol. 10, no. 4, pp. 345–63, Apr. 1970.
- [62] L. Geerts, P. Bovendeerd, K. Nicolay, and T. Arts, “Characterization of the normal cardiac myofiber field in goat measured with MR-diffusion tensor imaging,” *Am. J. Physiol. Heart Circ. Physiol.*, vol. 283, no. 1, pp. H139–45, Jul. 2002.
- [63] K.-Y. Yuan, Y.-S. Huang, H.-T. Yang, and T. H. H. Pian, “The inverse mapping and distortion measures for 8-node hexahedral isoparametric elements,” *Comput. Mech.*, vol. 14, no. 2, pp. 189–199, May 1994.
- [64] N. Bachner-Hinenzon, O. Ertracht, M. Leitman, Z. Vered, S. Shimoni, R. Beeri, O. Binah, and D. Adam, “Layer-specific strain analysis by speckle tracking echocardiography reveals differences in left ventricular function between rats and humans,” *Am. J. Physiol. Heart Circ. Physiol.*, vol. 299, no. 3, pp. 664–672, 2010.
- [65] H. E. Carstensen, “In vitro test of heart muscle viability,” *Scand. J. Thorac. Cardiovasc. Surg.*, vol. 9, no. 3, pp. 200–5, Jan. 1975.
- [66] P. F. Mannaioni, R. Levi, and A. Giotti, “Anaphylaxis in the heart isolated according to the Langendorff method and treated with reserpine and bretylium,” *Boll. Soc. Ital. Biol. Sper.*, vol. 37, pp. 1140–4, Nov. 1961.
- [67] C. Welsh, E. Di Bella, and E. Hsu, “Higher-order motion-compensation for in vivo cardiac diffusion tensor imaging in rats,” *IEEE Trans. Med. Imaging*, Mar. 2015.
- [68] N. S. Phatak, S. A. Maas, A. I. Veress, N. A. Pack, E. V. R. Di Bella, and J. A. Weiss, “Strain measurement in the left ventricle during systole with deformable image registration,” *Med. Image Anal.*, vol. 13, no. 2, pp. 354–61, Apr. 2009.
- [69] H. M. Wang, X. Y. Luo, H. Gao, R. W. Ogden, B. E. Griffith, C. Berry, and T. J. Wang, “A modified Holzapfel-Ogden law for a residually stressed finite strain model of the human left ventricle in diastole,” *Biomech. Model. Mechanobiol.*, vol. 13, no. 1, pp. 99–113, Jan. 2014.

CHAPTER 6

DT-MRI OBSERVATIONS OF FIBER STRUCTURE ALTERATIONS AS A COMPENSATORY MECHANISM FOR VENTRICULAR PRESSURE OVERLOAD: PRELIMINARY RESULTS¹

6.1 Abstract

Right ventricular failure has been associated with a number of cardiovascular conditions affecting a large portion of the population. Pressure overload is a common etiology relatable to deterioration of right ventricular function, but there is a need for improved understanding regarding tissue structure remodeling and other biomechanical factors involved in failure and recovery. Following the development and implementation of a reversible animal model for right ventricular failure due to pressure overload, a group of cardiac specimens in health, failure, and after recovery from failure was analyzed using diffusion tensor MRI. Analysis of the majority of the ventricular volume was achieved through an automated generation of potential-based local coordinates. In order to elucidate different types of adaptation to pressure overload, the failure group was subdivided according to the mean wall thickness of the right ventricle with respect to the left. By introducing the subdivision, trends suggesting thickness-

¹Included with permission by Arnold D. Gomez, Osama Abdullah, Stephen McKellar, and Edward W. Hsu from a manuscript in preparation entitled: DT-MRI Observations of Fiber Structure Alterations as a Compensatory Mechanism for Ventricular Pressure Overload.

mediated longitudinal alignment of fiber structure were observed, which may explain conflicting reports on previous investigations on similar models

6.2 Introduction

Right ventricular failure (RVF) is a deadly deterioration of pump function that can occur over a range of pathological processes including ischemia, as well as pressure or volume overload, often associated with left ventricular (LV) coronary disease, pulmonary hypertension (PH), genetic defects and complication after left ventricular assist device (LVAD) implantation [1]–[4]. While a great deal of research has been focused on elucidating progression of left ventricular (LV) failure via structural and functional analysis, knowledge concerning the failing and recovering right ventricle (RV) is comparatively scarce and currently insufficient for systematic development of effective treatment strategies [5]. Characterization of failure and recovery patterns in preclinical research is an important tool for bridging this knowledge gap and for the design and testing of treatments that could have significant impact due to the number of conditions on which RVF can develop.

Pressure overload is the most common RVF etiology with direct connection to elevated ventricular afterload typical of, among others, pulmonary arterial hypertension, reduced LV contractile function, and congenital heart disease. RVF due to pressure overload, which was the focus of this study, has been shown to reduce diastolic function primarily linked to wall stiffening mediated by hypertrophy and interstitial fibrosis [6]–[8]. These mediating factors can be conceptualized as mechanisms for limiting the magnitude of internal wall stresses via wall thickening (in hypertrophy) or material

stiffening due to increased perimysial collagen content (in fibrosis). Another factor associated with material stiffening consists of structural remodeling in terms of fiber orientation, although previous studies have yielded conflicting reports on its incidence and its extent [6], [9]. Myocardial structure is of special interest, because it is a significant contributor to organ function mediating RV contraction, which in turn causes interventricular septal compression and additional changes in LV kinematics [10]–[12].

Recently, the authors were involved in the development of a robust animal model of right ventricular failure due to chronic pressure overload. The model has the advantage of being reversible allowing the study of right ventricular recovery (RVR), in addition to RVF [13]. The long-term goal of this collaboration is to design an analysis workflow incorporating some aspects that are relevant to this dissertation including structural imaging, kinematic measurements, and mechanical simulations. The first aspect involves the application of structural analysis via diffusion tensor DT-MRI with its unique sensitivity to fiber directionality and to other aspects of myocardial microstructure, including interstitial fibrosis [14]–[16]. The primary objective of the present study is to provide some preliminary insight on the development of structural remodeling in RVF through analysis of DT-MRI parameters, and to identify the role of fiber structure remodeling as a compensatory adaptation to pressure overload.

6.3 Methods

6.3.1 Animal Model

Detailed information regarding methods and further evidence of failure and recovery can be found in a published description of the animal model [13]. Briefly,

using animal protocols subject to established guidelines and approved by supervisory offices at the University of Utah (protocol #13- 02010), New Zealand white rabbits (2.0-2.5 kg) were outfitted with a fully implantable, pulmonary artery (PA) band (Access Technologies, Skokie, IL, USA). After recovery from band implantation, injection of aqueous 0.9% into a subcutaneous port saline tightened the band according to estimates of RV end-systolic pressure (RVESP) obtained via transthoracic echo. Regular band tightening at weekly intervals was continued until RVESP measurements reached values over 25 mmHg, then it was maintained over a period of 2 weeks until evidence of RVF was observed (for instance, interventricular septum shift towards the left side, onset of hepatic congestion). Relaxing the PA band and allowing the animals to recover for a period of 2 additional weeks promoted RVR. The group of animals included controls (n=3), RVF (n=6), and RVR (n=2). CINE MRIs of one animal, which was used to generate a computer model, were obtained prior to PA banding and after RVF onset (retrospectively gated FLASH sequence, FOV 50x80mm, 10 short axis slices, 18° flip angle TR 43 ms, TE 2.9 ms) using a Bruker Biospec 7T imaging instrument and a 72mm quadrature volume coil.

6.3.3 Preparation of Specimens and DT-MRI Acquisition

Shortly after extraction, the hearts were cannulated at the aorta, and perfused with potassium chloride to evacuate blood from myocardial vasculature and cause cardiac arrest. A small amount of alginate (Smooth-On, PA, USA) comparable to systolic volume was injected inside the ventricles to prevent collapse. The samples were then fixed in formalin for over 48 h to avoid undesired fixation effects. Each heart was

scanned using a 50mm inner diameter quadrature volumetric coil (Rapid MRI, OH, USA) with a Bruker Biospec 7T imaging instrument. DT-MRI was obtained by applying a spin echo sequence (FOV 30x30x30 mm 128x85x85 pixels, TR 500ms, TE 23ms, 12 directions and 1000 mm/cm b-value) over a period of 13 h.

6.3.4 Image Analysis

Local coordinate systems for structural analysis were obtained using a distribution of potentials approach [17]. This method is particularly well suited for the analysis of RV geometry and deformed LV due to RVF, because, unlike the healthy LV, these cannot be accurately assumed to conform to a definite geometry. The process was automated using a MATLAB (Mathworks, MA, USA) script and calls to the Laplace equation solver within the finite-element solver part of the FEBio software suite [18]. The script consists of converting labeled images (LV and RV myocardium as well as their cavities) into pixel-wise hexahedral elements, and constructing three sets of boundary conditions corresponding to the apex-to-base, epicardium-to-endocardium, and right-to-left potential distributions, whose gradients determine local directionality.

Helical fiber distributions were obtained by projection of the principal eigenvector of the diffusion tensor obtained at every pixel after DT-MRI reconstruction on the plane tangent to myocardial surface, and calculation of angular distance with respect to the local circumferential direction. In RVF, based on empirical observation, the subjects were divided into “thin-walled” (n=3) and “thick-walled” (n=3) subgroups according to the mean RV wall thickness, respectively, corresponding to less than 50%, or over 50%, of mean LV wall thickness. Quantification of fiber distribution consisted of measuring

the transmural change of fiber orientation in the entire LV and the RV pixel population for control, combined RVF, separate RVF subgroups, and RVR specimens.

Parameters associated with DT-MRI sensitivity to interstitial diffuse fibrosis [16], including fractional anisotropy (FA), mean diffusivity (MD), and principal diffusivities (the principal eigenvalues of the diffusion tensor), were averaged in both the RV and LV. For visualization and measurement, wall thickness measurements were obtained from surfaces obtained by semi-automatic segmentation (Amira, FEI Life Sciences, OR, USA). Due to the small sample size, statistical analysis was not performed on the DT-MRI parameters or wall thickness measurements.

6.3.5 Numerical Simulations

To understand the effect of fiber structure remodeling in RV pressure overload, RV ejection fraction (RVEF) estimates were generated using a mechanical model of ventricular mechanics subject to normal and elevated RV afterloads using a nominal (quasilinear transmural helical angle change from -60° to 60°), and a longitudinally aligned (-75° to 75° , which is a 30% increase in transmural slope) helix angle distribution. The computational mesh is shown in Figure 6.1. Passive inflation diastolic pressure consisted of 13 mmHg in the LV, and 6 mmHg in the RV. Systolic pressures were 45mmHg and 15 mmHg for the LV and RV, respectively. In pressure overload, right ventricular pressure was increased by 25% according to measurements on the animal model [13]. Surfaces of approximately 75% of the ventricular volume at early diastole, which was assumed to be a no-load, stress-free configuration, were obtained via semi-automatic delineation (Amira, FEI Life Sciences, OR, USA) and meshed into

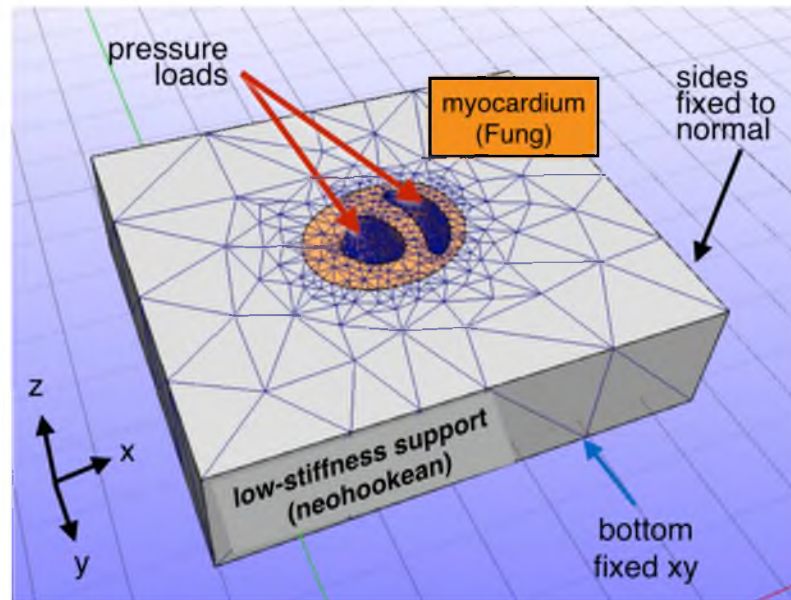


Figure 6.1: Computational mesh of biventricular mechanics. Ventricular volume was embedded in a support material. The strategy, akin to that described in Chapter 5, includes pressure loads for the ventricular cavities and fixed nodal displacements around the support material block.

33,000 quadratic tetrahedral elements (TetGen, Weierstrass Institute, Berlin, Germany). Mechanical behavior was modeled with a Fung-type constitutive model as in Chapter 5.

6.4 Results

Automated calculation of local coordinate systems using potential distribution was successful in all DT-MRI image sets by accurately producing boundary conditions based on label sets. Computational meshes varied between approximately 60 and 70 thousand elements. Although calculation of potentials for all three directions was performed in approximately 30 seconds, gradient calculation was performed in approximately 10 min on a 12-core 2GHz workstation.

Visualization of right ventricular thickness for representative specimens from the thick-walled and thin-walled groups appears in Figure 6.2. In the thin-walled group, hypertrophy was present mostly on the free RV wall. In contrast, the specimens belonging to the thick-walled exhibited myocardial hypertrophy across most of the RV, with the exception of the apex, which remained relatively unchanged in RVF and RVR.

Mean transmural helical angle slopes in RVR (Table 6.1) showed a trend of longitudinal alignment towards the base in the LV and towards the outflow direction in the RV with respect to the control group. In RVF, no trend was evident when both subgroups were averaged together. Separation into subgroups showed a clear trend characterized by increase in helical angle slope of approximately 30%, which is similar to that observed in RVR group with respect to controls. The thin-walled group exhibited changes in the opposite direction.

Figure 6.3 shows transmural helical angle distribution of representative specimens

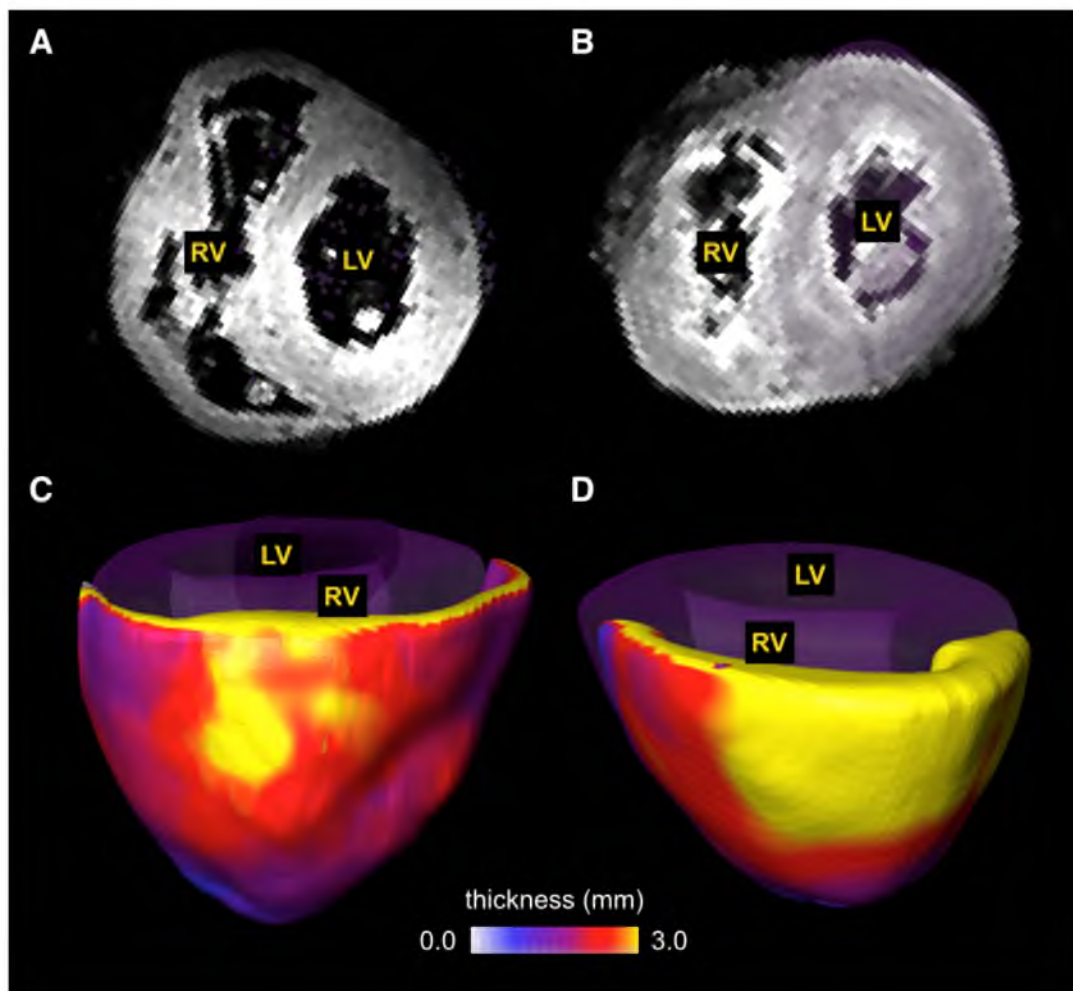


Figure 6.2: Wall thickness difference between failure specimens. Although all failure specimens were obtained from animals exhibiting signs of RVF, wall thickness variations existed among them as evident on anatomical MRI of thin-walled (A), and thick-walled (B) subgroups, as well as thickness visualization using the same classification (C and D, respectively).

Table 6.1: Mean helical angle slopes and specimen wall thickness

<i>group</i>	<i>helix</i>		<i>wall thickness</i>		<i>thickness ratio</i>
	<i>RV</i> (°)	<i>LV</i> (°)	<i>RV</i> <i>mm</i>	<i>LV</i> <i>mm</i>	<i>RV/LV</i> (-)
<i>control</i>	92(6)	135(8)	1.8(0.2)	1.7(0.4)	0.41
<i>failure (thin)</i>	82(10)	102(7)	2.1(0.5)	2.6(1.2)	0.38
<i>failure (thick)</i>	114(12)	134(16)	2.7(0.1)	3.4(0.4)	0.60
<i>failure (all)</i>	98(12)	118(13)	2.4(0.5)	3.5(1.3)	0.49
<i>recovery</i>	105(11)	140(6)	1.8(0.1)	3.0(0.1)	0.49

Numerical values are expressed as mean (SD)

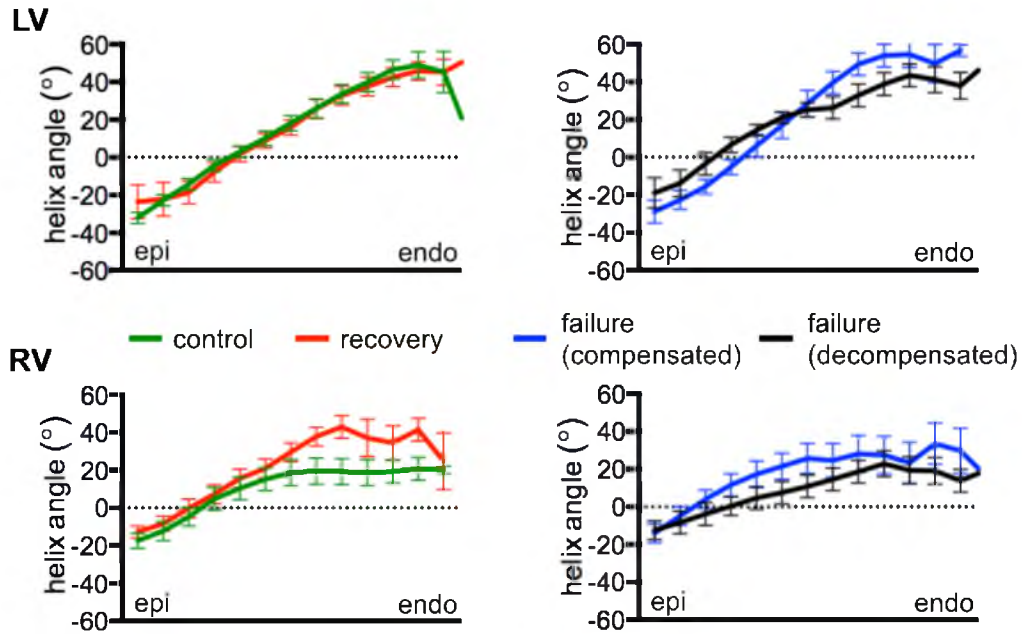


Figure 6.3: Representative transmural helical angle distributions of controls, RVR, and RVF subgroups. LV distribution was identical for control and recovery groups, which exhibited some localized similarities, for instance near the endocardium (left). RVF subgroups showed a clear trend that may suggest structural remodeling exhibited by increased distribution slope in both RV and LV (left).

from all four groups averaged over the entire ventricular wall. Control and RVR groups were characterized by identical distribution of LV helix angles, and localized similarities near the epicardium in the RV. Helix angle distribution followed the trends described previously, and this distribution was clearer on LV values than in the RV.

Mean DT-MRI parameters listed in Table 6.2 showed a reduction in RV functional anisotropy and mean diffusivity in the RVR and RVF “thick-walled” groups. No other trend was observed.

The numerical simulations of pressure overload with all other parameters held constant showed similar characteristics to those observed in the RVF MRIs. These features included an enlarged cavity and a bowed interventricular septum, and increase the confidence on the model’s ability to reproduce realistic behavior (Figure 6.4). The four ejection fraction approximations result in reduction under increased afterload. This drop is present in both, the model with nominal transmural helix angle distribution (RVEF decreases to 0.13 from 0.22), as well as the model with increased helical angle slope (RVEF decreases to 0.15 from 0.23).

6.5 Discussion

In general, limited by the small sample size and nature of nonlongitudinal experimentation, it is premature to conclusively state whether the specimens analyzed so far exhibited detectable changes between the different analysis groups. Nevertheless, encouraging trends were observed in terms of helical angle slope and wall thickness in RVF. If confirmed, these trends may offer an explanation for the inconsistent observations reported in the literature. Longitudinal alignment of fibers seen in the

Table 6.2: DT-MRI parameters

<i>group</i>	<i>FA</i>		<i>MD</i>	
	<i>RV</i> (-)	<i>LV</i> (-)	<i>RV</i> $10^{-3} \text{ mm}^2/\text{s}$	<i>LV</i> $10^{-3} \text{ mm}^2/\text{s}$
<i>control</i>	0.25(0.04)	0.24(0.05)	0.58(0.06)	0.62(0.03)
<i>failure (thin)</i>	0.26(0.02)	0.26(0.07)	0.63(0.10)	0.67(0.01)
<i>failure (thick)</i>	0.26(0.02)	0.28(0.01)	0.52(0.01)	0.57(0.02)
<i>failure (all)</i>	0.26(0.02)	0.27(0.04)	0.56(0.06)	0.61(0.02)
<i>recovery</i>	0.22(0.01)	0.29(0.00)	0.51(0.00)	0.57(0.02)

Numerical values are expressed as mean (SD)

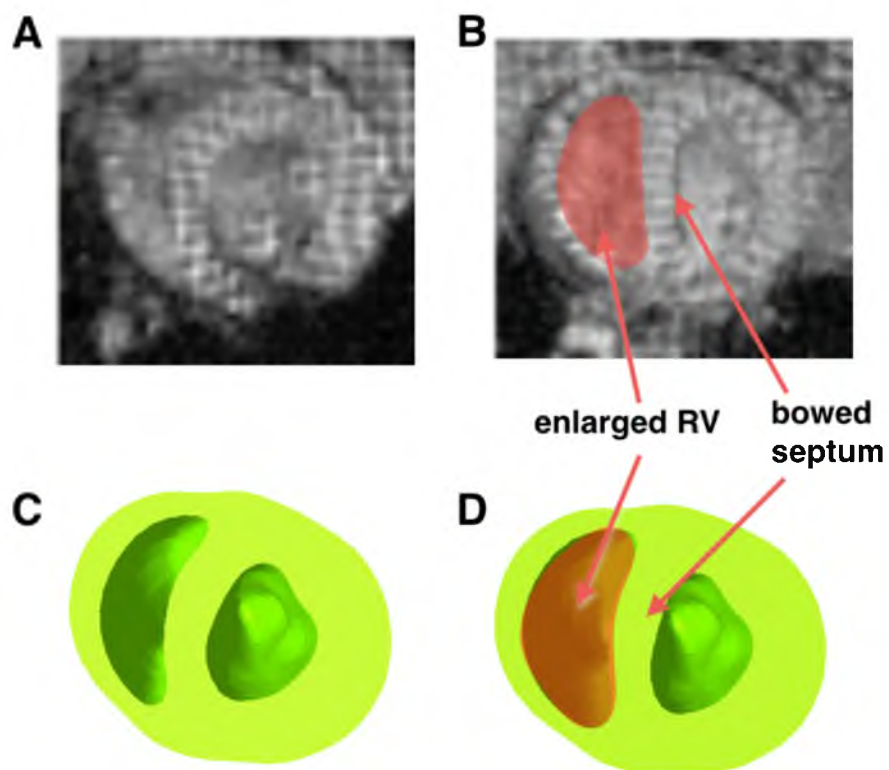


Figure 6.4: Biventricular simulation of pressure overload. Using CINE-MRI data (A), it was possible to construct a finite-element model of normal behavior (C), and the same model under pressure overload with every other parameter held constant (D). By mere simulation of increased afterload, the model exhibited features similar to RVF (B), including increase RV volume and intraventricular septum bowing.

thick-walled group were in accordance with a previous study based on histological sections where hypertrophy was directly confirmed [9]. In contrast, a DT-MRI investigation, similar to the present study, suggested no appreciable differences, but no histology results were offered [20]. It is possible that the previous DT-MRI study simply averaged out any evidence of structural changes by combining different levels of wall thickening that may occur due to biological variability in response to RV pressure overload. Further, the similarity between that RVR and thick-walled RVF, seen in terms of helical angle distribution as well as a reduction in RV FA and MD, may suggest a link between adaptation to overload and recovery. The functional implications of the observed structural changes can be seen in the numerical results. Increasing transmural helical slope, by an amount similar to that observed in the DT-MRI analysis, results in a 5% improvement in RVEF under normal conditions, but in a surprising 15% improvement under pressure overload, which suggests that longitudinal alignment may be particularly beneficial to recover ejection fraction in the presence of pressure overload. Further, if longitudinal alignment is achieved in a relatively short period, it may constitute a mechanism of ventricular reserve.

It is also possible that the observed trend is not associated with an underlying biological mechanism, but may be associated to fixation or specimen preparation error. This limitation can be mitigated by application of *in vivo* imaging. Despite of the lack of data for a rigorous statistical analysis, this preliminary study demonstrated an approach for automatic generation of local coordinate systems, and generation of biventricular simulations using quadratic tetrahedral elements. These contributions will mainstream and increase consistency in future investigations.

Aside from increasing the number of specimens in each group, this study can be further developed in terms of expanding the analysis strategy to other structural measures including transverse and sheet angles. Regional analysis may also be useful through application of statistical shape analysis, which can be used to characterize wall thickness across all groups. This approach may be useful to incorporate shape and material information, if a structural link is established, into mechanical models of the ventricles. Finally, the modeling approach can be improved by implementing a parameter identification routine similar to that shown in Chapters 3 and 5, which would likely improve the calculations of RVEF to better correspond to measurements *in vivo*.

6.6 Acknowledgements

The authors would like to thank Dr. Megan E. Bowen, and Dr. Xiaoqing Liu for operative assistance on the animal models and preparation of specimens

6.7 References

- [1] M. A. Fogel and J. Rychik, "Right ventricular function in congenital heart disease: pressure and volume overload lesions," *Prog. Cardiovasc. Dis.*, vol. 40, no. 4, pp. 343–56, 1998.
- [2] R. John, S. Lee, P. Eckman, and K. Liao, "Right ventricular failure--a continuing problem in patients with left ventricular assist device support," *J. Cardiovasc. Transl. Res.*, vol. 3, no. 6, pp. 604–11, Dec. 2010.
- [3] R. P. Vivo, A. M. Cordero-Reyes, U. Qamar, S. Garikipati, A. R. Trevino, M. Aldeiri, M. Loebe, B. A. Bruckner, G. Torre-Amione, A. Bhimaraj, B. H. Trachtenberg, and J. D. Estep, "Increased right-to-left ventricle diameter ratio is a strong predictor of right ventricular failure after left ventricular assist device," *J. Hear. Lung Transplantation*, vol. 32, no. 8, pp. 792–9, Aug. 2013.
- [4] M. Puhlman, "Continuous-flow left ventricular assist device and the right ventricle," *AACN Adv. Crit. Care*, vol. 23, no. 1, pp. 86–90, 2012.
- [5] N. F. Voelkel, R. A. Quaife, L. A. Leinwand, R. J. Barst, M. D. McGoon, D. R. Meldrum, J. Dupuis, C. S. Long, L. J. Rubin, F. W. Smart, Y. J. Suzuki, M. Gladwin, E. M. Denholm, and D. B. Gail, "Right ventricular function and failure: report of a National Heart, Lung, and Blood Institute working group on cellular and molecular mechanisms of right heart failure," *Circulation*, vol. 114, no. 17, pp. 1883–91, Oct. 2006.
- [6] S. L. Gaynor, H. S. Maniar, J. B. Bloch, P. Steendijk, and M. R. Moon, "Right atrial and ventricular adaptation to chronic right ventricular pressure overload," *Circulation*, vol. 112, no. 9, pp. I212–8, Aug. 2005.
- [7] M. A. J. Borgdorff, B. Bartelds, M. G. Dickinson, P. Steendijk, M. de Vroomen, and R. M. F. Berger, "Distinct loading conditions reveal various patterns of right ventricular adaptation," *Am. J. Physiol. Heart Circ. Physiol.*, vol. 305, no. 3, pp. H354–64, Aug. 2013.
- [8] M. S. Visner, C. E. Arentzen, A. J. Crumbley, E. V Larson, M. J. O'Connor, and R. W. Anderson, "The effects of pressure-induced right ventricular hypertrophy on left ventricular diastolic properties and dynamic geometry in the conscious dog," *Circulation*, vol. 74, no. 2, pp. 410–9, Aug. 1986.
- [9] M. R. Hill, M. A. Simon, D. Valdez-Jasso, W. Zhang, H. C. Champion, and M. S. Sacks, "Structural and mechanical adaptations of right ventricle free wall myocardium to pressure overload," *Ann. Biomed. Eng.*, vol. 42, no. 12, pp. 2451–2465, 2014.
- [10] S. J. Dong, E. R. Smith, and J. V Tyberg, "Changes in the radius of curvature of

- the ventricular septum at end diastole during pulmonary arterial and aortic constrictions in the dog,” *Circulation*, vol. 86, no. 4, pp. 1280–1290, Oct. 1992.
- [11] G. S. Nelson, E. Y. Sayed-Ahmed, C. A. Kroeker, Y. H. Sun, H. E. Keurs, N. G. Shrive, and J. V. Tyberg, “Compression of interventricular septum during right ventricular pressure loading,” *Am. J. Physiol. Heart Circ. Physiol.*, vol. 280, no. 6, pp. H2639–48, Jun. 2001.
- [12] J. Chua, W. Zhou, J. K. Ho, N. A. Patel, G. B. Mackensen, and A. Mahajan, “Acute right ventricular pressure overload compromises left ventricular function by altering septal strain and rotation,” *J. Appl. Physiol.*, vol. 115, no. 2, pp. 186–93, Jul. 2013.
- [13] S. H. McKellar, H. Javan, M. E. Bowen, X. Liu, C. L. Schaaf, C. M. Briggs, H. Zou, A. D. Gomez, O. M. Abdullah, E. W. Hsu, and C. H. Selzman, “Animal model of reversible, right ventricular failure,” *J. Surg. Res.*, vol. 194, no. 2, pp. 327–333, 2015.
- [14] D. F. Scollan, A. Holmes, R. Winslow, and J. Forder, “Histological validation of myocardial microstructure obtained from diffusion tensor magnetic resonance imaging,” *Am. J. Physiol.*, vol. 275, no. 6 Pt 2, pp. H2308–18, Dec. 1998.
- [15] E. W. Hsu, A. L. Muzikant, S. A. Matulevicius, R. C. Penland, and C. S. Henriquez, “Magnetic resonance myocardial fiber-orientation mapping with direct histological correlation,” *Am. J. Physiol.*, vol. 5 pt 2, no. 274, pp. H1627–H1627, 1998.
- [16] O. M. Abdullah, S. G. Drakos, N. A. Diakos, O. Wever-Pinzon, A. G. Kfoury, J. Stehlik, C. H. Selzman, B. B. Reid, K. Brunisholz, D. R. Verma, C. Myrick, F. B. Sachse, D. Y. Li, and E. W. Hsu, “Characterization of diffuse fibrosis in the failing human heart via diffusion tensor imaging and quantitative histological validation,” *NMR Biomed.*, vol. 27, no. 11, pp. 1378–86, Nov. 2014.
- [17] J. D. Bayer, R. C. Blake, G. Plank, and N. A. Trayanova, “A novel rule-based algorithm for assigning myocardial fiber orientation to computational heart models,” *Ann. Biomed. Eng.*, vol. 40, no. 10, pp. 2243–54, Oct. 2012.
- [18] S. A. Maas, B. J. Ellis, G. A. Ateshian, and J. A. Weiss, “FEBio: finite elements for biomechanics,” *J. Biomech. Eng.*, vol. 134, no. 1, pp. 011005–1,–10, Jan. 2012.
- [19] W. Kruskal and W. Wallis, “Use of ranks in one-criterion variance analysis,” *J. Am. Stat.*, vol. 47, no. 260, 1952.
- [20] E. Nielsen, M. Smerup, P. Agger, J. Frandsen, S. Ringgard, M. Pedersen, P. Vestergaard, J. R. Nyengaard, J. B. Andersen, P. P. Lunkenheimer, R. H.

Anderson, and V. Hjortdal, "Normal right ventricular three-dimensional architecture, as assessed with diffusion tensor magnetic resonance imaging, is preserved during experimentally induced right ventricular hypertrophy," *Anat. Rec.*, vol. 292, no. 5, pp. 640–51, May 2009.

CHAPTER 7

CONCLUDING REMARKS

7.1 Summary

This research was motivated by both, an interest for extending the capabilities of imaging hardware with the strategic application of computational physics, and current society's need for elucidating key aspects of the cardiovascular system in order to help detecting and treating disease. The objectives targeted four fundamental dimensions of imaging-based cardiovascular mechanics: morphology, material properties, tissue kinematics, and microstructure. The main contributions and considerations from each study are briefly highlighted in the following paragraphs.

The CT-based investigation of venous tissue in Chapter 3 showed that even relatively straight sections of vein have a markedly heterogeneous wall thickness, which affects the way strains are distributed along the tissue. On its own, morphological characterization of intact specimens can be useful for construction of computational geometry for computational fluid mechanics, or to obtain some interpretation of tissue constituents by evaluating the relative absorption of iodine [1]. The study also provided a strategy for incorporating an experimentally validated strain energy function into finite-element simulations. If, in addition to imaging, loading information is also known, the strategy was also demonstrated for material parameter identification enabling both geometrical

and material customization of numerical models of the vein. Customized models may be used to evaluate wall stress distribution though to be a contributing factor in neointimal hyperplasia [2], [3]. Though it is true that the presence of the amounts of iodine needed to achieve contrast may stiffen the tissue, the nature and precise implications of this effect are still unknown, and it is possible that it can be systematically reduced if before-and-after material testing reveals a consistent change. Further, material identification through the methods demonstrated in the study are expected to be fully applicable using other medical imaging modalities, because Hyperelastic Warping analysis has been successfully employed in the past to measure deformation with a range of scenarios including several imaging modalities [4]–[6]. For the vein, this versatility may allow the use of ultrasound or MRI.

Chapter 4 presented a method for obtaining myocardial displacements, which has already been demonstrated by several methods. However, one notable characteristic of the presented methodology is the emphasis on absolute and relatively fast displacements, which was either high temporal resolution (at the expense of additional scan time) or is highly prone to phase wrapping. This emphasis is well suited for small animal imaging, and for other applications involving kinematic characterization of large displacements and small deformations like skeletal muscle and brain biomechanics [7]. Because the method was shown to be robust over several deformations, tuning parameters, and signal-to-noise ratios, it can be reused virtually without modification once implemented. Importantly, the methodology introduced side-by-side analysis of deformation fields, which is not limited to vector displacement offset, but can be outfitted with additional error correction criteria allowing compatibility with other

imaging and mechanical information. For example, reconstruction of velocity fields with incomplete encoding gradient information could be corrected using computational fluid mechanics by employing a scaling correction model.

The models of tissue seen in Chapter 2 and Chapter 5 inherently possess both descriptive and predictive qualities, because the finite element method is embedded within the analysis methods. The descriptive characteristics have been employed for measurement of kinematics and structural description through FE-based registration and local coordinate system calculation. The predictive qualities have been exploited to approximate material properties and to estimate tissue deformation. In Chapter 5, subject specific material models were used to extrapolate DT-MRI information. By comparing a mechanically realistic simulation approach, i.e., including fiber orientation and tissue-based material behavior, with a simpler model, it was shown that regularization is a key component for mimicking experimentally observed structural alterations. That is, basic elastic or viscous registration will very likely produce erroneous results even if similar cavity volume (and arguably high similarity measure due to the lack of internal contrast inside the myocardium, as discussed in Chapter 3) is obtained.

7.2 Future Directions

Perhaps the main limitation of the presented methods comes from the need for a relatively detailed knowledge about the mechanical system under study, the imaging modality, and the modeling approach (or approaches) on part of the analyst. This is particularly true for the apparent circular logic regarding processing imaging data using

methods capable of obtaining identical parameters by simulation alone. For instance, displacements can be obtained from images through mechanics-based registration, but also through mechanical simulation of the system. Then, how is the image-based displacement solution separate from the simulation? Does agreement between both indicate faithfulness to the physical system, or is merely a foreseeable artifact? A similar challenge has been part of the implementation of fundamentally similar dynamic state observers, which combine sensor measurements with a system model. Nevertheless, just as dynamic observers are trusted to increase the effectiveness even in high-reliability applications like automated aircraft landing and cruise control, the applicability of even a rather simplistic model to perform a specific task should not be an overwhelming idea. For instance, in Chapter 2, some care was taken to ensure that the imaging-based strain measurement was reasonably independent of material assumptions. Further sufficient evidence of constitutive behavior was already in place to limit the investigation to parameter identification, as opposed to rigorous material characterization, which must follow more systematic and specialized protocols [8], [9]. In Chapter 3, the use of displacement-encoded MRI virtually eliminated the need for material information to measure deformation. However, the finite-element registration algorithm automatically calculates stress values, which, in the study, were completely meaningless.

Form a technical perspective, the use of numerical verification and experimental validation demonstrated the effectiveness of the presented methods, which are a large focus of this work. However, to some extent, the specimen count across the study was not sufficient to draw precise biological conclusions. This is both particularly true, and

particularly impractical, in Chapter 5, because future studies regarding structural variability and computational modeling may benefit from descriptions of accuracy in terms of absolute error in structural alterations and quantitative characterization of cardiac structure. Despite the potential benefits granted by these data, there are significant challenges associated with quantitative analysis DT-MRI for the purpose of obtaining such information, including the presence of crossing fibers in cardiac tissue [10], the lack of a clear model for ventricular structure [11], and numerical errors associated with sorting eigenvectors and noise.

A main theme of this research, imaging-based biomechanics for improved medical imaging reconstruction, can be further developed for biological motion estimation by generating a systematic approach for balancing simulated results and imaging information based on instrumentation and process noise covariance. As a start, this approach would be best implemented with an explicit solver, because a displacement solution at a given point depends on the solution at the previous time point (or points). Much like in a state observer [12], if displacements from a series of imaging data are also available, e.g., a finite set of MRI, then a weighted average of simulated and observed results can be used for the next time point. In fact, the approach would be a generalized state observer with two main benefits: filtering (and interpolation) of imaging data even at very low signal-to-noise ratios, and relatively simple incorporation of different data sources including like elastography for material property measurement for stress analysis. Alternatives to the finite element method, such as the material point method, could be explored to overcome limitations associated with mesh generation and tangling in certain applications.

In terms of structural atlas generation, a different direction of future research consists of further evaluation of low basis functions, such as low order polynomials, to describe left ventricular structure and the expansion of these methods to the right ventricle. Once parameterization of 3D ventricular structure can be narrowed to a definite set of equations, their coefficients could be made a function of time. In that case, experimental validation could consist of discrete points of DT-MRI data. As these data are made available, a more comprehensive interpretation of diffusion and its interaction, not only with strain, but also myocardial perfusion may be necessary to better understand the significance of DT-MRI information in terms of diffusive and advective transport mechanisms occurring in *in vivo* cardiac tissue [13], [14]. Interpretation of these mechanisms, combined with the predicted deformation, can be used to clarify the precise type of warping approach needed for extrapolation of data at a given precision. For example, in Chapter 5, rotation-only and full application of the deformation matrix on a given vector was applied. Yet, it is possible that deforming the diffusion tensor itself and recalculating its principal directions may provide the best approximations of structural alteration in living tissue.

7.3 Final Thoughts

Medical imaging technologies have evolved and branched into specialized applications featuring outstanding examples for noninvasive investigation of the mechanics of biological tissue through morphological, constitutive, kinematic, and microstructural analysis, as well as and untapped potential limited by technical challenges. This dissertation has presented a series of methods and applications, which

enhance specific capabilities of imaging hardware through integrated analysis of computational biomechanics, particularly with the finite-element method. In doing so, this manuscript demonstrated several instances of physics-based image analysis and reconstruction as an integrative field of study where enforcement of basic conservation principles is the key for enhancing the strengths of both, imaging systems and numerical simulations.

7.4 References

- [1] K. Degenhardt, A. C. Wright, D. Horng, A. Padmanabhan, and J. A. Epstein, “Rapid 3D phenotyping of cardiovascular development in mouse embryos by micro-CT with iodine staining,” *Circ. Cardiovasc. Imaging*, vol. 3, no. 3, pp. 314–22, May 2010.
- [2] C. A. Lemarié, P.-L. Tharaux, and S. Lehoux, “Extracellular matrix alterations in hypertensive vascular remodeling,” *J. Mol. Cell. Cardiol.*, vol. 48, no. 3, pp. 433–9, Mar. 2010.
- [3] S. Lehoux and A. Tedgui, “Cellular mechanics and gene expression in blood vessels,” *J. Biomech.*, vol. 36, no. 5, pp. 631–643, May 2003.
- [4] A. I. Veress, J. A. Weiss, G. T. Gullberg, D. G. Vince, and R. D. Rabbitt, “Strain measurement in coronary arteries using intravascular ultrasound and deformable images,” *J. Biomech. Eng.*, vol. 124, pp. 734–41, Dec. 2002.
- [5] N. S. Phatak, S. A. Maas, A. I. Veress, N. A. Pack, E. V. R. Di Bella, and J. A. Weiss, “Strain measurement in the left ventricle during systole with deformable image registration,” *Med. Image Anal.*, vol. 13, no. 2, pp. 354–61, Apr. 2009.
- [6] N. Phatak, Q. Sun, S.-E. Kim, D. Parker, K. Sanders, A. Veress, B. Ellis, and J. A. Weiss, “Noninvasive determination of ligament strain with deformable image registration,” *Ann. Biomed. Eng.*, vol. 35, no. 7, pp. 1175–87, Jul. 2007.
- [7] P. V Bayly, E. H. Clayton, and G. M. Genin, “Quantitative imaging methods for the development and validation of brain biomechanics models,” *Annu. Rev. Biomed. Eng.*, vol. 14, pp. 369–96, Jan. 2012.
- [8] D. P. Sokolis, “Experimental investigation and constitutive modeling of the 3D histomechanical properties of vein tissue,” *Biomech. Model. Mechanobiol.*, vol. 12, no. 3, pp. 431–51, Jun. 2013.
- [9] C. Wang, M. Garcia, and X. Lu, “Three-dimensional mechanical properties of porcine coronary arteries: a validated two-layer model,” *Am. J. Physiol. Circ. Physiol.*, vol. 291, no. 3, pp. 1200–1209, 2006.
- [10] D. E. Sosnovik, R. Wang, G. Dai, T. G. Reese, and V. J. Wedeen, “Diffusion MR tractography of the heart,” *J. Cardiovasc. Magn. Reson.*, vol. 11, p. 47, Jan. 2009.
- [11] R. H. Anderson, D. Sanchez-Quintana, K. Redmann, and P. P. Lunkenheimer, “How are the myocytes aggregated so as to make up the ventricular mass?” *Semin. Thorac. Cardiovasc. Surg.*, pp. 76–86, Jan. 2007.

- [12] R. E. Kalman, "A new approach to linear filtering and prediction problems," *J. Basic Eng.*, vol. 82, no. 1, p. 35, Mar. 1960.
- [13] E. O. Stejskal and J. E. Tanner, "Spin diffusion measurements: spin echoes in the presence of a time-dependent field gradient," *J. Chem. Phys.*, vol. 42, no. 1, p. 288, Jul. 1965.
- [14] E. M. Haacke, R. W. Brown, M. R. Thompson, and R. Venkatesan, *Magnetic Resonance Imaging: Physical Principles and Sequence Design*. Wiley-Liss Publishers, 1st Ed. 1999.